UNIVERSITY OF PADOVA

DEPARTMENT OF INFORMATION ENGINEERING
Ph.D. Course in Information Engineering
Information and Communication Science and Technologies Curriculum
XXXV series

Empirical Analysis and Network-wide Optimization for Next Generation Wireless Communications

Ph.D. Candidate
Salman Mohebi Ganjabadi

Ph.D. Supervisor
Michele Zorzi

Ph.D. Co-supervisor
Andrea Zanella

Ph.D. Coordinator
Andrea Neviani

Academic Year
2021–2022

To brave people of Iran,
and to Woman
Life
Freedom.

Abstract

The 5th Generation (5G) wireless networks have already been deployed worldwide, providing a multi-fold Quality of Service (QoS) improvement, compared to 4G, by adopting new techniques, such as Millimeter Wave (mmWave) frequency bands, advanced spectrum management techniques, and the integration of licensed and unlicensed bands. The next-generation networks will be empowered by new technologies such as Reconfigurable Intelligent Surface (RIS), Unmanned Aerial Vehicle (UAV) communications, and Cell-free (CF) massive Multiple-Input, Multiple-Output (mMIMO) technologies to further improve over existing technologies. In this thesis, we investigate the paradigm of the future generation of wireless systems, their requirements and specifications, emerging applications, and their enabling technologies. We analyze the usage of mmWave frequencies in indoor and outdoor environments. We discuss the challenges related to the scheduling of IEEE 802.11ad/ay, which provides multi-gigabit service over mmWave links, in realistic scenarios. We also analyze the performance of outdoor mmWave transmissions by conducting a measurement campaign in an early deployed 5G mmWave cell. We study various environmental impacts such as the body and foliage blockage, rain, and over-water transmission on mmWave links. Comparing our results with the simulations, we observe a performance gap between current operational networks and the reference system modeled in simulations. The proposed technologies for future wireless systems, i.e., RIS and UAVs, still need to be optimized before being functional. Hence, we propose some network-wide optimization schemes to increase the performance of such systems. We propose an energy-efficient design for joint RIS and UAV transmissions to provide sustainable communications in dense urban environments. We define a joint UAV trajectory and RIS phase optimization problem that minimizes the transmission power of UAV and Base Station (BS) while guaranteeing a certain level of data rate for users. Finally, we discuss CF mMIMO networks and propose pilot reuse strategies to optimize the system's rate. We formulate the pilot assignment problem in CF mMIMO as a diverse clustering problem and propose an iterative optima search scheme to solve it.

Sommario

Le reti wireless di quinta generazione (5G) sono già state distribuite in tutto il mondo e forniscono un miglioramento della qualità del servizio (QoS) di molte volte rispetto al 4G, grazie all'adozione di nuove tecniche, come le bande di frequenza a onde millimetriche (mmWave), tecniche avanzate di gestione dello spettro e l'integrazione di bande con e senza licenza. Le reti di prossima generazione saranno potenziate da nuove tecnologie come i RIS (Reconfigurable Intelligent Surface), le comunicazioni UAV (Unmanned Aerial Vehicle) e le tecnologie CF mMIMO (Cell-free massive Multiple-Input, Multiple-Output), per migliorare ulteriormente le tecnologie esistenti. In questa tesi, analizziamo il paradigma della futura generazione di sistemi wireless, i loro requisiti e specifiche, le applicazioni emergenti e le tecnologie abilitanti. Analizziamo l'utilizzo delle frequenze mmWave in ambienti interni ed esterni. Discutiamo le sfide legate alla programmazione di IEEE 802.11ad / ay, che fornisce servizi multi-gigabit su collegamenti mmWave, in scenari realistici. Analizziamo inoltre le prestazioni delle trasmissioni mmWave all'aperto conducendo una campagna di misura in una cella mmWave 5G di prima implementazione. Studiamo vari impatti ambientali, come l'ostruzione dovuta a corpi e fogliame, la pioggia e la trasmissione via acqua sui collegamenti mmWave. Confrontando i nostri risultati con le simulazioni, osserviamo un divario di prestazioni tra le reti operative attuali e il sistema di riferimento modellato nelle simulazioni. Le tecnologie proposte per i futuri sistemi wireless, cioè RIS e UAV, devono ancora essere ottimizzate prima di essere funzionali. Pertanto, proponiamo alcuni schemi di ottimizzazione a livello di rete per aumentare le prestazioni di tali sistemi. Proponiamo un design efficiente dal punto di vista energetico per le trasmissioni congiunte di RIS e UAV per fornire comunicazioni sostenibili in ambienti urbani densi. Definiamo un problema di ottimizzazione della traiettoria dell'UAV e della fase del RIS che minimizza la potenza di trasmissione dell'UAV e della stazione base (BS), garantendo al contempo un certo livello di velocità di trasmissione dei dati per gli utenti. Infine, discutiamo le reti CF mMIMO e proponiamo strategie di riutilizzo dei segnali pilota per ottimizzare la velocità del sistema. Formuliamo il problema dell'assegnazione dei segnali pilota in CF mMIMO come un problema di clustering diversificato e proponiamo uno schema di ricerca iterativa dell'ottimo per risolverlo.

Contents

Listing of figures

Listing of tables

Listing of acronyms

Symbols

1G 1 st Generation

2D 2-dimensional

3D 3-dimensional

3GPP 3rd Generation Partnership Project

4G 4th Generation

5G 5th Generation

6G 6th Generation

A

A-BFT Association-BeamForming Training

AC Access Category

ADDTS Add Traffic Stream

AI Artificial Intelligence

AoA Angle of Arrival

AoD Angle of Departure

AP Access Point

AR Augmented Reality

ATI Announcement Transmission Interval

B

B5G beyond-5G

BCI Brain Computer Interface

BHI Beacon Header Interval

BI Beacon Interval

BS Base Station

BTI Beacon Transmission Interval

C

C-RAN Cloud Radio Access Network

CBAP Contention-Based Access Period

CDF Cumulative Distribution Function

CF Cell-free

cobot collaborative robot

CoMP Coordinated MultiPoint

CPU Central Processing Unit

CSI Channel State Information

CSMA/CA Carrier Sense Multiple Access with Collision Avoidance

D

D2D Device-to-Device

DCP Diverse Clustering Problem

DKED Double Knife Edge Diffraction

DL Downlink

DLT Distributed Ledger Technology

DMG Directional Multi-Gigabit

DNN Deep Neural Network

DTI Data Transmission Interval

DTMKE Double-truncated Multiple Knife-edge

E

EDCA Enhanced Distributed Channel Access

eMBB Enhanced Mobile BroadBand

emMTC Extremely Massive Machine-Type Communication

eRLLC Extremely Reliable Low Latency Communication

ESE Extended Schedule Element

F

FL Federated Learning

FWA Fixed Wireless Access

H

HT Holographic Telepresence

I

IoE Internet of Everything

IoT Internet of Things

IoV Internet of Vehicles

IRS Intelligent Reflecting Surface

ISM Industrial, Scientific, and Medical

ITS Intelligent Transport System

ITU International Telecommunication Union

K

KPI Key Performance Indicator

L

LDHMC Long Distance and High Mobility Communication

LEO Low Earth orbit

LIS Large Intelligent Surface

LoS Line-of-Sight

LSF Large-Scale Fading

LTE Long Term Evolution

M

M2M Machine to Machine

MAC Medium Access Control

MCS Modulation and Coding Scheme

ML Machine Learning

mMIMO massive Multiple-Input, Multiple-Output

MMSE Minimum Mean Square Error

mMTC massive Machine-Type Communication

mmWave Millimeter Wave

MR Mixed Reality

MRT Maximum Ratio Transmission

MTC Machine-Type Communication

MU-MIMO Multi-User Multiple Input, Multiple Output

N

NB-IoT Narrow Band Internet of Things (IoT)

NextG Next Generation

NLoS Non-Line-of-Sight

NR New Radio

ns-3 Network Simulator 3

NSA Non-Standalone

NTN Non-Terrestrial Network

P

PBSS Personal Basic Service Set

PCI Physical Cell Identity

PCP Personal Basic Service Set (PBSS) Central Point

PCP/AP PBSS Central Point / Access Point

PHY Physical Layer

PoC Proof of Concept

Q

QoE Quality of Experience

QoS Quality of Service

R

RAN Radio Access Network

RE Resource Element

RF Radio Frequency

RIS Reconfigurable Intelligent Surface

RL Reinforcement Learning

RMa Rural Macro

RMS Root Mean Square

RSRP Reference Signal Received Power

RTT Round Trip Time

S

SCA Successive Convex Approximation

SDS Software Defined Surface

SE Spectral Efficiency

SNR Signal-to-Noise Ratio

SP Service Period

SS Synchronization Signal

SS-RSRP Synchronization Signal Reference Signal Received Power

SSB Synchronization Signal (SS)

SSS Secondary Synchronization Signal

SSW Sector Sweep

STA Station

T

TCP Transmission Control Protocol

TDD Time Division Duplexing

THz Terahertz

TSPEC Traffic Specification

U

U2X UAV-to-Everything

UAV Unmanned Aerial Vehicle

UDN Ultra Dense Network

UE User Equipment

UeMBB Ubiquitous Enhanced Mobile Broadband

UL Uplink

UMa Urban Macro

UMi Urban Micro

UPA Uniform Planar Square Array

URLLC Ultra-Reliable Low Latency Communication

V

V2X Vehicle-to-everything

VANET Vehicular Ad-hoc NETwork

VBR Variable Bit Rate

VLC Visible Light Communication

VR Virtual Reality

W

Wi-Fi Wireless Fidelity

WiGig Wireless Gigabit

X

XL-MIMO eXtra Large scale massive MIMO

XR eXtended Reality

1

Introduction and Motivation

In the last years, the mobile traffic demand has grown exponentially due to the increased number of connected devices and various data-hungry applications running on these devices. The global mobile traffic value is increasing from 7.462 EB/month in 2010 to 5016 EB/month in 2030 [1], which shows the necessity of improving wireless communication systems. Next Generations (NextGs) of wireless communication systems will bring a fully connected society of automated and intelligent systems. These systems will be used in industries, homes, vehicles, cities, and so on. Hence, providing ubiquitous connectivity with reliable and high data rate will be essential to support these applications. The 5th Generation (5G) wireless networks have already been deployed worldwide. The 5G provides a better Quality of Service (QoS) compared to the 4th Generation (4G) networks, employing new techniques, such as Millimeter Wave (mmWave) frequency bands, advanced spectrum management techniques, and the integration of licensed and unlicensed bands [2], [3]. Even though 5G offers significant improvements over previous systems, it is not expected that 5G can deliver a fully automated and intelligent network with everything as a service and a completely immersive experience [3], [4]. The convergence of communication, sensing, control, intelligence, and computing functionalities, which is necessary to future Internet of Everything (IoE) applications [2], is indeed expected to exceed 5G network's capabilities. On the other hand, some specific applications, like wireless Virtual Reality (VR), that requires a minimum of 10 Gbps data rate [5], are beyond 5G capabilities and will go for NextGs of wireless systems.

NextGs of wireless communication systems will fulfill the laggings of current systems by adding new features and technologies like ambient sensing, new human-to-human and human-to-machine interfaces, Terahertz (THz) communications, quantum communications, holographic beamforming, backscatter communication, Unmanned Aerial Vehicle (UAV) communication, Reconfigurable Intelligent Surface (RIS), Cell-free (CF) massive Multiple-Input, Multiple-Output (mMIMO) systems [6]. The 6th Generation (6G) systems need to continue the trends of previous generations

while introducing new services and inventing new technologies. The new services include Artificial Intelligence (AI), smart wearable devices, autonomous vehicles and cars, extended reality, wireless sensing, and 3-dimensional (3D) mapping [7].

6G systems will further expand the 5G paradigm, increasing the system performance and users QoS by several folds compared to 5G. It is envisioned that 6G will provide global communication facilities with per-user rate up to 1 Tbps in many use cases [8], with the latency less than 1 ms in ultra-long-range communications [9]. Machine Learning (ML) and AI will be fully integrated into 6G communication systems, making native-AI wireless networks to support various network management operations from physical layer signal processing to resource and service management. The NextG wireless communication will converge all the past features, including network densification, high throughput, ultra-reliability, low latency, low energy consumption, and massive connectivity [2]. Still, the most critical requirements for 6G will be the capability of handling massive volumes of data and very high per-device data rate [5]. New technologies are required to meet this requirement. In wireless communications, throughput is defined as Throughput [bit/s] = Bandwidth [Hz] $\times$ Spectral efficiency [bit/s/Hz].

To increase the throughput, one can explore new technologies that improve bandwidth, spectral efficiency, or both. This thesis focuses on technologies and solutions to improve the throughput, either by increasing the bandwidth, i.e., exploring the mmWave band frequencies, both for indoor (Wireless Gigabit (WiGig)) and outdoor (mmWave cellular networks), or optimizing the spectral efficiency in CF mMIMO, RIS-aided UAV communications.

1.1 Trends in Wireless Communications

From the 1 st Generation (1G) of wireless cellular systems, almost every ten years, a new generation of wireless systems has been introduced, supporting new features and services and providing higher QoS metrics compared to previous generations. NextG of wireless communication systems is also expected to improve 5G capabilities by a factor of 10-100, to be able to handle the increasing number of connected devices and the growing traffic demands after the next ten years.

Figure 1.1 shows the estimated number of connected devices from 2020 to 2027 [10]. As can be seen from the figure, the number of connected devices will exceed 40 B by 2027. While most of these devices will be Internet of Things (IoT) devices with their unique connectivity characteristics (e.g., transmitting small packets), other data-consuming devices, like mobile phones, laptops, and tablets, will still consume a large portion of network traffic.

Also, Figure 1.2 shows the exponentially increasing mobile traffic values from 2020 to 2030, predicted by International Telecommunication Union (ITU) [1]. As expected, in 2030, the global mobile traffic will exceed 5 ZB per month, showing an 80$\times$ increase compared to 2020, and per subscription, traffic demand will increase 50$\times$ to reach 257 GB/month.

It is expected that by 2030, the 5G will reach its capacity limits [2], so new architectures, technologies, and intelligent network management solutions need to be added on top of it to be able to support applications and traffic demands after that. This will force us to enter the 6G era, where

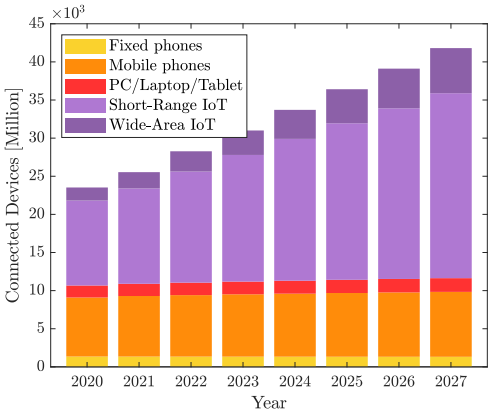

Figure 1.1: Estimated number of connected devices by 2027 [10].

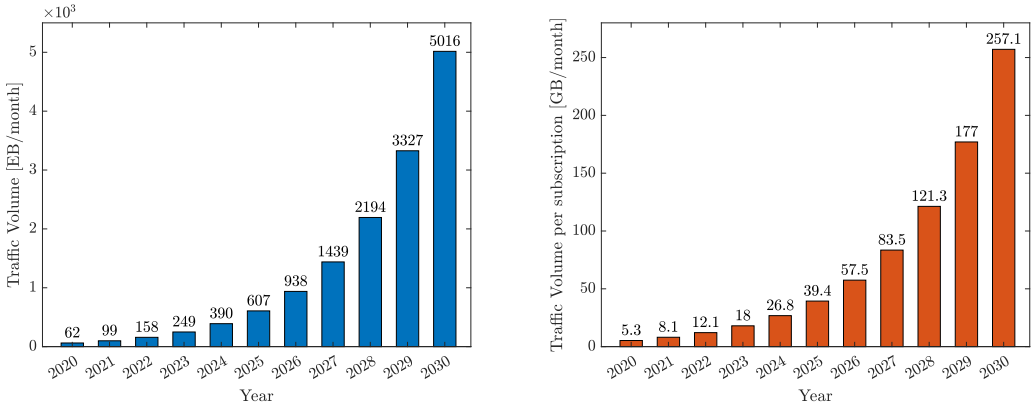

Figure 1.2: Traffic estimates for the years 2020 to 2030 [1].

new technologies, such as UAV swarms, cell-free mMIMO, RIS come together to provide a modern and intelligent communication ecosystem and seamless ubiquitous connection to users. This new paradigm will have some characteristics like high data rate, ultra-reliability, low latency, high energy efficiency, new spectra, intelligent networking, and convergence between sensing, computing, control, and communication, which will bring a fully digitally connected world.

1.2 Performance of Wireless Systems

While cellular networks were originally designed for voice communications, wireless data transmission is dominant nowadays, and on-demand video service originates most of wireless traffic [10]. One of the aims of the NextG of wireless systems is providing ubiquitous connectivity with enhanced data rate for end-users, which is critical for various applications such as wireless Augmented Reality (AR)/VR. The ubiquity can be achieved by increasing the wireless network

coverage and improving the throughput in the coverage area, and many technologies have already been proposed to achieve this goal, e.g., Ultra Dense Network (UDN) or mMIMO. The area throughput is a highly relevant performance factor for contemporary and future wireless networks [11]. It is measured in bit/s/km^2 and can be represented by the following high-level formula:

$$\text{Area throughput [bit/s/km}^2\text{]} = \mathrm{B}\,\text{[Hz]} \times \mathrm{D}\,\text{[cells/km}^2\text{]} \times \mathsf{SE}\,\text{[bit/s/Hz/cell]}$$

where B is the bandwidth, D is the average cell density, and SE is the spectral efficiency, defined as the amount of information that can be transferred over one Hz bandwidth in one second.

These three components, thus, need to be increased to improve the area throughput of communication systems. In summary, to improve the area throughput of wireless communication systems, one should:

- Allocate more bandwidth, which can be done by exploring higher frequency bands, e.g., mmWave.
- Densifying the network by deploying more and more cells in the area, i.e., UDNs, or designing new dense network architectures like CF mMIMO.
- Improving the spectral efficiency by designing the optimization schemes for utilizing the available resources.

In this thesis, we investigate different technologies and solutions to improve the throughput and QoS for end users, including exploring the mmWave frequency bands to provide very high data rate for both indoor (i.e., WiGig) and outdoor applications, RIS-assisted UAV communications, and CF mMIMO networks.

The abundant free spectrum available at mmWave frequencies, spanning from 30 GHz to 300 GHz, makes mmWave communication a key enabler for 5G and beyond-5G (B5G) systems to support bandwidth-hungry applications like online High Definition video streaming, AR/VR, and road-side vehicular communications. In this frequency range, the amount of available bandwidth is significantly more significant than that of the legacy sub-6 GHz counterpart, allowing unprecedented transfer speeds. Drones or UAVs are recognized as an essential part of B5G wireless communications. Thanks to their unique characteristics such as easy deployment, strong Line-of-Sight (LoS) links, degree of freedom, and controlled mobility [2], UAVs can act as flying or aerial Base Stations (BSs), providing better service compared to traditional fixed infrastructures. RIS consist of many reflecting diode units that can reflect any incident electromagnetic signals by an adjustable phase shift [12], [13]. In NextG era, RIS will play a critical role in controlling the propagation environment by deploying very large smart surfaces to improve the network coverage and throughput for the users that do not have LoS links to the BS.

The CF or distributed mMIMO systems are composed of a large number of distributed antennas that jointly serve relatively fewer users [14]. The operation, unlike the traditional cellular network, takes place in a user-centric fashion, where each user is surrounded and served by

multiple antennas. These antennas are connected to a Central Processing Unit (CPU) through high-capacity channels, where the network synchronization, data detection / precoding / decoding, and some other network management operations take place. CF mMIMO can considerably improve the performance compared to the conventional small-cell scheme, where each user is served by a dedicated BS. CF mMIMO has been considered one of the enabling technologies for B5G communications [15].

The remainder of this thesis is structured as follows: Chapter 2 provides an overview of the next generations of wireless communication systems and discusses the specifications and requirements of B5G and 6G networks, emerging applications in NextG networks, and enabling technologies in future wireless communications. Chapter 3 discusses the IEEE 802.11ad / ay standards that operate over 60 GHz of mmWave frequency bands and aim to provide multi-gigabit rates in indoor environments. It then presents some of the challenges related to the scheduling of IEEE 802.11ad / ay devices in realistic scenarios, with the main focus on the already-standardized IEEE 802.11ad. Furthermore, it discusses some pre-existing works and proposes some research directions. The Chapter 4, the usage of mmWaves in outdoor environments is investigated. It analyzes the performance of an early deployed mmWave cell and studies different environmental impacts on mmWave links, from the body and foliage blockage to rain and over-water transmission. Then it compares the actual system performance with simulations to reveal the gap between deployments and theoretical ones.

6G will be supported by new technologies and innovations such as RIS, UAVs, and CF mMIMO. These technologies can bring multi-fold QoS improvement over the existing technologies. These systems still need to be optimized with respect to various performance metrics such as data rate, network coverage, and energy consumption. In Chapter 5 the usage of RIS in conjunction with UAVs is being investigated as a way to provide energy-efficient communication to ground users in dense urban areas. It devises an optimization scenario to reduce overall energy consumption in the network while guaranteeing certain QoS to the ground users in the area. Due to the complex nature of the optimization problem, we provide a joint UAV trajectory and RIS phase decision to minimize transmission power of the UAV and BS that yields good performance with lower complexity. Chapter 6 discusses CF mMIMO networks and proposes pilot reuse strategies to optimize the system's rate. It formulates the pilot assignment in CF mMIMO as a diverse clustering problem and proposes an iterative optima search scheme to solve it. Finally, Chapter 7 concludes the thesis, providing some unsolved issues and some possible future research direction.

2

Next Generation Wireless Networks

The 6th Generation (6G) systems need to continue the trends of previous generations while introducing new services and technologies. The new services include Artificial Intelligence (AI), intelligent wearable devices, autonomous vehicles and cars, eXtended Reality (XR), and smart industry [7]. New technologies will be introduced, and the existing ones will be further improved to support these emerging services [6]. AI will be fully integrated into 6G communication systems, making native-AI wireless networks to support various network management operations from the physical layer to transport and application layers. The characteristics of previous wireless communication systems, including high throughput, ultra-reliability, low latency, and massive connectivity, will be converged in 6G [2]. Additional features will be incorporated with the previous ones to create a coherent communication system in 6G. Still, the most critical requirements for 6G will be the capability of handling massive volumes of data and very high per-device data rate [5].

In this chapter, we discuss the characteristics of the future generations of wireless communication systems, their specifications and requirements, the emerging applications that are foreseen in 6G, and potential enabling technologies of Next Generation (NextG) networks. Figure 2.1 illustrates these applications and enabling technologies.

2.1 6G Specifications and Requirements

5th Generation (5G) is associated with trade-offs among various requirements such as throughput, delay, energy efficiency, and reliability to support massive Machine-Type Communications (mMTCs), Enhanced Mobile BroadBand (eMBB), Ultra-Reliable Low Latency Communications (URLLCs) use cases. The main objectives of the NextG wireless communication are to improve these aspects and add new requirements on top of them. So, beyond-5G (B5G) networks should

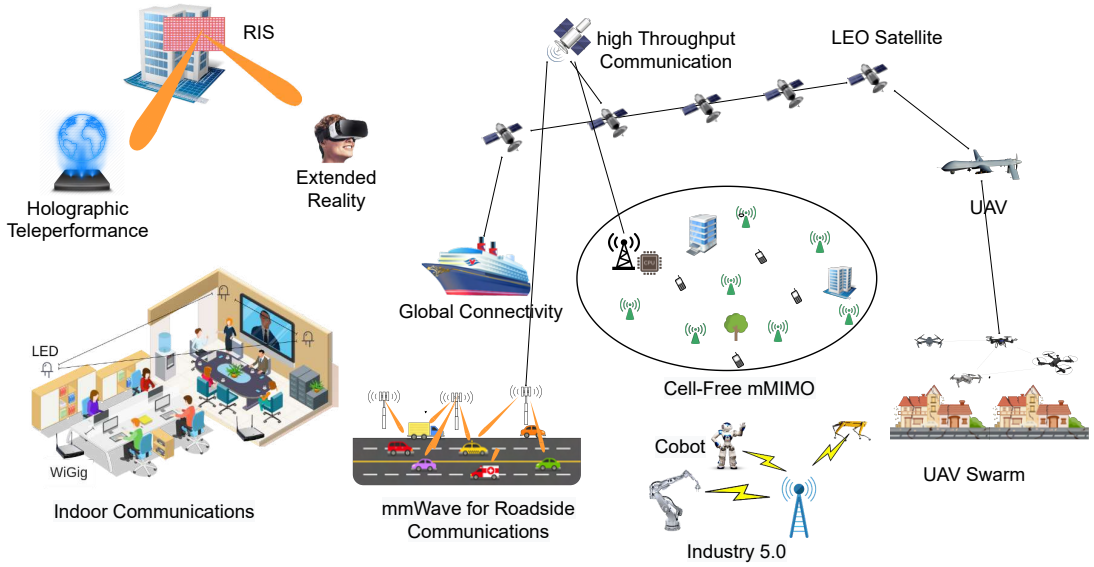

Figure 2.1: Applications, use-cases and the enabling technologies in next generation networks.

Table 2.1: Copmarison of 4G, 5G and 6G communication systems [2].

	4G	5G	6G
Per-device peach data rate	1 Gbps	10 Gbps	1 Tbps
End-to-end latency	100 ms	10 ms	1 ms
Maximum spectral efficiency	15 bps / Hz	30 bps / Hz	100 bps / Hz
Mobility support	350 km / h	500 km / h	1000 km / h
Satellite integration	No	No	Fully
AI	No	Partially	Fully
Autonomous vehicle	No	Partially	Fully
XR	No	Partially	Fully
Haptic Communication	No	Partially	Fully
THz Communication	No	Limited	Widely
Service level	Video	AR / VR	Tactile
Architecture	MIMO	massive MIMO	Intelligent surface
Maximum frequency	6 GHz	90 GHz	10 THz

provide (i) a very high per-device throughput, (ii) a massive number of connected devices, (iii) global connectivity, (iv) very low latency, (v) high reliable connectivity, and connected intelligence [2]. Table 2.1 compares 6G with previous versions of wireless networks.

B5G and 6G will require new Key Performance Indicators (KPIs), besides the 5G KPIs. These systems are expected to increase the respective capability by a factor of 10-100 compared to the previous version [2]. The following KPIs is expected from 6G [16]: up to 1 Tbps peak data rate, 0.1 ms end-to-end latency, 20 years of battery lifetime, $100/m^3$ of connection density, $1000\times$ throughput increase, $10\times$ energy efficiency improvement, maximum outage of 1 in 1 million devices, and positioning precision of 10 cm in indoor and 1 m in outdoor. These KPIs can be categorized into two groups: (i) technology and productivity driven KPIs, including KPIs for parameters such as jitter, link budget, extended range/coverage, position accuracy, energy and cost, and (ii) sustainability and societal driven KPIs, which are related to standardization, privacy/security, ethics, and intelligence. Some KPIs, such as capacity, throughput, latency, energy efficiency, and connectivity, are the basic requirements of all communications systems, while intelligence KPIs are newly designed for 6G.

2.1.1 Ubiquitous Enhanced Mobile Broadband

Evolving from 4^{th} Generation (4G) Long Term Evolution (LTE) networks to 5G communication systems, the eMBB supports a broader range of applications with higher quality. While the speed of eMBB is being greatly enhanced in 5G, compared to 4G [17], enabling new series of exciting immersive applications such as XR, 3-dimensional (3D) multimedia, and Internet of Everything (IoE), will require peak rate of tens of Gbps, which is beyond the 5G capabilities [18]. 6G mobile broadband need to be further improved to provide ubiquitous services with the peak of mobile broadband data rate at Tbps levels [2], [19], to provide high-definition contents to the end users.

Ubiquitous Enhanced Mobile Broadband (UeMBB) will enable use-cases like (i) super fast hotspots, where it can improve broadband services in very dense and populated regions such as public transportation or train stations [19]; (ii) Enhanced wireless multimedia, such as online 8K ultra-high definition video streaming and video gaming.

Multiple technologies will help 6G in supporting UeMBB. Fixed Wireless Access (FWA) will enable B5G networks to provide wireless broadband everywhere on the planet [20], where the Millimeter Wave (mmWave) links will be replaced by optical fibers to provide high data rate service, especially in remote areas. Terahertz (THz) communications are being considered one of the main frontiers for B5G networks that can offer the virtually unbounded capacity to support wide channels and super high data rates [21]. The increased complexity of modern networks prevents traditional optimization schemes from fully utilizing the available resources. Hence, Machine Learning (ML) has been proposed to be used in physical and Medium Access Control (MAC) layers [22]–[24] to optimize the resource and spectrum allocation, power control, Modulation and Coding Scheme (MCS), channel estimation, and beamforming.

2.1.2 Extremely Massive Machine-Type Communication

5G communications are supposed to support the connectivity of 1 million devices in 1 km^2, which allows millions of deployed sensors to collect and transmit their data. By entering to IoE era, this number will increase sharply, where a trillion automated sensors and actuators will connect and transmit their data back and forth through wireless links [25]. Existing traditional architectures will fail to support effective and efficient connectivity on such a massive scale. So B5G and 6G networks will need Extremely Massive Machine-Type Communication (emMTC) architectures to support connectivity in the scale of trillion of devices [26].

Several applications can be enabled by emMTC including smart buildings, smart industry, smart supply chain management [27], air and water quality monitoring, nature / wildlife monitoring and surveillance [28], [29]. Some of the new technologies, such as SigFox [30] and LoRa [31], will be among the potential candidates for connectivity and coverage in B5G era. Existing communication infrastructure, e.g., Radio Access Network (RAN), can also be considered in the design of new Machine-Type Communication (MTC) architecture in B5G networks. The following two technologies can be utilized in 6G to provide a more reliable and guaranteed service to MTC devices: (i) enhanced MTC, that provides high bandwidth data rate (e.g., up to 1 Mbps), with the support of high mobility for 6G-enabled applications like Internet of Vehicles (IoV); (ii) Narrow Band Internet of Things (IoT) (NB-IoT), which enables low data rate applications (e.g., in the order of Kbps) [19], [26]. The massive Multiple-Input, Multiple-Output (mMIMO) and Cell-free (CF) mMIMO can also be considered as potential candidates for MTC in B5G era, thanks to their enhanced efficiency of the spectrum in multi-user environments [32], [33].

2.1.3 Extremely Reliable Low-Latency Communication

URLLC provides a reliability of 99.999 in 5G systems [34], while some critical applications such as remote surgery will require even more reliable communications. By 2030, Extremely Reliable Low Latency Communication (eRLLC) communication with a reliability rate of 99.99999 is required to support applications like telemedicine, XR, internet of healthcare, and autonomous driving [7]. Various parameters must be considered in the design of eRLLC systems, such as fast end-to-end turnaround time, intelligent framing and coding, smart uplink and downlink communication, and efficient resource management [35].

2.1.4 Super Low-Power Communication

While the integration of traditional devices with large-scale antenna arrays brings high power consumption [36], increasing the number of connected devices in the following years will require highly efficient self-powered hardware to provide sustainable transmissions. 5G adopts multiple technologies to facilitate low-power communications such as back-scatter communication, hybrid analog / digital beamforming, sparse array, and sparse Radio Frequency (RF) link design [19]. Given the exponentially growing number of devices and traffic, these solutions may not bring enough power efficiency for 6G systems.

Multiple applications in 6G will require extremely low-power communications, including Unmanned Aerial Vehicles (UAVs), IoT and etc. Recently, Reconfigurable Intelligent Surface (RIS), also known as Intelligent Reflecting Surface (IRS), has been proposed as one of the enabling technologies for super low-power communication. Unlike the traditional relaying mechanisms, in RIS, no power amplifier is being used to amplify and forward the received signal, and it could potentially operate in entirely passive mode [36].

2.1.5 Long Distance and High Mobility Communication

Long Distance and High Mobility Communications (LDHMCs) is an essential requirement of large scale 6G networks [37]. While 5G provides service for high-speed vehicles and devices, i.e., high-speed trains up to 500 km / h, 6G will require LDHMCs services to support connectivity for the next generation of high-speed transportation systems. It is expected that 6G supports a mobility speed of more than 1,000 km / h [19].

2.1.6 High Area-Traffic Capacity

Area-traffic capacity refers to the total traffic throughput per geographic area (bit / s / m^2) [38]. It is expected that 5G supports the area-traffic capacity of 10 Mbps / m^2. However, some applications like 3D multimedia or collaborative video gaming require higher traffic capacity, which might be beyond 5G capacity. Hence, 6G needs ten times improvement over area-traffic compared to 5G to reach up to 1 Gb / s / m^2 for real-world applications [37].

2.2 Emerging 6G Applications

The NextG wireless communication systems are expected to support new applications and services that will build a fully connected and digital world. This section summarises some of these emerging applications.

2.2.1 Internet of Everything

The IoE will expand IoT to include things, data, people, and processes [19], [39], [40]. It integrates various sensing devices for identifying, monitoring, and controlling “everything” in an intelligent way. The range of sensory data includes position, light, speed, temperature, and pressure and can be used in various applications, from smart cities to healthcare and smart industry. 6G will be the key enabler for IoE by providing seamless connectivity to a massive number of machine-type communication and sensory devices [41]. The integration of 6G and IoE will support new applications by providing better service to IoT, wireless body area networks, smart grids, and smart cities, which all will work together to improve the quality of life. 6G needs to provide reliable low-latency connectivity for a massive number of devices to be able to support IoE [19].

2.2.2 Connected and Autonomous Vehicle

Researchers have explored and investigated the connected and autonomous vehicles paradigm for years in academia and industry. This paradigm consists of several technologies such as autonomous driving, cooperative vehicle networks, IoV [42], Vehicular Ad-hoc NETworks (VANETs) [43], road-side communication networks [44]. Integrating with AI-powered autonomous vehicles, 6G networks will pave the way for Intelligent Transport System (ITS) and intelligent Vehicle-to-everything (V2X) communications [19], which will change the shape of urban transportation by introducing driver-less taxies, cars and public transportation [45]. 6G networks will unleash the full potentials of V2X communications, by providing ultra reliable and low-latency ($\leq$ 0.1ms) communications.

2.2.3 Industry 5.0

Industry 5.0 refers to a human centric design solution where humans work together with collaborative robots (cobots), and intelligent machines add personal human touch to industry 4.0 pillars of automation and efficiency [46]. The cobots replace human workers in repetitive and dangerous tasks to preserve human workers' safety and health [47]. The key enablers of Industry 5.0 include cloud / edge computing, big data, AI, and IoE, as it was in Industry 4.0. In Industry 5.0 era, a massive number of intelligent and connected devices support various services and applications that are enabled by 6G which fully integrates cloud / edge computing, big data, IoE and AI.

2.2.4 UAV-Based Mobility

UAV-based communications will play an important role in the next generation of wireless communications, thanks to their unique features compared to fixed terrestrial equipment, such easy and fast deployment and Line-of-Sight (LoS) connectivity [48]. UAVs have been recently considered in some applications such as natural disaster management, traffic surveillance, agriculture, and environmental monitoring and mapping [49], [50]. UAVs can also play an important role in the integration of 6G and IoE, adopting the UAV-to-Everything (U2X) communications. U2X network still faces some critical challenges like efficient radio resource management, power transmission, and trajectory design [19].

2.2.5 Extended Reality

XR is a collective term that extends across immersive technologies including Augmented Reality (AR), Virtual Reality (VR), Mixed Reality (MR), and everything in between [51]. XR fuse physical and virtual worlds using various wearable sensors and computers to encode human-machine interactions. XR requires the processing of sensory data regarding location, orientation, and acceleration, which requires a very reliable, low latency, and high data rate connection to provide a fully immersive experience [19].

2.2.6 Holographic Telepresence

Holographic Telepresence (HT) consists of a real-time 3D projection of distant people and objects with a high level of resolution and fully-motion support [52]. In HT systems, the transmitter captures the footage of surrounding people and objects and compresses and sends them to the receiver over a broadband network. This information then decompresses by the receiver and is projected by laser beams to create a 3D vision of the original object. Several applications can be imagined for HT, including 3D video conferencing and news broadcast [19]. HT requires 0.1 ms latency and multi Gbps data rate to provide an immersive and seamless experience [3].

2.3 6G Enabling technologies

Several technologies and ideas have been proposed to handle the massive traffic growth and the increasing number of connected devices in B5G and 6G networks, such as exploring beyond sub-6 GHz frequencies (mmWave, THz), mMIMO and cell-free mMIMO, RIS, Large Intelligent Surface (LIS) and UAV communication systems. While some of these technologies have already existed in 5G communications, they need multi-fold improvement to handle 6G requirements.

2.3.1 Beyond Sub-6 GHz Communication

The increased traffic and data demand and the limited resources in the sub-6 GHz frequency range led researchers to explore the possibility of using higher frequency bands for data transmission. mmWave frequency band (from 30 GHz to 300 GHz) has already been explored and standardized for indoor (Gigabit WiFi) [53] as well as outdoor cellular networks. Thanks to the abundantly available bandwidth,mmWave radio technology is currently a suitable candidate for data-hungry applications in 5G, such as wireless office docking, Ultra High Definition video streaming, wireless AR and VR, mobile front-hauling and offloading, etc. [54]. Due to the propagation characteristics over mmWaves, most of these applications are suitable for controlled indoor environments. The usage of mmWave in complex outdoor environments, instead, is still limited to some use cases like FWA with fixed transmitters and receivers. Some critical problems need to be solved, and more efficient solutions, i.e., very fast beamforming and beam tracking schemes, need to be proposed to use mmWaves in more complicated scenarios such as mmWave roadside communications [55], [56].

Some B5G applications such as wireless Brain Computer Interface (BCI), HT, and XR require data rates in the range of Tbps, which is beyond the capacity of mmWave systems [57]. Researchers recently have been exploring the THz frequency band for data transmission, especially for super high data rate communications with zero error rate in short distances [2], [19], [58], [59]. THz band, also known as submillimeter radiation, refers to the frequency band from 100 GHz to 10 THz, with the corresponding wavelength from 0.03 to mm-3 mm. The critical characteristics of THz communications include widely available bandwidth to enable very high data rates

and high propagation loss and sensitivity to blockage, which makes the use of highly directional antennas indispensable [5].

Designing proper beamforming and beam alignment techniques is critical to unleashing the full capacity of THz communications. The narrow beams will also reduce the co-channel interference among different users and so can further improve the performance. Because of the shorter wavelength in THz communications, compared to mmWaves, a huge number of antennas can be deployed in the same size area, generating a more directional and higher number of beams.

2.3.2 Machine Learning and Federated Learning

AI and ML will play a fundamental role in 6G communications [60]–[66]. AI / ML will be partially supported by 5G systems. However, native-AI will be an essential part of 6G, enabling the full potential of radio signals and paving the way to the transformation from cognitive radio to intelligent radio. Advances in ML will create intelligent and more efficient networking that will fully utilize the resources to improve the Quality of Service (QoS) for end users. ML can perform complex networking tasks such as handover, network selection, and resource management. It will also play a critical role in IoT, MTC, Machine to Machine (M2M), human-to-human and machine-to-human communications [2]. Native-AI will be supported by metamaterials, smart infrastructures, intelligent devices, intelligent cognitive radio, and sustainable networks [2]. ML will take the place of traditional approaches in physical and MAC layers such as RF signal processing, spectrum sharing, encoding / decoding, channel estimation, power control, and MCS. ML approaches will also be considered in the link layer and transport layer for resource allocation and traffic prediction and control tasks.

Federated Learning (FL), has been recently proposed as an AI concept to leverage on-device processing power and improve the user data privacy [67]–[71]. The idea is to collaboratively train a shared model so that the participating devices train the local model and share updated weights with the central server that combines different models. FL techniques can be categorized in three groups, horizontal FL, vertical FL and federated transfer learning [72]. FL is proposed as an answer for the problems of centralized data collection and processing frameworks such as privacy and huge communication overhead [67].

2.3.3 Unmanned Aerial Vehicles

Drones or UAVs are recognized as an essential part of B5G wireless communications. Thanks to their unique characteristics such as easy deployment, strong LoS links, degree of freedom, and controlled mobility [2], UAVs as flying or aerial Base Stations (BSs) can provide better service compared to traditional fixed infrastructures. In emergencies and natural disasters such as earthquakes and floods, where the terrestrial infrastructure is destroyed and becomes unfunctional, the UAV networks can be easily and quickly deployed to provide connectivity and help manage the disaster. UAVs can also be used in other scenarios, as for increasing network connectivity and coverage, on-demand broadband, environment and nature monitoring, pollution monitoring, security and surveillance, and road traffic monitoring. UAV communication will bring a

new paradigm to the wireless communication industry. A swarm of UAVs can collaborate to overcome the limitation of UAVs operating as individual nodes in increasing the network coverage to provide better service to ground users [73]–[75]. Given the limitation of UAV such as limited payload, flight time, and communication range [74], a swarm of UAVs, where the nodes are working together and are aware of the situation of each other, can provide more sustainable communication.

2.3.4 Large Intelligent Surfaces

LIS, also known as metasurfaces, RIS, IRS and Software Defined Surface (SDS), consist of many reflecting diode units that can reflect any incident electromagnetic signals by an adjustable phase shift [12], [13], [76]–[80]. In the 6G era, very large intelligent surfaces will provide a controllable propagation environment. LIS can play a critical role when the LoS link is blocked or experience low quality by turning artificial structures, e.g., buildings, into intelligent and electromagnetically active wireless environments that can control propagation characteristics like reflection, scattering, and refraction [81], [82].

Fractional programming and gradient descent can be employed to optimize the transmit power and intelligent surface phase shift, respectively [2]. LIS are a potential solution to maximize data rate and minimize the transmission power in B5G networks. It is expected that LIS will go beyond traditional mMIMO and provide advantages such as reduced noise, lower interuser interference, and reliable communications for 6G networks.

2.3.5 Cell-Free massive MIMO

Network densification is a common technique to increase the network coverage and rate for the User Equipments (UEs). Densification can happen both by increasing the number of the BSs, a.k.a. Ultra Dense Networks (UDNs), or the number of antennas at the BS, a.k.a. mMIMO. Each of these approaches suffers from some shortages: deploying a large number of BSs increases the inter-cell interference and hence reduces the service quality for the UEs, while in the mMIMO, UEs located at the edge of the cell suffer from high propagation loss because of the long distance from the BS.

Distributed or CF mMIMO [14] has recently been introduced as an answer to the limits of the technologies mentioned above by adopting the best of both. Distributed or CF mMIMO [14] has recently been introduced as an answer to the limits of the technologies mentioned above by adopting the best of both. In CF mMIMO systems, a huge number of geographically distributed antennas are coherently working together to serve users in their coverage area. The massive antenna arrays in mMIMO systems provide a very high beamforming gain and spatially multiplexing of users, increasing the spectral and energy efficiency and enhancing the reliability [83]. Distributed nature of CF mMIMO provides additional macro-diversity by implementing coherent user-centric transmission that eliminates the inter-cell interference limitation in cellular networks [84], which can considerably improve performance. CF mMIMO has been considered one of the enabling technologies for B5G communications [15], [85], [86].

2.3.6 Non-Terrestrial Communications and 3D Networking

The ground networks will be integrated with airborne and Non-Terrestrial Network (NTN) in 6G to support communications for the users in vertical extension [2]. This 3D networking paradigm will be enabled by Low Earth orbit (LEO) satellites and UAVs [87], [88]. Adding the dimension in terms of altitude makes connectivity in 3D networking considerably different and more challenging than for conventional 2-dimensional (2D) networks. Integrating ground networks, satellites, UAVs in 6G will provide global connectivity and stringent seamless access across the globe. Developing protocols and architectural solutions for New Radio (NR) operations in NTNs is considered in 3rd Generation Partnership Project (3GPP) Rel-17 and then further expanded in Rel-18 and Rel-19 [89].

2.3.7 Quantum Communication

Quantum systems play a role in wireless communication and networking in two different ways: quantum communication and quantum computing. Quantum communication is transferring a quantum state from sender to receiver, which enables the execution of a task that is difficult, if not possible, for classical techniques [90]. Quantum communication will bring advantages to next-generation wireless systems, such as quantum key distribution, quantum secure direct communication, and quantum teleoprations [91]. Quantum communications and quantum computing technologies will provide rigorous security against various cyber-attacks by applying a quantum key based on the quantum no-cloning theorem and the uncertainty principle. The information will be encoded in the quantum state by quantum particles or photons, which can not be accessed or cloned without tampering it due to quantum principles [92].

2.3.8 Other Technologies

Many other technologies can be listed as 6G's potential enablers. Visible Light Communication (VLC) as one of the promising optical wireless communication technologies that use visible lights (frequency spectrum from 430 THz to 790 THz), will be used to support super-fast short-range communications [6], [93]–[95]. Because of its built-in strong security nature, Distributed Ledger Technologies (DLTs) and in particular Blockchain technology, have turned out to be an up-and-coming technology in 6G era [96]–[99]. It can enhance the 6G's technical aspects, such as dynamic spectrum sharing, resource and mobility management, as well as enabling unforeseen applications like HT, XR and Industry 5.0 [19]. Integrated sensing and communications [100]–[106] is another enabling technology for 6G. A key driver of autonomous wireless networks is continuously sensing the state of the changing environment and exchanging information among different nodes. Hence, in 6G, the sensing will be tightly integrated with communication to support this autonomy. Ambient backscatter wireless communication allows interaction between two battery-less devices by only using existing RF signals as the source of power [107]–[109]. Backscatter communications can provide a reasonable data rate for short-range communications. It can be used to transmit small monitoring signals by the sensors without consuming any power. The

battery-less devices in the backscatter communications make it a potential candidate for massive machine-type communications in the future 6G networks.

3

The challenges of Scheduling and Resource Allocation in IEEE 802.11 ad / ay

3.1 Introduction

Wi-Fi is nowadays present in many devices and is common in households, offices, public institutions, and transportation. Over more than 20 years, many amendments have been made to the original standard, updating both the Physical Layer (PHY) and Medium Access Control (MAC) layers to provide higher bit-rate, robustness, and Quality of Service (QoS).

As users keep asking for higher data-rates, the current deployments struggle to keep up with the demand. One key enabler for gigabit-class communications is the use of the Millimeter Wave (mmWave) band, which loosely refers to the portion of the electromagnetic spectrum with frequencies higher than 6 GHz. In this frequency range, the amount of available bandwidth is significantly larger than that of the legacy sub-6 GHz counterpart, allowing unprecedented transfer speeds.

As the research started to mature, the Wi-Fi Alliance introduced in 2012 the IEEE 802.11ad amendment [110], standardizing communication in the 60 GHz Industrial, Scientific, and Medical (ISM) unlicensed band, offering data-rates up to 6.75 Gbps. As a follow-up, its successor IEEE 802.11ay is planned to be standardized by the end of 2020 [111], introducing technologies such as Multi-User Multiple Input, Multiple Output (MU-MIMO), channel bonding, higher-order modulation, and thus even higher speeds. Such extreme data-rates make it possible to unlock new applications, such as wireless office docking, 8K Ultra High Definition video transfer, wireless Augmented Reality (AR) and Virtual Reality (VR), mobile front-hauling and offloading, etc. [54].

On the downside, given the higher carrier frequency, mmWave transmission suffers from an increased propagation loss, as well as deeper diffraction shadows, and higher penetration and

reflection losses, making communication more difficult and less stable.

On the other hand, these characteristics allow for extreme spatial reuse, e.g., transmissions in different rooms will hardly interfere with each other unlike in legacy Wi-Fi. Moreover, the short wavelength makes it possible to use antenna arrays with tens of elements packed in a small area, making it is possible to counteract the increased path loss by focusing the radiated power into directive beams, thus increasing the overall antenna gain. While this further reduces interference even where users share the same area and improves spatial reuse, it also creates the problem of directional deafness, worsens the hidden node problem, and makes mobility more complex to handle.

To meet the strict QoS requirements of some new applications and partially alleviate the hidden node problem, the standard provides the possibility to transmit data in reserved contention-free periods, that coexist with contention-based access periods, very similar to the legacy Carrier Sense Multiple Access with Collision Avoidance (CSMA / CA) channel access mechanism, and the hybrid allocation can be flexible enough to support the coexistence of traffic with vastly different QoS requirements.

In this chapter, we present some of the challenges related to the scheduling of IEEE 802.11ad / ay devices in realistic scenarios, with the main focus on the already-standardized IEEE 802.11ad. Furthermore, we discuss some pre-existing works and propose some research directions.

In particular, in Section 3.2 the main characteristics of IEEE 802.11ad will be described. Section 3.3 will briefly discuss the literature on channel access and scheduling. Section 3.4 will showcase our research plan, and finally Section 3.5 will draw the conclusions.

3.2 IEEE 802.11ad Overview

To introduce the main concepts and nomenclature of IEEE 802.11ad, in this section we provide a short summary of the standard [110], while referring to other sources for more details [112].

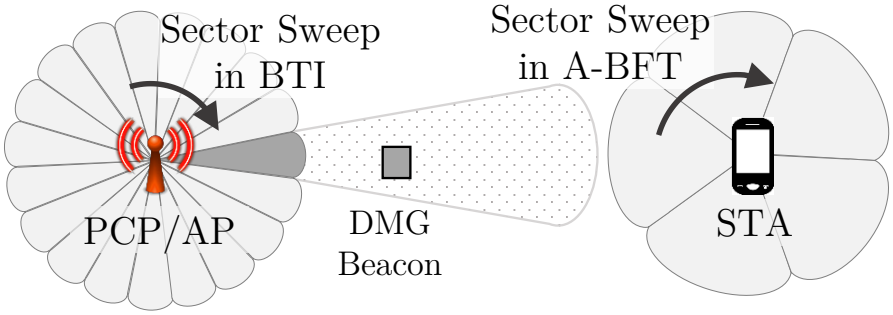

Figure 3.1: Graphical representation of sector structure in IEEE 802.11ad.

Being a mmWave-based standard, directional communication with all the added overhead and the possibility of spatially multiplexing users are included in the amendment. To simplify beam management, both the Personal Basic Service Set (PBSS) Central Point / Access Point (PCP / AP)

and the Stations (STAs) divide their surrounding space into sectors as shown in Fig. 3.1. STAs and PCP / AP will then need to keep beam alignment, which increases the signaling overhead.

Fig. 3.2 shows that in IEEE 802.11ad time is divided in Beacon Intervals (BIs) of about 100 ms. Each BI is further divided into Beacon Header Interval (BHI) and Data Transmission Interval (DTI), briefly described in the following sections.

3.2.1 Beacon Header Interval

The PCP / AP does most of the managing, such as beaconing, beamforming training, and scheduling, during the BHI. This period can last hundreds of microseconds up to a few milliseconds, and is further divided into three subintervals: Beacon Transmission Interval (BTI), Association-BeamForming Training (A-BFT), and Announcement Transmission Interval (ATI).

The BTI is used to send Directional Multi-Gigabit (DMG) Beacons to announce the network, give the basic synchronization and BI structure information, start the beamforming training with new stations, and, if needed, do some basic traffic management. Beacons are sent over the different sectors, covering all possible directions to maximize coverage for untrained STAs.

After receiving a DMG Beacon during the BTI, new STAs can use the A-BFT to complete the basic beamforming training by sending Sector Sweep (SSW) frames in different sectors. Beam alignment is completed once the PCP / AP responds with an SSW Feedback.

Finally, advanced scheduling mechanisms setup and further network management can be done during the optional ATI.

3.2.2 Data Transmission Interval

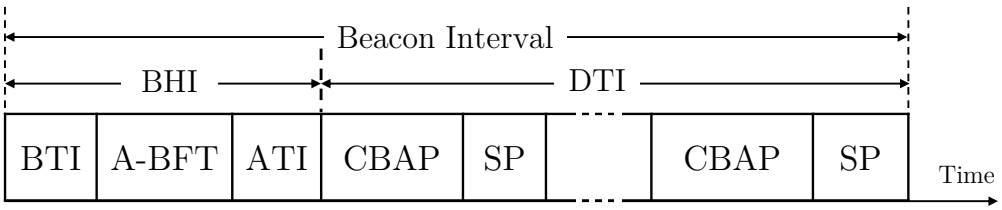

Figure 3.2: Representation of a Beacon Interval (BI).

The DTI is mainly used for the actual data transmission, but it can also be used to improve communication links and for further scheduling. The DTI comprises Contention-Based Access Periods (CBAPs) and Service Periods (SPs), which can appear in arbitrary combinations and are scheduled during the BHI.

Transmission in Contention-Based Access Period (CBAP) follows the rule of Enhanced Distributed Channel Access (EDCA), slightly modified to account for directional transmission, in which STAs compete with each other in order to transmit their data.

Instead, Service Periods (SPs) are scheduled contention-free intervals that are dedicated to exclusive transmission between a pair of STAs* to guarantee QoS. The standard also allows for spatial sharing, meaning that multiple pairs of STAs with low cross-interference can be scheduled in the same SPs. This, however, comes at the cost of increased overhead since interference measurements must periodically take place.

3.3 Scheduling in IEEE 802.11ad

IEEE 802.11ad allows for great flexibility in the scheduling of radio resources, but we will hereby describe only some of these possibilities in their simplest form.

We want to stress the fact that, unlike in traditional contention-based medium access, scheduled SPs guarantee QoS. Access Categories (ACs) introduced in 802.11e, in fact, only allow for stochastic traffic prioritization according to the DiffServ paradigm, which ceases to work in congested networks. For this reason, allocated traffic is especially important for those applications with strict QoS constraints. Instead, more realistic applications, such as data transfer or asynchronous bursty traffic, can simply rely on CBAP.

As shown in Fig. 3.3, a STA can set up an allocation by sending an Add Traffic Stream (ADDTS) Request frame to the PCP / AP during the DTI and embedding a DMG Traffic Specification (TSPEC) element. The DMG TSPEC element is created by the requesting STA and comprises information such as the allocation period, and the minimum and maximum allocation duration.

Based on its admission policy, the PCP / AP will either reject or accept the request, immediately notifying the requesting STA via an ADDTS Response. If accepted, the allocation is made effective by including it in the Extended Schedule Element (ESE) transmitted in the next DMG Beacons, which will contain details such as the effectively allocated period duration and the SP start time. In this way, STAs not involved in the communication will not create interference and will be able to switch to power-saving mode. Otherwise, the PCP / AP can either reject or propose a change in the DMG TSPEC. A STA can later update the DMG TSPEC by sending another ADDTS Request with the updated element and follow again the same procedure.

Allocating the right duration to SPs is clearly a trade-off between QoS traffic, which needs resources to fulfill the minimum requirements imposed by the application, and elastic traffic, which still needs resources even though with less stringent requirements. Since resource availability, as well as channel quality, are time-varying, the standard supports SP extension and truncation services, which let the stations keep transmitting and / or relinquishing the unused occupied channel. Still, these features bring extra overhead and should thus be used carefully.

A mathematical model for preliminary allocation of SP for Variable Bit Rate (VBR) flows is presented in [113], which helps determine how to set the TSPEC parameters to meet QoS requirements while minimizing the amount of allocated time. Unfortunately, SPs are assumed to be placed at the beginning of the DTI, which is not possible in general for applications with tight de-

*A PCP / AP also contains a STA, i.e., a logical entity that is a singly addressable instance of a MAC and PHY interface to the wireless medium [110].

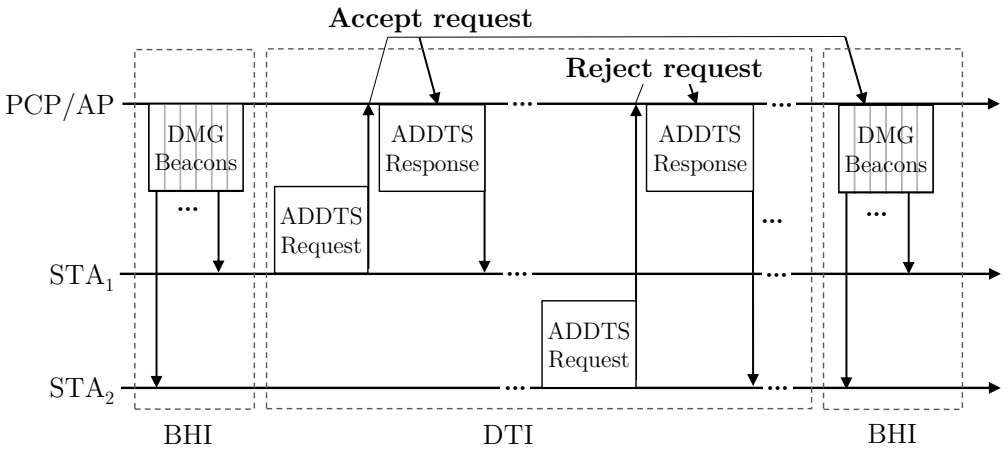

Figure 3.3: Representation of ADDTS scheduling in IEEE 802.11ad.

lay constraints. For example, for virtual or augmented reality services, latencies should be below 20 ms to avoid motion sickness.

Other works in the literature consider different aspects of the DTI. For example, [114] derives the theoretical maximum throughput for CBAPs when two-level MAC frame aggregation is used. Beamforming is also considered in [115], which proposes a joint optimization of beamwidth selection and scheduling to maximize the effective network throughput, while other works, though not specifically concerning IEEE 802.11ad, deal with transmission scheduling for mmWave communications [116].

3.4 Future Research

In this section, we highlight some possible research directions. In particular, in Section 3.4.1 we describe the main tools that are currently available to study the subject. Then, in Section 3.4.2 we propose a possible research plan.

3.4.1 Available Research Tools

Although commercial devices supporting the IEEE 802.11ad standard are currently available, manufacturers do not provide tools to access low-level functionalities. Ultimately, it is more flexible, timely, and cost-effective, although arguably less realistic, to simulate the behavior of such devices.

In particular, significant effort has already been done implementing the IEEE 802.11ad standard into Network Simulator 3 (ns-3) [117], a popular open-source network-level simulator. The last release of the simulator also supports quasi-deterministic channel modeling based on ray-tracing, making simulations extremely accurate and realistic at the cost of a long preliminary channel generation phase, although some works already tried to improve this aspect [118]. While

the implementation already covers most parts of the standard, it is still missing the scheduling mechanisms necessary for this project. The authors of [117] are also working on the implementation of the IEEE 802.11ay amendment [119], making their work even more valuable.

Historically, scheduling algorithms have been mainly based on heuristics, trying to balance performance and adaptiveness versus complexity. In the last years, instead, the Machine Learning (ML) revolution has brought many innovations also to the telecommunication field at all layers of the stack and, in particular, Reinforcement Learning (RL) is especially applicable to optimize or even replace legacy scheduling algorithms [120]. Following the principle of self-driving networks [121], ML algorithms can learn from real on-line data and supersede manually-designed protocols, which are becoming increasingly complex. OpenAI Gym is one of the most used RL toolkits and has been adopted by all popular ML frameworks. Given their potential in many fields of networking and telecommunications in general, OpenAI Gym APIs have also been integrated into ns-3 [122] with the name of ns3-gym.

With these powerful tools, it will be possible to further advance the state of the art, create a comprehensive performance evaluation of available algorithms and further improve upon them once the weak points are clearly identified.

3.4.2 Research Plan

One of our first goals is to extend the already existing IEEE 802.11ad ns-3 module with the necessary mechanisms to make it properly support the hybrid channel access and advanced scheduling (see Section 3.4.1), and add the support to the ns3-gym framework. A significant development effort will be put into the creation of a proper simulation environment, with particular attention to the computational complexity since a high data-rate simulation of just 10 s of simulated time may currently take one hour or more of run-time. This makes the design, evaluation, and optimization of scheduling protocol a lengthy process, which may be even infeasible if RL is involved since many training episodes are needed to learn even basic mechanisms.

Indeed, decisions such as admission policy, resource allocation, smart SP truncation or extension, and spatial sharing are often difficult to accurately model in terms of trade-offs and usually comprise several tunable parameters. However, if trained correctly, an RL agent is often capable of learning extremely complex rules and optimize the network for different networking metrics (e.g., delay, jitter, throughput, fairness) even beyond complicated heuristics.

Resource allocation can be divided into two subproblems. Specifically, STAs have to translate information given by the application into DMG TSPEC elements and the PCP / AP subsequently has to efficiently schedule the DTI especially considering the Modulation and Coding Scheme (MCS) used. Regarding the former, applications may not yield constant inter-packet arrival time (e.g., frame-rate drop in video applications) nor packet size (e.g., when compression is considered). At the same time, transmission conditions may vary mainly due to environmental changes, mobility, or even blockage, thus increasing performance variability. If QoS requirements are not met, the RL agent of a STA could thus update the TSPEC.

On the other hand, the PCP / AP has to allocate SPs for a BI based on the available resources.

Effective scheduling must take into account, in addition to network metrics, the possible evolution of the MCS since the packet transmission time largely depends on it. Given the significant differences in channel dynamics of IEEE 802.11ad with respect to sub-6 GHz Wi-Fi, new ones can be proposed to account for the specific characteristics of the mmWave channel. An RL agent could thus jointly adapt the MCS and perform scheduling to optimize the network performance by observing the evolution of both channel statistics and network traffic.

One way to overcome the problem of slow simulations is to quickly pre-train the RL agent to make it learn at least simple decisions, such as understanding when a new request does not fit the available resources, avoid overlapping SPs during scheduling, and avoid scheduling highly cross-interfering users with spatial sharing. Thus, we plan to build a very simple and fast simulator that will only model relevant notions, e.g., basic channel and traffic modeling and the BI structure defined in IEEE 802.11ad, but eliminating the fine details which make ns-3 realistic but extremely slow. In this way, the agent can learn very broadly which actions it should take and then fine-tune its behavior via more realistic simulations. Then, to further decrease ns-3 simulation runtime, a database of simulation results can be created and multiple agents can passively learn from it [123] before fine-tuning their performance on ad hoc simulations. Transfer learning will also be considered to speed up convergence to effective policies in different scenarios.

Another objective will be to understand the traffic behavior of target applications. For example, it could be possible to acquire real-world traffic traces of AR / VR applications, characterizing and modeling their traffic patterns with focus on packet size, and variability of inter-packet arrival accounting for variable frame-rate statistics. These models would ultimately be integrated with standardized scenarios [124], [125] to further increase simulation realism.

Furthermore, understanding how the current state of the art performs in a realistic simulator will allow understanding the strong and weak points of the proposals in realistic settings. From detailed studies, it will be possible to understand how the state of the art can be improved upon with heuristics or, when modeling becomes too complex or inaccurate, ML-based approaches.

These results will then be easily transferred to the future IEEE 802.11ay standard, which will add further complexity on top of the already existing one, by introducing channel bonding and MU-MIMO. Even more complex schedulers will then have to be designed, but starting from the solid ground of the proposed work further improvements will be possible.

3.5 Conclusions

In this chapter we briefly described the main characteristics of IEEE 802.11ad, mainly focusing on the MAC layer and especially on the newly introduced scheduling mechanisms, allowing different types of traffic to coexist and potentially improving the performance of QoS-sensitive applications. As shown in Section 3.3, some research has already been done in this direction but lacks a common and realistic testing ground, making it unclear whether the assumptions may hold.

Our future work will focus on proposing solutions for the many open problems described in Section 3.4.2. Models and source code that will be considered of interest for the community will

be published, making it possible to fairly compare results from different groups in a common and realistic simulation environment.

4

Performance analysis of mmWave Cellular Networks

4.1 Introduction

The abundant free spectrum available at Millimeter Wave (mmWave) frequencies, spanning from 30 GHz to 300 GHz, makes mmWave communication a key enabler for 5th Generation (5G) systems to support bandwidth-hungry applications like online High Definition video streaming, augmented and virtual reality, and road-side vehicular communications.

However, transmission over mmWave bands has its unique characteristics and adds new challenges, which are very different from those of sub-6 GHz communications. In the last decade, a massive body of research has been carried out to understand and model mmWaves' propagation properties, mainly focusing on path-loss models, ray propagation mechanisms, material penetration, and atmospheric effects.

The first commercial 5G mmWave systems have already been deployed in the last two years, and some early measurements [126]–[128] investigated the performance of these systems under various urban scenarios, revealing a high variability in the systems' performance, partially attributed to the high sensitivity to the propagation environment. These studies are important because the commercial instalment may require to implement some changes, adaptations, and parameters' setting that were not be required nor tested in Proof of Concept (PoC) or pre-deployment phases and that may potentially affect the system behavior in certain situations. Evidence of such a risk was reported, for example, in [129] where the authors observed how an unexpected setting of some base station parameters had a dramatic impact of the energy consumption of narrowband-IoT nodes, significantly deviating from what predicted by models based on the protocol specifications. So, further research is required to fully understand the behavior of mmWaves

in an operational setup. To this end, we have conducted a measurement campaign to analyze the impact of different environmental phenomena like rain, water surfaces, foliage, and human body blockage on the performance of an operational 5G mmWave cell. We have also studied the signal coverage in different propagation environments for different sectors and beams. The purpose of this study is hence to understand to what extent the expected performance of mmWaves is fulfilled in commercial settings, with all the complexity of an actual cellular system and of a real-world environment. In many cases, our results confirm the system behavior already observed in previous studies based on non-commercial PoC deployments or predicted by theoretical models and simulations. However, in a few cases, we observed some nonconforming results that may be proxy of some problems in the deployment of the commercial solution.

The analysis of the measurement results provides guidelines for planning future deployments and predicting the performance of 5G in different use cases, such as in case of fish farms / aquaculture [130], or when the User Equipments (UEs) are located inside forests or vegetated areas [131], or when the Line-of-Sight (LoS) signal is blocked by buildings, moving objects or humans, as in dense urban environments [132]. Therefore, our observations are especially helpful to industries interested in deploying 5G over mmWave frequencies, but are not familiar with its intricacies.

In summary, our main contributions are as follows:

- We present the coverage analysis of a commercial 5G mmWave cell by measuring the Reference Signal Received Power (RSRP) in a complex real-world propagation environment (Section 4.4.1).

- We then analyze the beam separation and gauge the difference with respect to the sector-level transmission (Section 4.4.2).

- We study different environmental impacts from the body and foliage blockage to rain and over-water transmission on mmWave links on the commercial setup (Section 4.4.3).

- We analyze the performance of Non-Line-of-Sight (NLoS) mmWave links in two different sectors, representing urban and suburban areas, observing that in an urban environment with multiple buildings and reflecting elements, the NLoS components of mmWave signals can compensate for the lack of LoS links, while this is not the case in the suburban environment (Section 4.4.3).

- We analyze the effect of the above-mentioned scenarios on the performance of end-to-end transmissions (Section 4.4.3).

- We compare the measurement results with 3rd Generation Partnership Project (3GPP)'s statistical channel models for the urban and rural environment both for omnidirectional RSRP and transceiver's optimal antenna configuration, revealing the gap between the ideal simulated environment and the complex propagation environment (Section 4.5).

- Finally, we discuss how the above would affect real-world applications (Section 4.7).

Table 4.1: Related works

Ref.	Year	Scenario	Methodology	Contribution
[126]	2020	5G urban	Measurement (commercial)	Performance of end-to-end transmission
[127]	2021	5G urban	Measurement (commercial)	Performance, power consumption, QoS
[128]	2020	5G urban	Measurement (commercial)	5G performance in UE-side
[133]	2020	LoS indoor corridor	Measurement (testbed)	Path loss model
[134]	2018	LoS indoor office	Measurement (testbed)	Path loss / Large scale fading
[135]	2019	LoS / nLoS indoor	Measurement (testbed)	mmWaves channel characteristics
[136]	2017	Urban	Simulation / Measurement	Channel modeling
[137]	2017	Urban / Indoor	Measurement (testbed)	Spatio-temporal features of channel
[138]	2018	Urban	Measurement (testbed)	Feasibility of mobility
[139]	2020	Foliage / Suburb	Measurement (testbed)	Propagation characterization
[140]	2017	Foliage / Suburb	Measurement (testbed)	Propagation characterization
[141]	2017	Foliage / Suburb	Measurement (testbed)	Foliage propagation model
[142]	2019	Body blockage	Measurement (testbed)	Human blockage model
[143]	2019	Body blockage	Simulation	Hand grip impact
[144]	2019	Rain	Measurement (testbed)	Rain attenuation
[145]	2020	Rain	Measurement (testbed)	Rain attenuation
[146], [147]	2020	End-to-end urban	Simulation	Performance of TCP in mmWave
[148], [149]	2017	End-to-end urban	Simulation	Performance of TCP in mmWave
[150]	2019	Urban / Indoor	Simulation	Performance of TCP in mmWave

The remainder of this chapter is structured as follows: Section 4.2 reviews the existing literature around mmWave propagation and early 5G mmWave deployments. Section 4.3 describes the methodology used to conduct the measurement campaign. The observations and result analysis is provided in Section 4.4, and Section 4.5 compares the measurement results with some simple simulated scenarios. Section 4.6 summarize key findings and take-home messages and and finally, Section 4.7 concludes the chapter.

4.2 Related work

In the past few years, several studies have experimentally investigated the behavior of mmWave propagation in different scenarios and conditions: indoors [133]–[135]; urban environment [136]–[138]; suburban and vegetated area [139]–[141]; human body blockage [142], [143] and rain-induced fading [144], [145]. Further, [146]–[151] study end-to-end transmissions over mmWaves. Table 4.1 presents a summary of the related work.

The studies mainly aim to characterize the propagation of mmWave signals in different environments and under various circumstances. For example, the measurement study in [136] considered the outdoor 32 GHz microcells to extract and develop a mmWave channel model. The empirical result is then compared and validated through simulation. Ko et al. [137] investigated the wideband directional channel characteristic of mmWaves in both indoor and urban environments to model the spatio-temporal features of the communication channel. In [138], the authors investigate, through a measurement study, the feasibility of mobility for a typical vehicular speed in the urban environment.

The propagation of mmWaves in suburban and vegetated environments, surrounded by lots of foliage, is highly different from the urban and indoor scenarios. This matter has already been

considered in the literature, where a vast body of research studies the effects of foliage attenuation on mmWave propagation. A measurement study in [139] analyzes and extracts large-scale and small-scale propagation properties of 5G mmWaves in various vegetated environments with different types and density of vegetation. A real-time channel sounder is used in [140] to measure mmWave LoS and NLoS channel responses in a suburban area with lined trees. The authors then use the measurement results to generate a foliage propagation model based on the ITU-R terrestrial model.

The propagation of mmWaves can be highly affected by different phenomena like rain and human body blockage. 3GPP has recognized human body as one of the main obstacles affecting mmWave propagation and causing large radio channel variations. Human body blockage has been considered and modeled in the literature, based on Double Knife Edge Diffraction (DKED), wedge, and cylinder models. In [142], human body blockage is measured at 15 GHz, 28 GHz, and 60 GHz for 15 humans with different heights and weights. They model the body blockage as a Double-truncated Multiple Knife-edge (DTMKE) scheme and compare the calculated diffraction with existing models such as the absorbing double knife-edge model and the 3GPP human blockage model. The [152] is measured the human body shadowing at 28 GHz frequency and investigated its effect on Device-to-Device (D2D) devices in an outdoor environment.

The attenuation caused by precipitation can not be neglected at mmWave bands, where rain droplets can absorb mmWave signals whose wavelengths (1 mm to 10 mm) is comparable to the size of a raindrop (a few millimeters). Rain attenuation in the 21.8 GHz and 73.5 GHz bands, based on a one-year measurement campaign in tropical regions, is presented in [145]. In [144], Huang et al. employ a custom-designed channel sounder for 25.84 GHz and 77.52 GHz frequencies to measure the rain-induced signal attenuation for short-range mmWave links. To compare the performance result from the sub-6 GHz and mmWave frequency bands, the authors in [153] has been carried out channel measurements in 3-18 GHz in urban macro and micro-cellular environments. They have characterized path-loss, shadow fading, Root Mean Square (RMS) delay spreads and some other channel parameters for both LoS and NLoS communications. In the other work, the authors of [154] have performed measurements in 3.5 and 28 GHz. They have proposed a statistical channel model for large scale fading and analyze the channel characteristics for both sub-6 GHz and mmWave bands. The [155] has introduced a 28 GHz channel sounder that can be used with both horn antennas and phased array antennas. The authors have then extracted different multipath component properties such as path gain by comparing the antennas' speed when switching from one direction to another. They have also proposed passive reflectors and active repeater to improve the received signal strength and coverage. The [156] has presented a performance analysis for commercial sub-6 GHz 5G networks based on a cross-layer measurement study over 5G New Radio (NR) in an urban environment. They have analyzed the signal quality, coverage, and hand-off performance in the physical layer as well as end-to-end throughput, latency, user Quality of Experience (QoE) in niche applications, and energy consumption of the 5G smartphone.

From the user experience perspective, the efficiency of end-to-end transmission is critical when mmWave links are part of the network, as the unsteady physical channel makes it difficult to

support higher-layer connections. In [146], [147], Poorzare et al., presented an analysis of reliable end-to-end communications in 5G networks by investigating the effects of mmWave on Transmission Control Protocol (TCP) performance and discussed the factors impacting the performance of 5G networks. They further evaluated the performance of TCP in urban environments under different conditions. Polese et al. evaluated the performance of TCP over mmWave links, relying on simulation [148], [149]. They studied the behavior of multipath-TCP on 28 GHz mmWave links with a secondary Long Term Evolution (LTE) or 73 GHz mmWave link. Zhang et al. [150], analyzed the performance of TCP in mmWave networks for high-speed UEs in dense urban environments, where the UEs are located at different geographical positions with LoS and NLoS links to the Base Station (BS) as well as indoor UEs. They studied the performance of edge and remote servers as well as different TCP variations. The authors in [157] analyzed the effects of different types of blockages on congestion control mechanisms of transport layer protocol in the presence of handovers.

Most of the previous works were conducted in test setups that were not equipped with commercial 5G mmWave BSs since commercial mmWave deployments did not arrive until late 2019. Notable exceptions are studies by Narayanan et al. [126]–[128]. The study [126] presents a first look at the performance of two mmWave and one mid-band commercial 5G deployments in US. Using end-to-end performance measurements, Narayanan et al. tracked the interplay between propagation in the urban environment, blockage, and precipitation on applications performance. They further expand their measurement campaign in [127] to include the power consumption and application QoE of operational 5G networks by considering different deployment schemes, radio frequencies, protocol configurations, mobility patterns and upper-layer applications. They also investigate the possibility of predicting network throughput in commercial mmWave 5G networks [128]. That work identified the different factors that affect 5G performance and proposed a context-aware throughput prediction framework based on Machine Learning techniques.

Xu et al. presented a performance analysis for commercial sub-6 GHz 5G networks based on a cross-layer measurement study over 5G NR in an urban environment in China [156]. They have analyzed the signal quality, coverage, and hand-off performance in the physical layer as well as end-to-end throughput, latency, user QoE in niche applications, and energy consumption of the 5G smartphone.

Like the work of Narayanan et al., we present an evaluation of a commercial 5G cell deployment. However, to the best of our knowledge, this chapter is the first to provide a fine-grained analysis of mmWave propagation of a commercially deployed BS. This offers concrete explanations for the main causes of performance degradation since we are not treating the radio as a black box. We have also investigated a range of scenarios that are known to impact mmWave propagation, including human body blockage, foliage, transmission over-water and rain. While some of these have been investigated before, this chapter is the first to analyze all of them in a commercial 5G mmWave deployment with known parameters configuration. We also note that this chapter is the first to look at the effect of transmission over-water. We further compare the measured RSRP against 3GPP's statistical mmWave channel models for the urban and rural environments, considering both omnidirectional strongest RSRP (transceiver's optimal antenna configuration),

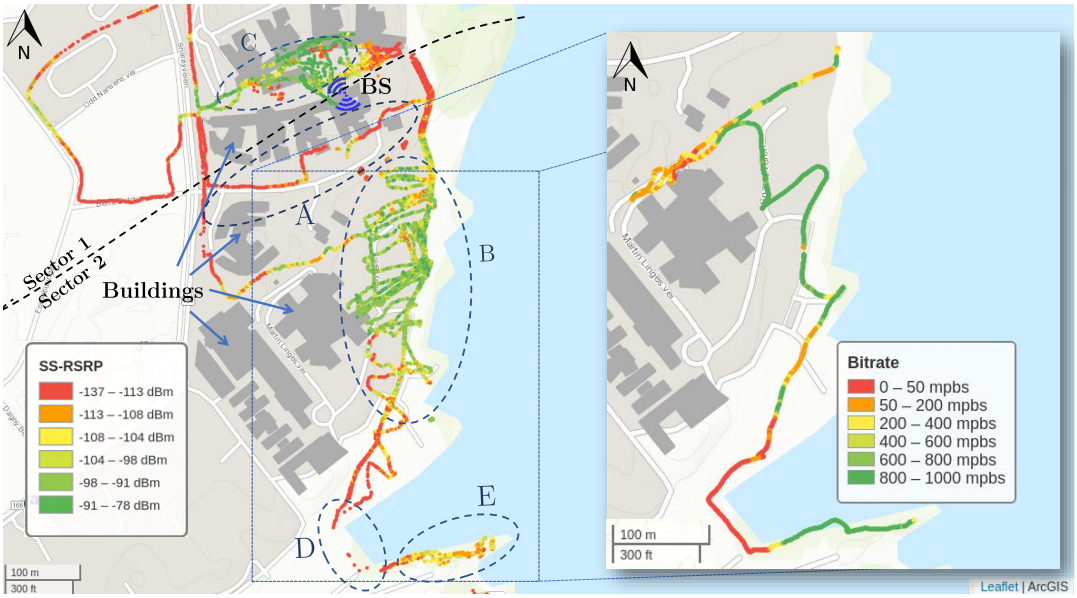

Figure 4.1: Signal coverage map of the cell site, showing the maximum RSRP among all beams and PCIs. The zoomed-in area presents the bitrate.

to study the simulation and actual performance (Section 4.5).

4.3 Measurements Methodology

This chapter includes two measurement studies: the first study aims to analyze the coverage aspects of commercial 5G mmWave cells, while the second study targets the end-to-end communication performance of a 5G network when mmWave links are employed as part of the system.

The 5G mmWave BS is located on the roof of a 15 meters high building in Telenor's campus in Oslo, Norway. The BS is equipped with two Huawei HAAU5213 radio frequency units with 768 antenna arrays providing coverage to a northern and a southern sector as shown in Figure 4.1. Its frequency range is 26.5 GHz to 29.5 GHz with a maximum transmit power equal to 32.5 dBm. It supports up to four carriers and can generate 16 different static beams, employing hybrid beamforming. The black dashed line in the Figure 4.1 showcases the topological separation of the two sectors. The northern sector (sector 1) points towards an open square surrounded by glass and steel buildings. The southern sector (sector 2) is directed towards a peninsula with some buildings on the west and sea on the east. Each sector has four 200 MHz wide channels (800 MHz total), with center frequencies between 26.6 GHz and 27.2 GHz. We identify each channel by its respective Physical Cell Identity (PCI), where PCIs 101-104 belong to the northern sector and PCIs 301-304 to the southern. The operator can adjust the beams' boresight both in the horizontal and vertical plane. We did not have any control of the beams and no prior knowledge about their directions. However, we were able to estimate the beams' directions based on the measurements we collected to create the coverage map from LoS scenarios, if a single beam has the highest RSRP

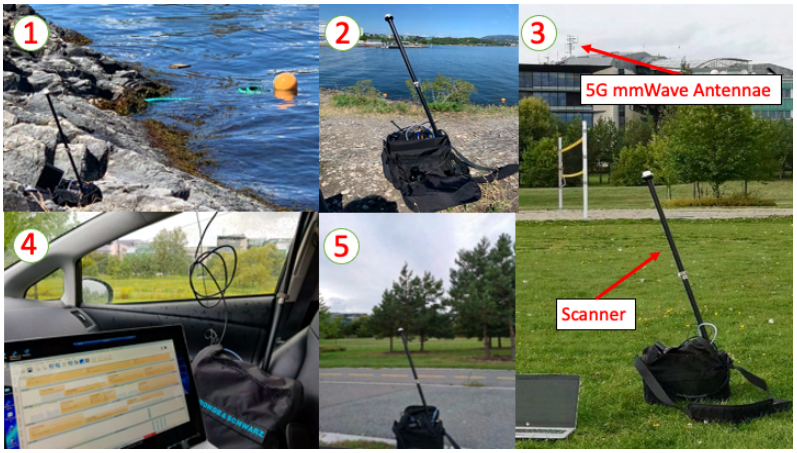

Figure 4.2: Some measurement locations: 1) close to water, 2) 6 m above water, 3) Line of Sight, 4) rain, 5) foliage blockage.

in all locations of a measured area is considered to have an orientation towards this area.

We collect channel quality information with a Rohde & Schwarz scanner[158] that can monitor all the relevant channels simultaneously using an omnidirectional antenna. Note that our measurements do not consider the antenna gain that is expected in a commercial receiver (e.g., as smartphone). On the other hand, the isotropic antenna makes the measurements almost independent of the receiver orientation. Since we are interested in how different factors affect propagation, the absence of the receiver gain does not influence our evaluation. The scanner was used to gather measurements across the site and under different conditions, collecting in total 535137 samples between April 2020 and September 2020. Each sample contains several channel quality indicators, such as RSRP, for all the detected PCIs and beams. We create a coverage map by walking around the site with the scanner, and perform stationary measurements at selected locations, each lasting typically at least 5 minutes, to capture the time variations of the signal strength. Figure 4.2 shows the scanner and some of the measurement scenarios.

We also collected the measurements to analyze the performance of 5G mmWave end-to-end transmission. Because of BS maintenance, the northern sector was not operational, and the measurements for the bitrate and delay study were done only in the southern sector. Each experiment was repeated at exactly the same locations and with the same BS configuration used for the channel quality measurements. This experiment focused on the user experience, so we evaluated the end-to-end bitrate and Round Trip Time (RTT). The measurements were performed with a pre-production Huawei 5G CPE, supporting 2×2 MIMO and operating in Non-Standalone (NSA) mode, which can reach data rates of up to 1 Gbps. A Gigabit Ethernet cable connects the CPE to a laptop which acts as the client. Even though the BS can achieve approximately 3 Gbps in downlink, the Gigabit Ethernet limits the maximum transfer rate with the laptop to 1 Gbps. This does not pose an obstacle for our analysis, since we are more interested on the cases where the network performance drops well below this limit, as a consequence of obstacles or other environmental phenomena. Figure 4.3 shows the devices and the measurement setup used for this study.

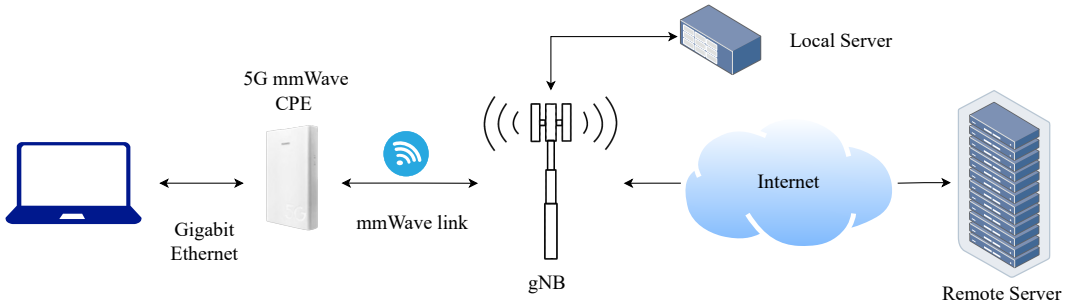

Figure 4.3: The measurement setup for the end-to-end communication experiment. The CPE is connected through a Gigabit Ethernet cable to a laptop running the scripts.

The traffic sources are servers located inside the operator's network to avoid the effect of cross-traffic and congestion over the public Internet. The delay performance was assessed from the RTT measurements given by `ping`, with packets of 64 bytes (default setting) and of 1500 bytes (maximum size allowed by the Ethernet connection without requiring IP fragmentation). Note that, to be transmitted over the wireless link, the bigger `ping` packets have to be split into multiple Transport Blocks when the system experiences bad signal, which results in the use of robust (but not very spectrum efficient) modulation and coding schemes. The bitrate performance is evaluated through `iPerf3`*, a cross-platform tool for network performance measurement. We use ten parallel TCP connections, lasting at least 10 seconds, to get an estimation of the bitrate achieved at each measurement location.

4.4 Measurement Results

4.4.1 Coverage analysis

We first focus our analysis on the measured Synchronization Signal Reference Signal Received Power (SS-RSRP), which is the average power of the Resource Elements (REs) that carry the Secondary Synchronization Signal (SSS) transmitted within a Synchronization Signal (SS) (SSB) [159]. The beams are time-multiplexed, thus there is no interference between the beams when the SS-RSRP is measured. For simplicity in the sequel we will refer to SS-RSRP as RSRP. Each SSB / beam is assigned a unique number, called SSB index. Note that the values of the SSB index were not contiguous. Thus, in the subsequent plots, the numbering of SSB indexes has gaps.

Figure 4.1 presents the mmWave coverage map. At each location, we were able to detect all the PCIs of the relevant sector and most of the beams. Since a UE would be attached to the dominant beam, i.e., that with the highest RSRP among those detected by the UE, in Figure 4.1 we report only this maximum RSRP values.

In mmWave bands, the RSRP is dominated by the signal's LoS components: missing these components can lead to significant attenuation. This can be easily seen in area **A** of Figure 4.1, where

*https://iperf.fr/

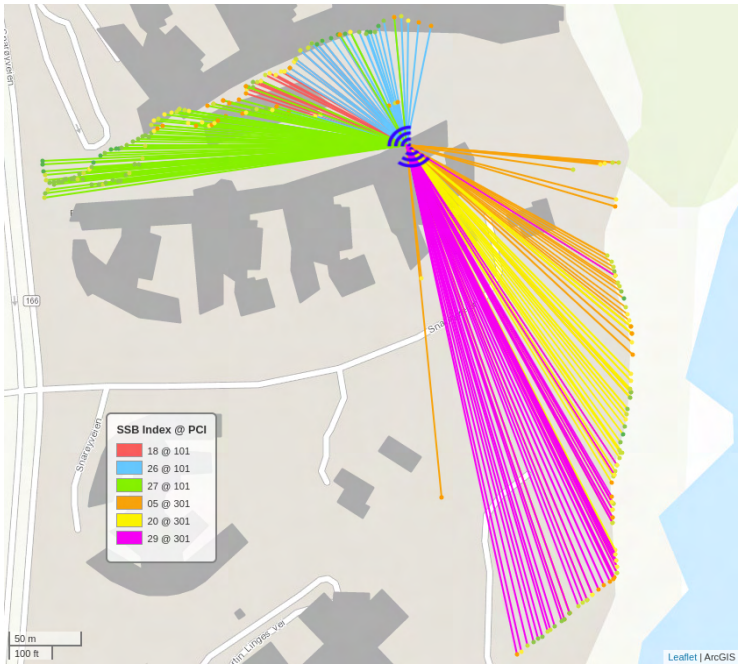

Figure 4.4: Dominant beams (lines) and the related RSRP values (points) in a subset of the locations.

the LoS link is blocked by buildings and the RSRP drops below -113 dBm. Although the availability of LoS components of a mmWave signal is an important factor in determining coverage, other effects like signal diffraction, reflections from surrounded objects, and multipath propagation can compensate for their absence. These effects are likely responsible for the relatively large RSRP measured in Area **C** of sector 1, between the two buildings, where the LoS link is blocked by the roof edge of the building hosting the BS. In contrast, in absence of reflecting or diffracting elements, there are no NLoS components of mmWave signals. This is the case of area **A**, where the signal propagates in a vegetated area without many reflecting elements, and of area **D**, where we did not record any significant RSRP value at most of the locations.

As expected, we did not observe a significant difference between PCIs for the same beam. Moreover, in presence of LoS, we did not record a strong dependency between signal power and distance to the BS. The attenuation due to the increasing distance is indeed marginal compared to the rest of the factors that affect the RSRP, which fluctuates within a certain range as long as the receiver remains in the main lobe of the dominant beam. This behavior can be observed by considering a straight LoS line in Area **B** and sampling locations at a distance from the BS ranging from 200 m to 450 m. At such LoS locations, the median RSRP value of the dominant beam is always between -94 dBm and -100 dBm, regardless of the distance. We hypothesize that it is the vertical antenna gain pattern that is causing this behavior. At short distances we were located significantly below the boresight of the BS antenna, hence the antenna gain was low. As we moved further away we got closer to the boresight and the antenna gain increased. So the effects of larger pathloss and increasing antenna gain as the distance increased approximately cancelled

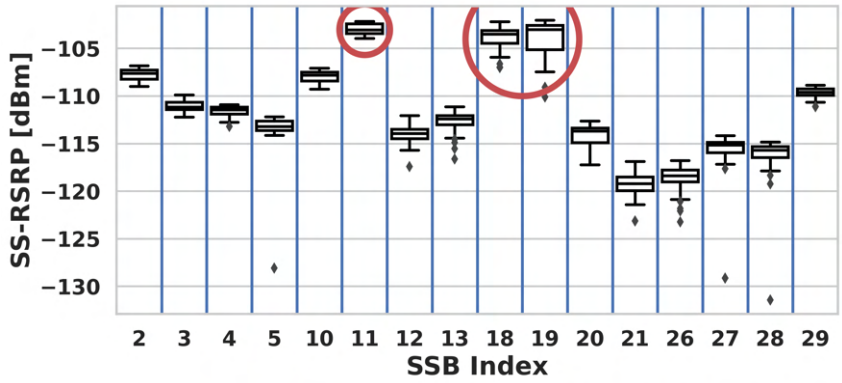

Figure 4.5: On rare occasions, we observe multiple dominant beams. Static measurements over a 5-minute period at a location 250 m away from the BS, where several beams could be considered dominant (highlighted with red circles).

each other. We discuss in more detail the relationship between RSRP and distance in Section 4.5, where Fig. 4.11b visualises our measurements and compares the maximum measured RSRP to state of the art models.

To construct the bitrate map, we launched 10 parallel continuous TCP connections and walked around the cell site with normal speed, while tracking the location by external GPS. Simultaneously, `tcpdump` captured the generated traffic. We were able to get an estimate of the observed bitrate at each location by correlating the timestamps of the packet capture and the GPS log. The packet capture is split into 100 ms bins and all the packets received during a bin are grouped together. The bandwidth values are estimated by dividing the total number of bytes of all the packets in a bin by 100 ms. Then, we assign this bandwidth value to the closest, by time, GPS entry. As shown in Figure 4.1, the bitrate in different locations is highly correlated with the RSRP: the higher the RSRP, the higher the bitrate. As seen in the figure, in the LoS locations, the maximum possible bitrate is achieved. Even in area **E**, which is relatively far from the BS, the bitrate is high. Note that, the Gigabit Ethernet connecting the CPE to the Laptop is the bottleneck and limits the network speed to 1 Gbps. In a very bad channel state (area **D**), TCP still keeps the connection open but with a very low bitrate.

4.4.2 Beam separation

A sharper beam can improve spatial separation between users, hence increasing MU-MIMO performance, as well as reduce interference in multi-cell deployments. To showcase beam separation, we select a few locations, creating a perimeter at the ground level around the BS. Figure 4.4 color codes the dominant beam at each location. The beam lines drawn on the map are hypothetical, connecting the BS and receiver location and the actual beams are not as narrow as we have shown in the figure: signals from different beams can be detected at a much wider angle (side lobes) and even at the backside of the transmitter (back lobes). According to [160], the RSRP should be above -110 dBm to be detectable by 5G NR UEs, thus we filter out values below this threshold. For each

Table 4.2: Summary of the body blockage effect on bitrate.

Position	Bitrate [Mbps]
Line of sight	822
No line of sight (2 sitting 2 meters away from the CPE)	613
No line of sight (2 standing right in front of the CPE)	755

sector, we have also displayed only three out of 16 beams and have not considered the beams that overlap in the vertical plane. We observe a similar beam separation pattern across the vertical axis, by performing measurements on several floors at the building opposite of the BS at sector 1. The dominant beams at the ground level, third floor, fourth floor and roof are different.

As commented in Section 4.4.1, within a certain range, the actual distance between transmitter and receiver is not of much relevance as long as the receiver is within the main lobe of the dominant beam. Therefore, it is possible to get good signal even at long distances. The furthest point from the BS we could detect RSRP higher than -110 dBm was 902 meters. We can assume a commercial UE would be able to achieve an even bigger range, because of the receiver antenna gain. At almost all the studied locations, a single beam had consistently and markedly higher RSRP than the rest for the whole measurement duration, so beam selection was trivial. However, it is possible to have multiple dominant beams in some locations, as shown in Figure 4.5, where the RSRP values for different beams are presented at a single location for one PCI over a 5 minute period. We can observe that three beams, marked with red circles, have about the same median value. The number of simultaneous beams is limited by the number of Transmit/Receive (transceiver) units in the BS, so only one beam is transmitted in any given time/frequency slot for each PCI. This time multiplexing avoids inter-beam interference, but beam selection becomes more complicated. In such cases, it might be better to have a secondary criterion for beam selection, such as choosing the beam with the lowest standard deviation of RSRP. Even more sophisticated beam selection algorithms [161], [162] might be required in a more complicated and dynamic propagation environment. On the other hand, the slightly overlapped coverage regions of the SSB beams are good for robustness (body blockage, moving cars, etc), where there is a higher chance of having at least a good beam at any time. The other benefit of this slight overlap (or closely spaced beams) is to have a smooth user experience as a UE moves from one beam's coverage region to another beam's.

4.4.3 Environmental impact on mmWave propagation

In the following, we analyze the effect of different environmental factors such as human body blockage, communication over-water surfaces, foliage and rain-induced attenuation on mmWave propagation.

Human body blockage effects To analyze the impact of human body blockage, we placed the scanner at a LoS location 260 meters away from the BS. We then blocked the direct link from the BS in two different ways. First, by standing 10 cm away from the scanner, and later by folding

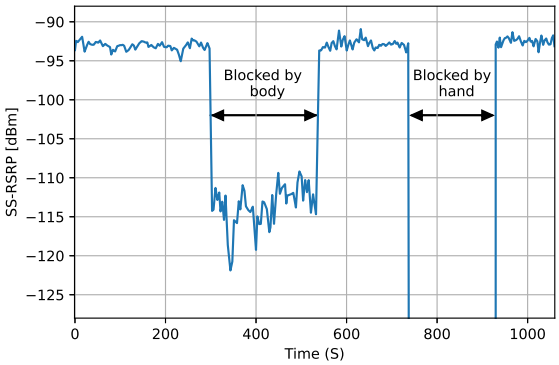

Figure 4.6: Body blockage effect on mmWave propagation at a location 260 m away from the BS with a LoS link.

Table 4.3: Summary of the effect of different types of foliage to bitrate and delay.

Position	Bitrate [Mbps]	RTT [ms]	RTT big [ms]
LoS baseline besides the trees	891	14.6	15.7
Besides a small tree	831	13.4	16.6
Behind a single branch	785	14.8	17.5
Behind big tree with sparse leaves	451	14.8	19.6
Behind big tree	323	15	17.8

the hand around the scanner's antenna, which are typical behaviors of smartphone users. As shown in Figure 4.6, we observed a 20-30 dB drop in RSRP in the first experiment, which is in line with the literature [143]. In the latter case, all the signal components were removed, and we were unable to detect any signal. In the first case, the received signal was likely due to the NLoS components reflected or scattered from the surrounding objects, or diffracted from the person were standing in front of the scanner. Folding the hands around the scanner's antenna, instead, completely shielded the receiver from all the signal components, which explains the absence of significant RSRP measurements. The human body blockage effects on mmWave communications have already been investigated and modeled in various ways, and the interested readers can refer to [142], [163] for more information. Our experiments hence confirm this critical aspect also in commercial cell deployments.

The effect of body blockage on bitrate is presented in Table 4.2. We measured the bitrate with 10-parallel TCP connections as above, while 1) two average-size people were sitting about 2 meters away from the CPE, completely covering the LoS link, and 2) two people standing right in front of the CPE. As seen in the table, the bitrate dropped from 822 Mbps to about 613 Mbps and 755 Mbps for the first and second scenarios, respectively. This shows that despite the partial occlusion of LoS, the performance at TCP layer seems to remain acceptable.

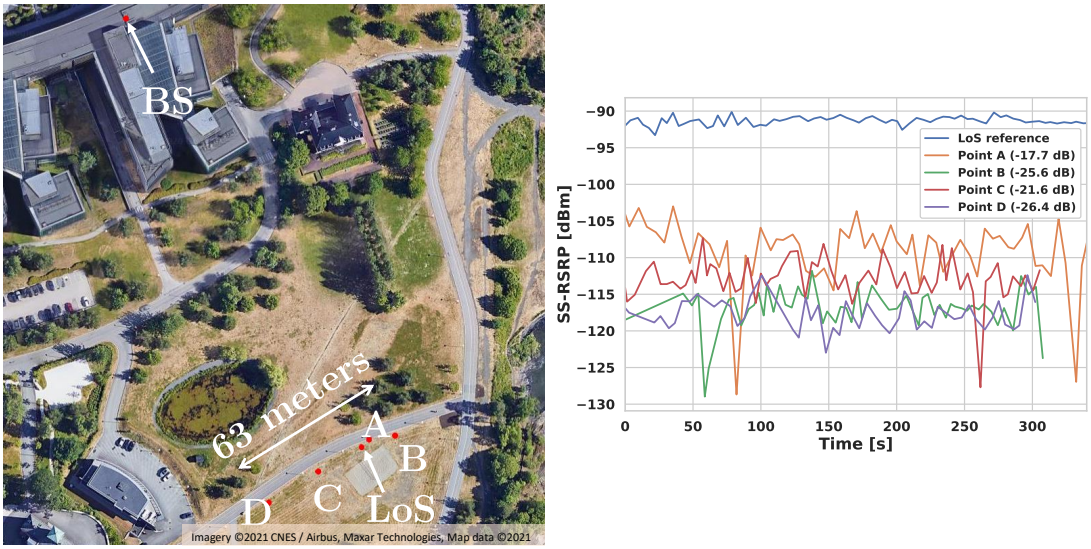

Figure 4.7: Foliage attenuation scenarios compared to LoS. Locations A, B, C and D suffer from different types of foliage blockage. Distance from BS: ≈220 m for all locations.

Foliage Attenuation The propagation characteristics of mmWave frequencies in suburban and vegetated environments are very different from those in urban and indoor scenarios. Foliage attenuation could significantly affect communication over this frequency range and should be considered in network planning for such suburban areas [139]. We carried out a set of measurements to investigate the effect of blocking the path between transmitter and receiver by vegetation and trees. During the measurements, nearby weather stations reported wind intensity between 4.7 and 5.9 m/s, which is considered a "gentle breeze" according to the Beaufort scale. The leaves and the twigs on small trees were in constant motion.

Figure 4.7 shows the RSRP at 4 different locations where the LoS path is blocked by different types of trees. The recorded RSRP exhibits significant attenuation at all four locations, typically 15 dB to 30 dB lower than our measurements at a nearby reference LoS location. The intensity of attenuation highly depends on the type and shape of the blocking trees, with bigger trees causing higher attenuation. As Figure 4.7 illustrates, the smaller trees at location **A** attenuate the signal by 17.7 dB, while the bigger ones at location **D** decrease the received signal power by up to 26.4 dB. This result is comparable with similar studies, where the authors reported 22.48 ± 0.92 dB foliage attenuation in 26.5 GHz [164]. The high variations in RSRP are likely due to wind that constantly moved trees' branches and leaves, which resulted in varying blockage and reflection patterns.

Table 4.3 summarizes the result for the foliage effect on bitrate and delay. The measurements take place under a gentle breeze (wind speed between 2.4 to 5.1 m/s). As was expected, the bitrate drop and delay are highly correlated with the result from the RSRP measurement. The bigger trees with more dense branches and leaves cause a more significant drop in RSRP, and these unreliable links result in decreasing the bitrate and increasing the RTT. Based on the type of foliage and tree, communication speed dropped from 891 Mpbs at the LoS baseline location to

Table 4.4: Water effect on mmWave propagation, across all the southern sector's PCIs. Instances with high std are highlighted.

Beam type	Distance (m)	PCI-301		PCI-302		PCI-303		PCI-304		TCP		
		mean [dBm]	std	mean [dBm]	std	mean [dBm]	std	mean [dBm]	std	Bitrate [Mbps]	RTT [ms]	RTT big [ms]
Over water (close to the sea level)	792	-103.2	**2.33**	-105.2	**3.12**	-103.7	**2.62**	-105.9	**3.35**	903	13.9	17.5
Over water (6m above sea level)	813	-111.4	**4.61**	-110.6	**4.70**	-107.7	**3.16**	-105.8	**3.25**	885	15.5	16.6
Ground	573	-94.3	0.29	-94.7	0.33	-93.0	0.30	-92.3	0.29			
Ground	256	-103.0	0.54	-102.1	1.21	-100.1	0.66	-100.7	0.76			
Ground	213	-91.3	0.56	-94.2	0.76	-96.4	0.84	-92.2	0.59			
Ground	323	-93.1	0.80	-94.8	1.57	-103.7	**3.20**	-97.5	1.87			

426 Mbps when being behind small trees and further dropped to 323 Mbps when being behind big trees. Also, the delay is larger for big packets than for small packets, as they may break into multiple Transmission Blocks and be retransmitted multiple times under challenging signal conditions.

Rain-caused attenuation We collected measurements on two different days, with dry and rainy weather, at the same location. During the rainy day, nearby weather stations reported precipitation between 0.1 and 0.2 mm per minute, which is a moderate to heavy rain intensity. Figure 4.8 presents the RSRP values measured for different weather conditions for a single PCI, grouped per beam. Results for the other PCIs are similar. As it can be seen from the figure, rain causes a notable drop in the mean RSRP and increases its variability in particular for the weaker beams.

The increased variability for the weaker beams is probably caused by multi-path signal propagation where no single signal component is significantly stronger than all others. The most significant components will consist of signals reflected by e.g. buildings and vegetation, and usually also of the LoS signal. Strong beams point towards the scanner and the BS antenna gain for the LoS signal will be high. Therefore the LoS signal will be much stronger than the reflected signals, and the received signal power will have little variability. Weak beams, on the other hand, do not point directly towards the scanner and the BS antenna gain for the LoS signal is therefore low. In this case the strength of the reflected beams might be comparable to or larger than the strength of the LoS component. This results in multi-path fading that gives large variability in the received signal power.

Over-water communication We also investigate how water surface scattering and reflection affect mmWave signals. This scenario could be relevant when mmWaves are used for providing high capacity communications on the shore. For example, fish farms plan to use mmWaves for high definition video communications between fish cages and on-land data centers where advanced signal processing and analytics are used to, e.g., control feeding and monitor fish health [130].

We performed the measurements at locations with good LoS of the BS antenna, on the far side of a small bay. From the BS, the mmWave signal first travels over the ground for about 630 meters and then over-water for 160 meters before reaching the scanner. The measurements were collected at two locations. First, we put the scanner at the shoreline about 50 cm from the wa-

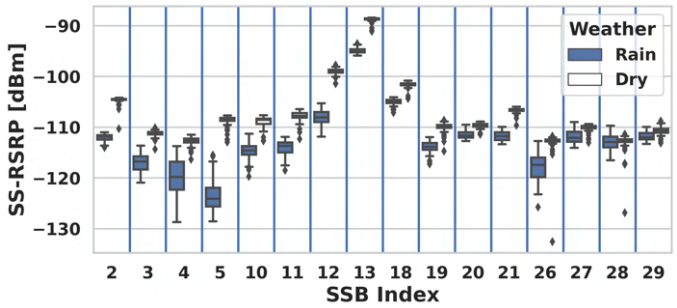

Figure 4.8: Comparison of received power during rain (left element per boxplot pair) and dry (right element per boxplot pair) weather for a single PCI. Distance from BS: 214 meters.

ter. Second, we placed the scanner approximately 6 meters above the water surface. We could not assess the water wave height directly, but during the measurements, nearby weather stations reported a wind intensity between 4.9 m/s and 5.6 m/s, which typically corresponds to wave heights of 0.6 m to 1.2 m. The measurement location is relatively sheltered, though, so we can assume that the wave height is closer to the lower limit of this range. For comparison, we also made corresponding measurements at LoS locations with different distances to the BS where the propagation was solely over-ground (due to terrain and building blockage, we were not able to do over-ground propagation measurements at exactly the same distances as for the over-water measures). Table 4.4 summarizes our measurements. The RSRP standard deviation for over-water propagation is significantly larger than for over-ground propagation. The increased standard deviation for the over-water communications can be explained by a model where the received signal consists of a direct LoS component and one or more components (specularly or diffusely) scattered from the water surface. Since the water surface moves, the scattered components' strength varies with time, thereby causing signal power variations at the receiver.

Another observation from Table 4.4 is that the difference between the mean RSRP values for PCIs with different frequencies are much larger at 6 meters above the water than at the sea level. This can be explained by the same propagation model. When the scanner is located close to the water surface, the scattered components of the signal are coming from the water immediately in front of the scanner. In contrast, these components are originated much further out when the scanner is placed far above sea level, so the scattered components' delay compared to the LoS is more variable. In frequency domain, this translates to flatter fading (i.e., attenuation is almost the same across neighboring frequencies) when the scanner is at sea level than when placed at a higher location. A consequence of the increased signal variation for over-water reception is that it will be necessary to use a higher link margin in the link budget calculations than when the communication is solely over-ground. The smaller signal variation for the scanner located at sea level suggests that mmWave antennas should be placed close to the water, e.g., on a fish cage.

Table 4.4 also presents the bitrate and RSRP values for the over-water transmission. The bitrate and the delay at 6 meters above the water are significantly worse than at sea level. This observation was also expected, as the high-level performance is indeed correlated with the RSRP

values.

nLoS measurement scenarios In mmWave communications, LoS links can be easily blocked by buildings, moving cars and other obstacles. In this case, the RSRP depends on the NLoS components, such as reflected, scattered and diffracted waves. To get an indication of the NLoS coverage we performed measurements at four locations where the LoS path to the BS antenna was blocked by the roof of the building with the BS (See Figure 4.9). Locations **S1** and **S2** in Figure 4.9 are surrounded by high buildings and a large number of rectangular columns placed in a regular pattern in the plaza between the buildings, representing an urban environment. Locations **S3** and **S4** are surrounded by trees and some distant buildings, representing a suburban and vegetated environment. Figure 4.10 presents the RSRP distribution of the best beam (written in parenthesis) for every carrier (PCI) of the BS at these locations. Even though the orientation of the beams is the same for all the PCIs at the BS, we observe that at locations **S2** and **S4** the dominant beam is different for some of the PCIs. Further, at location **S2**, PCI 101 has degraded performance compared to the rest of the PCIs. Both observations are in contrast to what we measure at LoS locations. It can be due to the property of different scattering and diffracting materials at different frequencies (i.e., reflection coefficients and penetration losses), but we are unsure about the exact source of these behaviors.

At locations **S1** and **S2** the received signal is quite strong, indicating good NLoS coverage. This is thought to be due to the rich scattering environment, possible reception of diffracted (i.e., from the edge of the roof) signal components and the relatively short distances involved. At locations **S3** and **S4** the received signal level is very low and there is little or no NLoS coverage. This is thought to be due to a much poorer scattering environment. The buildings that might act as good reflectors for the signals are located far away from both the BS antenna and the scanner, hence the signal paths will be very long. The trees in the surrounding area further attenuate both the reflected and the diffracted signal components. These results show that in an urban environment, with multiple buildings and scattering elements, the NLoS components of the mmWave signals could compensate for the lack of a LoS link to the BS. In contrast, in vegetated areas, the LoS link is necessary to establish reliable communication.

Finally, we study the end-to-end communication performance over NLoS 5G mmWave links. To do so, we collect measurements in different locations, close to the buildings, where there is no LoS path to the BS. These locations are marked as **P1-P5** in Figure 4.9. Table 4.5 reports the bitrate and RTT values for the mentioned locations. It is evident that the bitrate sharply drops and the delay increases by moving toward the buildings. This is an expected observation as fewer diffracted elements reach the locations close to the building, which results in lower RSRP and therefore bitrate.

4.5 Comparison with Simulations

This section compares our measurement results with simulations based on empirical models to check how accurately statistical models can predict the received signal at different locations. The

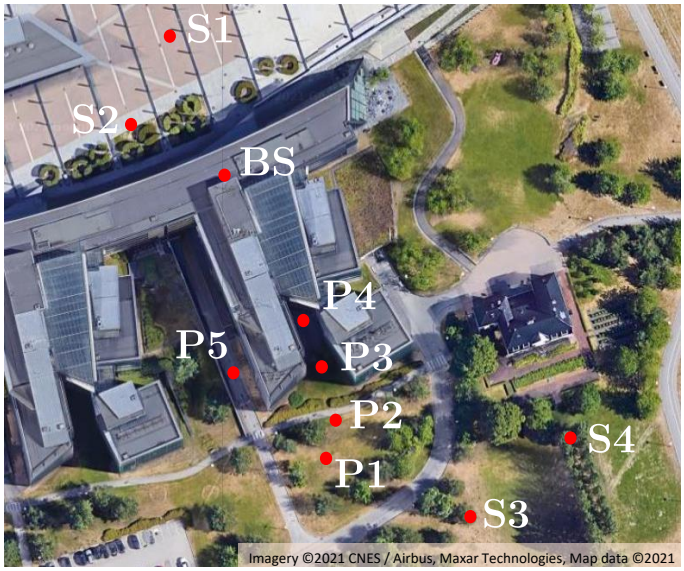

Figure 4.9: The locations where the nLoS measurements were performed.

Table 4.5: Summary of the effect of nLoS links to Bitrate and delay.

Position	Bitrate [Mbps]	RTT [ms] normal size	RTT [ms] big size
P1	845	15.4	17.8
P2	573	16.5	33.9
P3	176	15.6	22.1
P4	87	18.0	48.0
P5	177	15.4	18.1

complexity of the propagation environment, makes impossible the use of accurate channel models, i.e., ray-tracing based quasi-deterministic channel models [165], [166], to accurately obtain the NLoS components of the propagated signal is not possible. We hence used 3GPP's statistical channel model for mmWave frequencies [167] to estimate the path loss for different scenarios. For Sector 1, we use the Urban Micro (UMi) and Urban Macro (UMa) channel models [168], [169], as the BS is pointed towards a square surrounded by large buildings and the topology is similar to a typical urban environment, while for Sector 2, we employ the Rural Macro (RMa) model [170], as it represents a suburban area with more trees and vegetation and fewer or no buildings. The omnidirectional path loss model used in our simulations is:

$$\mathrm{PL[dBm](d)} = 20\log_{10}(\frac{4\pi \mathrm{d_0}}{\lambda}) + 10\mathrm{n}\log_{10}(\frac{\mathrm{d}}{\mathrm{d_0}}) + \mathrm{SF}, \tag{4.1}$$

where, d is the distance from transmitter, $\lambda = \mathrm{c}/(10^9\mathrm{f})$ [m] is the wavelength, $\mathrm{c} = 3 \times 10^8$ [m/s] is the speed of the light, SF [dB] indicates the shadow fading, whose standard deviation is σ_{SF}, n represents the path loss exponent and $\mathrm{d_0} = 1$ [m] is the free space reference distance. The values for σ_{SF} and n at different scenarios are presented in Table 4.6.

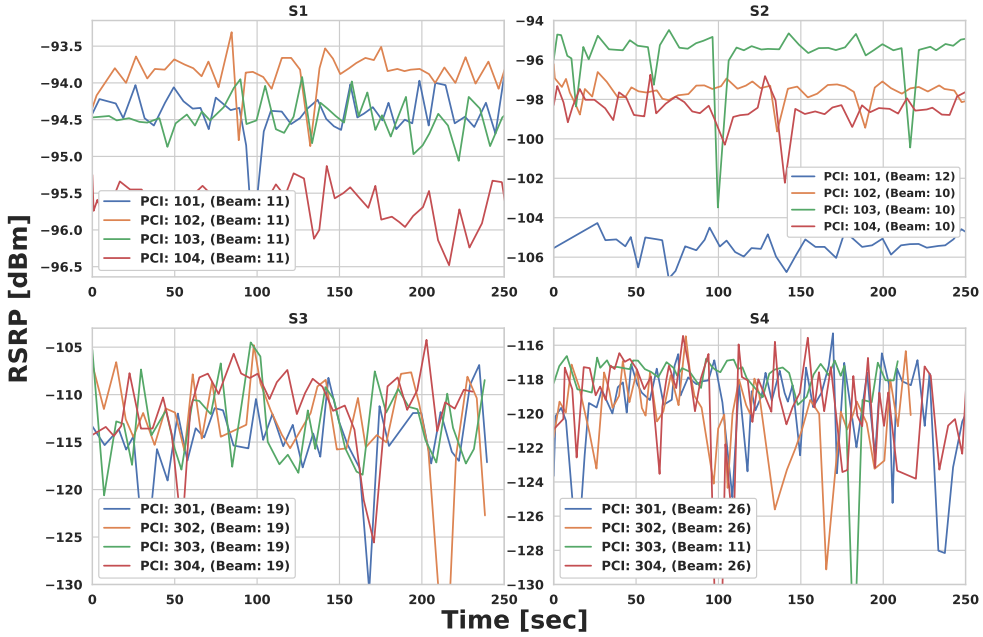

Figure 4.10: RSRP in different locations with NLoS links to the BS.

Table 4.6: Simulation parameters.

Parameter	RMa		UMa		UMi	
	LoS	nLoS	LoS	nLoS	LoS	nLoS
n	2.3	3.1	2	2.9	2	3.2
σ_{SF}	1.7	6.7	4.0	7.0	4.0	7.0

Figure 4.11 shows the maximum measured RSRP of the dominant beam at different distances for Sector 1 and Sector 2 and compares it to the RSRP achieved using the omnidirectional path-loss model in (4.1), as is perceived from two omnidirectional isotropic transmit and receive antennas with 0 dBi gain.

The strongest measured RSRP in Sector 1 is ≈-78 dBm, which is a bit higher than the strongest RSRP in the other sector (≈-84 dBm). As shown in Figure 4.11a, our measurements can barely fit with the 3GPP UMi and UMa models. The RSRP varies between -78 dBm and and -130 dBm which is always lower than the predicted values by the LoS models and only at larger distance is lower than the NLoS models. This figure clearly shows that statistical channel models are not always capable of predicting the RSRP accurately in every propagation environment. Figure 4.11b shows that the LoS RMa can estimate the RSRP in locations with clear sight to BS. Even in Area **E**, where the signal propagates overwater, this model predicts the RSRP relatively well ($\leq$ 5 dBm error). On the other hand, NLoS RMa fails to accurately predict the RSRP for NLoS locations.

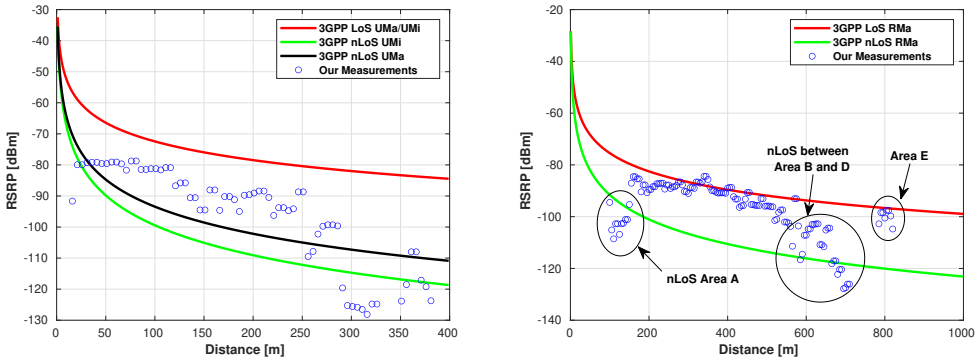

(a) Sector 1 **(b)** Sector 2

Figure 4.11: Comparing the maximum measured RSRP with simulated 3GPP models for different distances in (a) Sector 1, and (b) Sector 2.

The variation in measured power in NLoS is mainly due to changes in the type of the obstacles, scattering objects, and topography of the environment, rather than pure distance. Referring to Figure 4.1 and Figure 4.9, the type and shape of obstacles blocking LoS in area **A** and the area between **B** and **D** are very different and composed of buildings with various shape that highly affect the RSRP in these areas.

Table 4.7 compares the RSRP recorded during the measurement campaign against the 3GPP channel models which are used to estimate the RSRP, both on case of omnidirectional and directional antenna gain patterns at transmitter and receiver. To obtain the values for the strongest RSRP, we use the NYUSIM simulator [171], which searches for the best pointing angle among all possible pointing angles employing the specified antenna details (i.e., azimuth and elevations of receiver and transmitter antennas) in both transmitter and receiver. The details of the procedure is out of the scope of the this chapter and interested readers may refer to [171], [172] and the references therein for more details. For this simulation, we assumed that BS and UE are equipped with 16 and 4 uniform linear array antenna elements, respectively.

As seen in Table 4.7 and Figure 4.11, only in limited LoS scenarios, the omnidirectional path loss models perform well in predicting the mmWave channels. In complicated environments, especially in NLoS locations with many complex scattering objects, using more advanced ray-tracing-based models is difficult, if not impossible, so some extent of measurement is needed to estimate the RSRP accurately. It is also seen that in the best case, the received power at different locations is as good as the omnidirectional power. The gap between the measurement (and omnidirectional power) with the Strongest power is significant for all scenarios ($\approx$ 50 dBm). This vast gap reveals how much an adaptive dynamic beamformer can improve performance. This specifically makes more sense in some mmWave use-cases where the UEs are stationary, i.e., Fixed Wireless Access (FWA) or do not move fast. Some codebook-based beamforming techniques can be employed for these use-cases where the optimal transmitter / receivers antenna configuration can be learned and saved for future uses.

Table 4.7: Comparing the measured RSRP [dBm] with simulations for different scenarios.

Scenario	Distance [m]	Measurement	Simulation	
			Omni	Strongest
RMa LoS	160	-84.5	-80.8	-31.5
RMa LoS	250	-87.7	-85.2	-36.0
RMa LoS	350	-85.6	-88.8	-39.6
RMa LoS	450	-90.6	-91.4	-42.2
RMa LoS	570	-93.0	-94.0	-44.8
RMa LoS	810	-97.5	-97.7	-48.4
RMa nLoS	80	-103.9	-90.4	-41.2
RMa nLoS	120	-102.7	-93.4	-44.2
RMa nLoS	590	-114.4	-117.6	-68.4
RMa nLoS	690	-120.3	-117.5	-68.3
UMa LoS	60	-79.0	-64.5	-17.2
UMa LoS	160	-88.0	-73.4	-26.1
UMa LoS	250	-88.6	-77.0	-29.6
UMa LoS	500	-97.8	-83.2	-35.9
UMa nLoS	15	-91.6	-63.7	-16.6
UMa nLoS	300	-114.3	-100.5	-53.4
UMa nLoS	450	-123.6	-106.0	-58.8

4.6 Summary of Results and Discussion

This section summarizes and discusses the results of our measurement campaigns to provide an overview and guidance for different verticals considering 5G mmWave networks for various communication solutions.

Based on our measurement results, we can confirm that the range of mmWave cells is strongly affected by obstacles, such as buildings, trees, or human bodies, as already observed in the literature. As expected, the LoS beam is generally the most robust in all situations. These observations are against employing 5G mmWave in NLoS and dynamic environments, where the LoS line is constantly blocked; at least with current TCP protocols and for time-critical applications. Some examples of these use cases are large industrial environments, where LoS links get blocked by hefty mobile machinery, and cell phones, where the antennas can easily be covered and blocked by the user's hands, head, and body. For these cases, combining 5G mmWave with multi-path TCP [148] or TCP proxy architecture [173] can provide more reliable solutions. One interesting use case for 5G mmWave networks that network operators have recently considered is FWA, which aims to provide high-speed internet for houses, especially in rural environments. Internet providers can highly benefit from this solution, as it can decrease costs by replacing the expensive optical fibers with 5G mmWave links.

The solutions concern different environmental impacts, from rain to foliage, on communications over mmWave links; in general, these phenomena can highly degrade the received signal and hence service quality. Regarding the effect of foliage, we observed signal quality drops when the LoS is obstructed by trees, particularly when moved by (even light) wind. However, this

generally affects all beams so that the dominant beam remains the same. Therefore, the beam tracking solutions that have been widely analyzed in the literature may turn out to be ineffective in these scenarios. The measurements have also revealed that wide water surfaces, especially in the presence of waves, can generate time-varying scattering phenomena that affect the stability of the received signal. This is pronounced if the receiver is higher than the water surface and thus collects more water-reflected waves. The propagation of mmWave on water surfaces is, hence, critical and would require further investigation to determine the limitations of links involving floating stations.

The take-out message for the network planners that are deploying 5G mmWave solutions for applications like forest surveillance and monitoring system, fish monitoring systems, ship-hull inspection systems, and anti-grounding service [174], which involve communications in forest areas, fish-farms, and harbors, is that deploying such a system based on 5G mmWaves needs careful design, as ignoring some environmental factors, like rain or wind, can lead the system to fail. Comparing the measured RSRP with the simulated omnidirectional (based on 3GPP's path loss models) and strongest RSRP (optimal antenna configuration) shows the necessity of measurement in especially complex NLoS environment, in predicting cell coverage and recognizing coverage holes. It also reveals the considerable improvement that mmWaves can achieve by employing a perfect beamformer, as by utilizing the beamforming gain, network operators can highly increase the power and the service rate for final users.

4.7 Conclusions

Our empirical analysis of a commercial 5G cellular system has confirmed the validity of previous studies carried out on prototypal or PoC deployments or via simulations. Clearly, general theoretical models cannot perfectly capture the complexity of real installments, and some significant deviations from model predictions and real-world measurements have been observed in certain cases. This will require the implementation of self-tuning capabilities on commercial installations to adapt the BS configuration to the specificities of the environments, though a first, rough performance estimate can be done using the theoretical models. The effects of body blockage, rain, and trees on the propagation of mmWave signals previously reported in the literature have been mostly observed also in our study. This confirms that the commercial version of the mmWave communication interface does not show any significant limitation with respect to pre-commercial versions, which was not guaranteed. On the other hand, it does not bring any improvement either. Finally, we noticed that beam selection in a real commercial setting is likely less critical than feared, since the strongest beam appears to remain rather stable in time and space, also in bad weather conditions, so that beam swiping techniques should be able to track the best beam direction rather easily.

The above observations should help interested stakeholders make more informed decisions when deploying 5G solutions utilizing the mmWave spectrum. Our next steps involve testing verticals' use cases at the same cell site to check if their service requirements are met.

For future works, we will extend the result for the end-to-end transmission study, investigating

the performance of TCP variants over unreliable mmWave links in various scenarios. We will also investigate the performance of delay-sensitive applications such as live broadcasting (i.e. a special case of online video streaming) and networked music over 5G networks. Finally, some of the mentioned scenarios can be repeated over operational networks in different customer sites like fish farms, factories, etc.

5

Energy-Efficient Design for RIS-assisted UAV Communications

5.1 Introduction

Increasing demand for sustainable and flexible connectivity specifically for either semi-urban or rural areas [13], [175] or disaster scenarios for monitoring and surveillance [176], [177], has led to focus on the usage of Unmanned Aerial Vehicles (UAVs) and Reconfigurable Intelligent Surface (RIS) for enhancing the network coverage and, thereby, the service availability of cellular networks. The conceptual design of RIS consists of several reflective elements which can be configured so as to reflect and, in particular, beamform a signal towards a particular direction. Recently, there have been certain works that have provided definitions and optimization scenarios to tackle the direct links between UAVs and User Equipments (UEs) as well as links between UAV and UE with the aid of RIS [178]–[181]. However, the issues of the existence and capacity limitation of the link from Base Stations (BSs) to UAVs have not been considered so far in conjunction with the issue of optimizing the UAV movement and RIS configuration. This should not be overlooked as the performance of the system clearly depends on the whole path from BS to the UEs. Indeed, UAVs and RIS can be used to create mobile micro cells to serve temporary hotspots, i.e., areas with very high service requirement at a certain time. Additionally, the joint usage of UAVs and RIS can also enable to learn and adapt the network based on information such as user mobility and density to satisfy the user service requirements [182]–[184]. Additionally, the availability of high frequency communication technologies, such as mmWave [185], to satisfy the higher bandwidth requirements in beyond 5G networks has increased the interest on exploiting the unconstrained mobility of UAVs to provide dynamic coverage where and when needed. Also, the enhanced beamforming capabilities of RIS can be exploited to increase the coverage

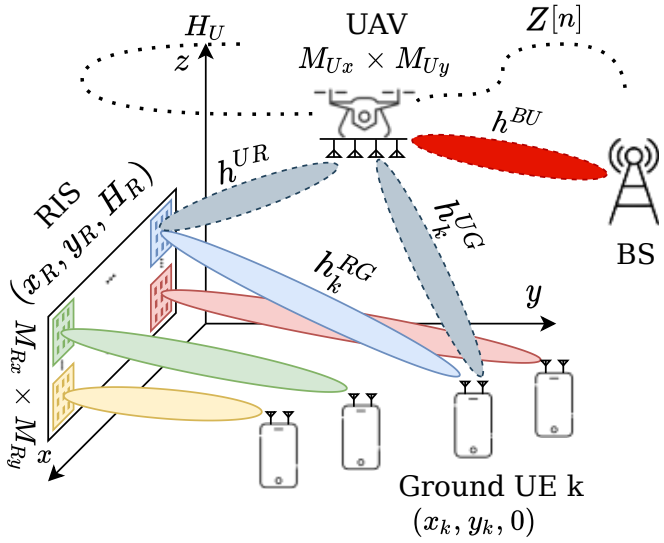

Figure 5.1: The problem scenario.

for mmWave networks [186]. These new technologies have individually provided significant improvement in terms of service availability in semi-urban / rural areas or disaster scenarios, while potentially reducing the energy consumption of the system [187]. But the usage of high frequency technologies in conjunction with both UAV and RIS raises new challenges in terms of network optimization. In particular, a significant issue regards the trade-off between communication range and quality of service in a dense urban scenario.

One of the major hurdles while using both these technologies is the energy consumption of the system as a whole. UAVs, especially quadcopters, generally run on small batteries and the energy consumption is very high when the UAV is in flight. Therefore, to provide sustained coverage to the UEs with high Quality of Service (QoS) requirements, the trajectory of the UAV has to be optimized. The use of RIS, which can improve the coverage in certain areas, may help reducing the need for UAVs to travel further, with a small trade-off on the energy consumed for RIS operation [79], [178], [188]. As the energy consumption in RIS is still a research problem, we need to parametrize it by assuming E^{RIS} joules per unit for reconfiguration, with the goal of finding how small the energy should be in order to obtain an overall net benefit.

To summarize, in this chapter we explore the possibility of the combined usage of UAVs and RISs to reduce the energy consumption of the entire system, while providing a certain level of QoS to the UEs in the area. Figure 5.1 denotes the overall scenario in question. The UAV acts as a mobile BS relay that can establish Line-of-Sight (LoS) links with the UEs and the RIS, something that might not be always possible for the fixed BS. The UAV hence extends the area of coverage of the BS, while optimizing the energy consumption for in-flight movement and signal transmission due to the inclusion of the RIS. If the RIS position is optimal, which is another open research problem, the UEs can be served either directly by the UAV or with the help of the RIS or there-

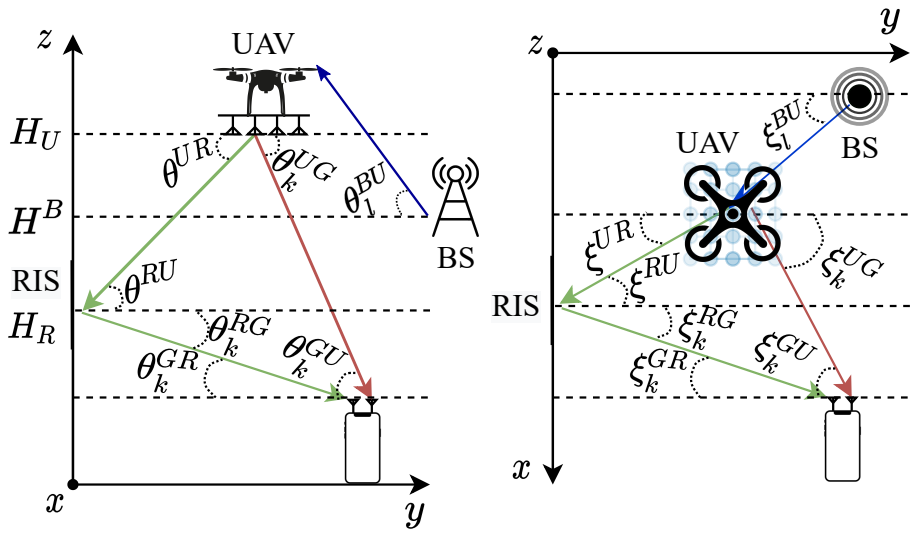

Figure 5.2: The vertical (left) and horizontal (right) AoDs / AoAs between the UAV, RIS, and k^{th} UE in the downlink communication system respectively.

fore combination of both, potentially reducing the energy consumption for in-flight movement of the UAVs. This can potentially extend the area of coverage (i.e., of the area of satisfactory QoS), also in situations where a BS could not be relied upon for service, such as emergency or disaster scenarios [177]. The chapter is structured as follows: Section 5.1 provides introduction and motivation for the usage of UAVs and RIS in cellular networks. Section 5.2 explains the optimization scenario and provides a brief formulation of the optimization problem whose solution is outlined in Section 5.3. Section 5.4 reports the simulation results for the obtained solution and the related discussion. Section 5.5 provides the conclusion and future research directions.

5.2 Scenario Definition and Problem Formulation

Consider a network environment with K UEs randomly spread in the area with a RIS in fixed and known position. We assume that the user association and additional control information needed for data transfer are exchanged between BS and UEs by means of a dedicated long range control channel. We also assume that the UEs are aware of their own position (e.g., calculated through triangulation with respect to the BSs in the area) and UAVs as well as the UEs periodically communicate this information to the BS. We also assume BSs and UAVs are equipped with Uniform Planar Square Array (UPA) antennas so as to perform concurrent beamforming in different directions and UEs are equipped with omnidirectional antenna. Additionally, for RIS, an eXtra Large scale massive MIMO (XL-MIMO) RIS deployment is considered in which every UE is served by a specific region of the surface. This holds when the RIS dimensions is large and the UEs are sufficiently spaced apart to have partial observability of the surface [189].

5.2.1 Channel Models

As visible from Figure 5.1, there are four channels in the scenario: BS to UAV, UAV to UE, UAV to RIS and RIS to UE.

BS to UAV (h^{BU}) Channel We consider the channel model proposed in [190], which provides a relation between the position and height of the UAV with respect to the position and height of the BS. We assume a LoS channel based on the UAV-UE channel model from [178]. From Figure 5.1, we devise $d^{BU}[n] = \sqrt{\|\mathbf{Z}^{BS} - \mathbf{Z}[n]\|^2}$ as the Euclidean distances between UAV and BS where $\mathbf{Z}[n] = [x_U[n], y_U[n], H_U]$ and $\mathbf{Z}^{BS} = [x_B, y_B, H_B]$ are the coordinates of UAV and BS at a particular time instant n. So, the LoS channel from BS to UAV is given by

$$\begin{aligned} h^{BU}[n] = \sqrt{\frac{\alpha_0}{(d^{BU}[n])^2}}[1, e^{-j\frac{2\pi\Delta_{Bx}}{\lambda_c}\sin\theta^{BU}\cos\xi^{BU}}, \\ \ldots, e^{-j\frac{2\pi\Delta_{Bx}}{\lambda_c}(M_{Bx}-1)\sin\theta_k^{BU}\cos\xi^{BU}}]^H \\ \otimes [1, e^{-j\frac{2\pi\Delta_{By}}{\lambda_c}\sin\theta^{BU}\sin\xi^{BU}}, \\ \ldots, e^{-j\frac{2\pi\Delta_{By}}{\lambda_c}(M_{By}-1)\sin\theta^{BU}\sin\xi^{BU}}]^H \in \mathbb{C}^{M_B\times 1} \end{aligned} \tag{1}$$

where, $\mathbf{h}^{BU}[n]$ is the channel vector based on the Angle of Departure (AoD). Δ_{Bx} and Δ_{By} are the separation between antenna elements in x-direction and y-direction for UE. Also, M_{Bx} and M_{By} is the number of antenna elements in x and y-direction for BS, $M_B = M_{Bx} \times M_{By}$ is total number of antenna elements for BS and λ_c is the carrier wavelength. θ^{BU} and ξ^{BU} are the AoD for the link from BS to the UAV. From Figure 5.2, it can be observed that $\sin\theta^{BU} = \frac{\|H_B\|}{d^{BU}}$, $\sin\xi^{BU} = \frac{\|x_B - x_U[n]\|}{\|l_B - l_U[n]\|}$ and $\cos\xi^{BU} = \frac{\|y_B - y_U[n]\|}{\|l_B - l_U[n]\|}$ where, $l_B = [x_B, y_B]$ and $l_U[n] = [x_U[n], y_U[n]]$.

UAV to UE (h^{UG}) Channel For the link between UAV and UE, which is LoS and between UAV and UE through RIS, we adopt the channel model from [178]. The UAV, RIS and UE, as previously mentioned, have a UPA antenna with M_U, M_R and M_G elements, respectively. Due to our XL-MIMO RIS assumption, the channel model we propose corresponds to each subsection / group of elements in the XL-MIMO RIS that we are using to serve different UEs, similar to the approach proposed in [191] to reflect sharp beams towards specific destinations. We assume that these groups have sufficient spatial separation thereby neglecting interference among them. From Figure 5.1, we devise $d^{UR} = \sqrt{\|\mathbf{Z}^{RIS} - \mathbf{Z}[n]\|^2}$, $d_k^{UG} = \sqrt{\|\mathbf{Z}_k^{UE} - \mathbf{Z}[n]\|^2}$, and $d_k^{RG} = \sqrt{\|\mathbf{Z}^{RIS} - \mathbf{Z}_k^{UE}\|^2}$ as the Euclidean distances between UAV and RIS, UAV and k^{th}UE and RIS and k^{th} UE respectively, where $\mathbf{Z}^{RIS} = [x_R, y_R, H_R]$ and $\mathbf{Z}_k^{UE} = [x_{G,k}, y_{G,k}, 0]$ are the coordinates of RIS and k^{th} UE. So, the LoS channel from UAV to UE is given by

$$
\begin{aligned}
h_k^{UG}[n] = \sqrt{\frac{\alpha_0}{(d_k^{UG}[n])^2}}[1, e^{-j\frac{2\pi\Delta_{Ux}}{\lambda_c}\sin\theta_k^{UG}\cos\xi_k^{UG}}, \\
\ldots, e^{-j\frac{2\pi\Delta_{Ux}}{\lambda_c}(M_{Ux}-1)\sin\theta_k^{UG}\cos\xi_k^{UG}}]^H \\
\otimes [1, e^{-j\frac{2\pi\Delta_{Uy}}{\lambda_c}\sin\theta_k^{UG}\sin\xi_k^{UG}}, \\
\ldots, e^{-j\frac{2\pi\Delta_{Uy}}{\lambda_c}(M_{Uy}-1)\sin\theta_k^{UG}\sin\xi_k^{UG}}]^H \in \mathbb{C}^{M_U\times 1}
\end{aligned}
\tag{2}
$$

where, $h_k^{UG}[n]$ is the channel vector based on the AoD and λ_c is the carrier wavelength. θ_k^{UG} and ξ_k^{UG} are the AoD for the link from UAV to k^{th} UE. From Figure 5.2, it can be observed that $\sin\theta_k^{UG} = \frac{\|H_U\|}{d_k^{UG}}$, $\sin\xi_k^{UG} = \frac{\|x_{G,k} - x_U[n]\|}{\|l_{G,k} - l_U[n]\|}$ and $\cos\xi_k^{UG} = \frac{\|y_{G,k} - y_U[n]\|}{\|l_{G,k} - l_U[n]\|}$ where, $l_{G,k} = [x_{G,k}, y_{G,k}]$ and $l_U[n] = [x_U[n], y_U[n]]$.

UAV to RIS to UE (h^{URG}) Channel Similarly, the channel from UAV to RIS is defined as follows

$$
\begin{aligned}
H^{UR}[n] &= h^{RU}[n] \otimes (h^{UR}[n])^H \\
&= \sqrt{\frac{\alpha_0}{(d^{UR}[n])^2}}[1, e^{-j\frac{2\pi\Delta_{Rx}}{\lambda_c}\sin\theta^{RU}\cos\xi^{RU}}, \\
&\ldots, e^{-j\frac{2\pi\Delta_{Rx}}{\lambda_c}(M_{Rx}-1)\sin\theta^{RU}\cos\xi^{RU}}]^H \\
&\otimes [1, e^{-j\frac{2\pi\Delta_{Ry}}{\lambda_c}\sin\theta^{RU}\sin\xi^{RU}}, \\
&\ldots, e^{-j\frac{2\pi\Delta_{Ry}}{\lambda_c}(M_{Ry}-1)\sin\theta^{RU}\sin\xi^{RU}}]^H \\
&\otimes [1, e^{-j\frac{2\pi\Delta_{Ux}}{\lambda_c}\sin\theta^{UR}\cos\xi^{UR}}, \\
&\ldots, e^{-j\frac{2\pi\Delta_{Ux}}{\lambda_c}(M_{Ux}-1)\sin\theta^{UR}\cos\xi^{UR}}] \\
&\otimes [1, e^{-j\frac{2\pi\Delta_{Uy}}{\lambda_c}\sin\theta^{UR}\sin\xi^{UR}}, \\
&\ldots, e^{-j\frac{2\pi\Delta_{Uy}}{\lambda_c}(M_{Uy}-1)\sin\theta^{UR}\sin\xi^{UR}}], \in \mathbb{C}^{M_R\times M_U}
\end{aligned}
\tag{3}
$$

where, $h^{RU}[n]$ and $h^{UR}[n]$ are the channel vectors based on the Angle of Arrival (AoA) and AoD respectively, $d^{UR}[n]$ is the distance between the UAV and RIS, Δ_{Rx} and Δ_{Ry} is the separation between antenna elements in x-direction and y-direction for RIS and Δ_{Ux} and Δ_{Uy} is the separation between antenna elements in x-direction and y-direction for UAV.

Also, M_{Rx} and M_{Ry} is the number of antenna elements in x and y-direction for RIS and M_{Ux} and M_{Uy} are the number of antenna elements in x and y-direction for UAV, λ_c is the carrier wavelength. θ^{RU} and ξ^{RU} are the AoA and θ^{UR} and ξ^{UR} are the AoD for the link from UAV to RIS. From Figure 5.2, it can be observed that $\theta^{RU} = \theta^{UR}$ and $\xi^{RU} = \xi^{UR}$. So $\sin\theta^{RU} = \sin\theta^{UR} = \frac{\|H_U - H_R\|}{d^{UR}}$,

$\sin\xi^{RU} = \sin\xi^{UR} = \frac{\|x_R - x_U[n]\|}{\|l_R - l_U[n]\|}$ and $\cos\xi^{RU} = \cos\xi^{UR} = \frac{\|y_R - y_U[n]\|}{\|l_R - l_U[n]\|}$ where, $l_R = [x_R, y_R]$. Subsequently, the channel from RIS to k^{th} UE is defined as follows

$$\begin{aligned} h_k^{RG} = \sqrt{\frac{\alpha_0}{(d_k^{RG})^2}}[1, e^{-j\frac{2\pi\Delta_{Rx}}{\lambda_c}\sin\theta_k^{RG}\cos\xi_k^{RG}}, \\ \ldots, e^{-j\frac{2\pi\Delta_{Rx}}{\lambda_c}(M_{Rx}-1)\sin\theta_k^{RG}\cos\xi_j^{RG}}]^H \\ \otimes [1, e^{-j\frac{2\pi\Delta_{Ry}}{\lambda_c}\sin\theta_k^{RG}\sin\xi_k^{RG}}, \\ \ldots, e^{-j\frac{2\pi\Delta_{Ry}}{\lambda_c}(M_{Ry}-1)\sin\theta_k^{RG}\sin\xi_k^{RG}}]^H, \in \mathbb{C}^{M_R\times 1} \end{aligned} \tag{4}$$

where, $h^{RG}[n]$ is the channel vector based on the AoD respectively, $d_k^{RG}[n]$ is the distance between the RIS and UE, Δ_{Rx} and $\Delta_{Ry}$is the separation between antenna elements in x-direction and y-direction for RIS. Also, M_{Rx} and M_{Ry} is the number of antenna elements in x and y-direction for RIS and λ_c is the carrier wavelength. Additionally, θ^{RG} and ξ^{RG} are the AoD for the link from RIS to k^{th} UE. From Figure 5.2, it can be observed that $\sin\theta_k^{RG} = \frac{\|H_R\|}{d_k^{RG}}$, $\sin\xi_k^{RG} = \frac{\|x_{G,k} - x_R\|}{\|l_{G,k} - l_R\|}$ and $\cos\xi_k^{RG} = \frac{\|y_{G,k} - y_R\|}{\|l_{G,k} - l_R\|}$. Additionally, the phase shift introduced in the reflected signal by RIS is defined as

$$\begin{aligned} \Phi_k[n] = \mathrm{diag}(e^{j\Phi_{1,1,k}[n]}, \ldots, e^{j\Phi_{m_{Rx},m_{Ry},k}[n]}, \\ \ldots, e^{j\Phi_{M_{Rx},M_{Ry},k}[n]}) \in \mathbb{C}^{M_R\times M_R}, \end{aligned} \tag{5}$$

where $\Phi_{m_{Rx},m_{Ry},k}[n] \in [0, 2\pi), m_{Rx} = \{1, \ldots, M_{Rx}\}, m_{Ry} = \{1, \ldots, M_{Ry}\}$ represents the phase control introduced to the $(m_{Rx}, m_{Ry})^{th}$ reflecting element of the RIS. Hence, end-to-end effective channel between the UAV and the k^{th} UE reflected by the RIS is given by

$$(H_k^{URG}[n])^H = (h_k^{RG}[n])^H \Phi_k[n] H^{UR}[n] \in \mathbb{C}^{1\times M_U}. \tag{6}$$

Hence, the Signal-to-Noise Ratio (SNR) is given by

$$\gamma^U[n] = \frac{P_U^T |h^{BU}[n]|^2}{\sigma_n^2}, \tag{7}$$

$$\gamma^{k,1}[n] = \frac{P_{1,k}^T |h_k^{UG}[n]|^2}{\sigma_n^2}, \tag{8}$$

$$\gamma^{k,2}[n] = \frac{P_{2,k}^T |H_k^{URG}[n]|^2}{\sigma_n^2}, \tag{9}$$

where, P_U^T is the transmit power for BS towards the UAV, $P_{1,k}^T$ is the transmit power for the UAV towards the k^{th} UE over the LoS link, $P_{2,k}^T$ is the transmit power for the UAV towards the k^{th} UE over the RIS link, and σ_n^2 is the white noise power. Communication using (7) and assuming a Gaussian channel, the maximum achievable rate for the channel between BS to UAV, UAV to UE

Table 5.1: Notation for Energy Consumption Model[178]

Symbol	Meaning	Simulation Values
Ω	Blade Angular Velocity	300 rad/s
r	Rotor radius	0.4 m
ρ	Air Density	1.225 kg/m^3
s	Rotor Solidity	0.05 m^3
A_r	Rotor Disc Area	0.503 m^3
v_0	Forward Flight Rotor Induced velocity	4.03 m^3
d_0	Fuselage drag ratio	0.3
P_0	Blade profile power in hovering status	79.86 W
P_p	Induced power in hovering status	88.63 W

with and without RIS is given by the Shannon bound

$$R^U[n] = \log_2(1 + \gamma^U[n]) \qquad [\text{bits/s/Hz}], \tag{10}$$

$$R_k^i[n] = \log_2(1 + \gamma^{k,i}[n]) \qquad [\text{bits/s/Hz}]. \tag{11}$$

where $i \in \{1, 2\}$, $R^U[n]$ is the rate achieved by the UAV over the BS-UAV LoS channel and $R_k^i[n]\ \forall\, i$ is the rate achieved by the k^{th} UE over the corresponding UAV-UE and UAV-RIS-UE channels respectively. Note that, to use the above formula, we must assume that BS, UAV and UE know the channel between them and can determine the rate based on the available SNR. Also, we assume that the UEs are sufficiently spread apart to avoid mutual interference when communicating with the UAV.

5.2.2 Energy Consumption for UAV

The power consumption for UAV is critical due to its limited battery capacity. In the chapter, we use the distance-based energy consumption model from [192] given by

$$P^U[n] = \underbrace{P_o\left(1 + \frac{3\|\mathbf{v}[n]\|^2}{\Omega^2 r^2}\right)}_{\text{Bladeprofile}} + \underbrace{\frac{P_i v_0}{\|\mathbf{v}[n]\|}}_{\text{Induced}} + \underbrace{\frac{1}{2} d_0 \rho s A_r \|\mathbf{v}[n]\|^3}_{\text{Parasite}}, \tag{12}$$

where $\mathbf{v}[n]$ is the velocity vector, and the other terms of the equation are explained in Table 5.1. We only considered the energy consumption for the in-flight movement of the UAV for now and keep the impact of take off and landing on energy consumption for further research.

5.2.3 Optimization Problem

Considering the assumptions, the objective is to find an energy efficient UAV path and corresponding RIS phase shift in order to minimize the overall transmission power consumption of UAV and BS under minimum QoS constraints and maximum UAV energy budget which is defined as

$$\min_{\mathbf{P},\mathbf{Z},\mathbf{V},\mathbf{\Phi}} \sum_{n=1}^{N} P_U^T[n] + \sum_{n=1}^{N}\sum_{k=1}^{K}\sum_{i=1}^{2} P_{i,k}^T[n] \tag{13}$$

s.t.

$$\begin{aligned}
&C1: \sum_{i=1}^{2} R_k^i[n] \geq R_{min}, \forall\, k, n;\\
&C2: R^U[n] \geq \sum_{k=1}^{K}\sum_{i=1}^{2} R_k^i[n],\ \forall\, n;\\
&C3: 0 \leq \mathbf{\Phi}[n] \leq 2\pi;\\
&C4: \sum_{n=1}^{N} P^U[n] \leq E_{max}^{UAV};\\
&C5: \mathbf{Z}[n+1] = \mathbf{Z}[n] + \mathbf{v}[n]\tau,\ n = 1, \ldots, N-1;\\
&C6: \|\mathbf{v}[n]\| \leq V_{max},\ \forall n;\\
&C7: \|\mathbf{v}[n+1] - \mathbf{v}[n]\| \leq V_{acc}\tau,\ n = 1, \ldots, N-1;\\
&C8: \|\mathbf{v}[n]\| \geq 0\ \forall n;\\
&C9: \mathbf{Z}[1] = \mathbf{Z}_0;\\
&C10: \mathbf{Z}[N] = \mathbf{Z}_F.
\end{aligned}$$

Optimization Variables

The terms of this optimization problem are explained below:

- $\mathbf{P}$: UAV (P_k^T) and BS (P_{BS}^T) transmission power.
- $\mathbf{Z}$: UAV trajectory, represented as the sequence of geographical coordinates of the UAV at each timestep.
- $\mathbf{V}$: UAV velocity over the trajectory.
- $\mathbf{\Phi}$: RIS phase configurations.

Objective Function

The objective is to minimize the overall energy consumption of UAV and BS for transmission during the N timesteps taken by the UAV to cover its trajectory.

Constraints

C1–Guaranteed Rate Constraint C1 is devised to provide a guaranteed service rate to each one of the K UEs. We recall that R_k is the sum rate achieved over the LoS and RIS link, which has to stay above the guaranteed rate R_{min}.

C2–Backhaul Capacity Constraint C2 ensures that the backhaul link capacity is greater than or equal to the aggregate minimum guaranteed rate for all the UEs, i.e., that the UAV has enough bandwidth capacity towards the BS to provide at least the minimum guaranteed rate to all the UEs.

C3–Phase Shift Constraint C3 limits the phase shift with respect to the incident signal from 0 to 2π. With the assumption of XL-MIMO surface for RIS, the phase shift can be considered almost continuous from 0 to 2π.

C4–UAV Energy Budget C4 requires that the total energy consumption of the UAV over N timesteps does not exceed the threshold E_{max}^{UAV} that defines the maximum energy the UAV can spend before recharging and, implicitly, the maximum length of the UAV path.

C5–Timestep Position Constraint C5 constraints the position $Z[n]$ in successive timesteps, thereby limiting the movement of the UAV in one timestep.

C6–Maximum Velocity Constraint C6 is devised to constraint the velocity $\mathbf{v}[n]$ of the UAV in one timestep to be lower than or equal to the maximum velocity V_{max}, thereby limiting the maximum distance the UAV can travel in one timestep.

C7–Timestep Velocity Constraint C7 is devised to determine the velocity $\mathbf{v}[n]$ of the UAV in successive timesteps based on the maximum acceleration V_{acc} of UAV in one timestep.

C8–Minimum Velocity Constraint C8 constraints the velocity $\mathbf{v}[n]$ of the UAV, thereby limiting the minimum distance the UAV can travel over one timestep. Note that, if the UAV can hover at one place in one timestep, then the minimum velocity is zero.

C9/C10–Initial/Final Position Constraint C9 and C10 fix the starting and ending points of the trajectory otherwise determined by the optimization problem.

We remark that, as shown in Figure 5.1 the UAV has two parallel links to each UE: one directional and the other with the RIS sector associated to the UE. The multipath approach offers a greater chance to satisfy the service requirement by jointly optimizing the UAV trajectory $\mathbf{Z}[n]$ and RIS phase configuration $\mathbf{\Phi}$, while minimizing the transmission power of the entire system. To facilitate the UEs to determine the multipath connections, the BS has to continuously communicate the beams to be used to the UE taking into account the mobility information of the UEs and

the trajectory of the UAV. As mentioned before, the BS may communicate this information over long-range low-rate technologies such as LoRa [193].

5.3 Analytical Solution

The optimization problem discussed in the previous section is clearly non-convex and, hence, quite difficult to solve in itself. But we can determine a feasible solution by considering the initial transmission powers for the UAV and BS so as to jointly optimize the UAV trajectory and RIS phase and, then, minimize the transmission powers for the given trajectory and phase configuration within the constraints in (13). This method is explained in detail in the following subsections.

5.3.1 Joint UAV Trajectory and RIS phase optimization

Joint UAV Trajectory and RIS phase optimization can be facilitated considering a particular $\mathbf{P}$ over different links [194]. As shown in the Figure 5.2, the BS to UAV, UAV to UE, UAV to RIS and RIS to UE links are assumed to be deterministic LoS channels. For ease of notation, in the following we indicate the nodes involved in a link using the subscript U, B, R and G for UAV, BS, RIS and (ground) UE, respectively. The channel information is supposed to be available at the UAV and the UEs. Hence, to maximise the transmission efficiency, a Maximum Ratio Transmission (MRT) is applied, i.e., the transmission beamformer for any k^{th} UE as well as for the UAV can be defined as $w^{BU} = \frac{1}{\sqrt{M_B}} h^{BU}$, $w_k^{UG} = \frac{1}{\sqrt{M_U}} h^{UG}$ and $w^{UR} = \frac{1}{\sqrt{M_U}} h^{UR}$. The overall channel gains can hence be obtained as

$$H^{BU}[n] = (h^{BU}[n])^H w^{BU}[n] = \frac{\sqrt{M_B}\alpha_0}{d^{BU}[n]}; \tag{14}$$

$$H_k^{UG}[n] = (h_k^{UG}[n])^H w_k^{UG}[n] = \frac{\sqrt{M_U}\alpha_0}{d_k^{UG}[n]}; \tag{15}$$

$$\begin{aligned} H_k^{URG}[n] &= (h_k^{RG}[n])^H \mathbf{\Phi}_k[n] H^{UR}[n] w^{UR}[n] \\ &= \sqrt{M_U}(h_k^{RG}[n])^H \mathbf{\Phi}_k[n] h^{RU}[n] \\ &= \frac{\sqrt{M_U} M_R \alpha_0}{d_k^{RG} d^{UR}[n]}. \end{aligned} \tag{16}$$

To determine the $H_k^{URG}[n]$ coefficients correctly, the optimal phase control policy for the phase shift in every timestep (which maximizes the reflection-mode channel gain by aligning the phase of the RIS to match those of the channel), defined in [178], is given by

$$\begin{aligned} \mathbf{\Phi}_{m_{Rx}, m_{Ry}, k} = \frac{2\pi\Delta_R}{\lambda_c} [&(m_{Rx} - 1)(\sin\theta^{RU}\cos\xi^{RU} \\ &+ \sin\theta_k^{RG}\cos\xi_k^{RG}) + (m_{Ry} - 1)(\sin\theta^{RU}\sin\xi^{RU} \\ &+ \sin\theta_k^{RG}\sin\xi_k^{RG})], \end{aligned} \tag{17}$$

where θ^{RU} and ξ^{RU} are the AoAs and θ^{RG} and ξ^{RG} are the AoDs as defined in Figure 5.2. The assumption for RIS phase configuration is that there is a wired direct link to the RIS controller and that, delay and imperfect phase configuration are negligible.
Note that, the problem is still non-convex due to C1 and C2 w.r.t. $\mathbf{Z}$. In order to overcome this issue, we add three slack variables $\lambda_{k,i}[n]$ and $\pi[n]$. In this way, we keep the constraints C1-9, and the problem can be reformulated as follows

$$\min_{\mathbf{Z},\mathbf{V},\mathbf{\Lambda},\mathbf{M},\mathbf{\Pi}} \sum_{n=1}^{N} P_U^T[n] + \sum_{n=1}^{N}\sum_{k=1}^{K}\sum_{i=1}^{2} P_{i,k}^T[n] \tag{18}$$

s.t.

$$\begin{aligned}
&C1 - \ C10;\\
&C11: \ \|\mathbf{Z}_k^{UE} - \mathbf{Z}[n]\|^2 \leq \lambda_{k,1}[n], k \in \{1,...,K\};\\
&C12: \ \|\hat{\mathbf{Z}}_k^{RIS} - \mathbf{Z}[n]\|^2 \leq \lambda_{k,2}[n], k \in \{1,...,K\};\\
&C13: \ \|\mathbf{Z}^{BS} - \mathbf{Z}[n]\|^2 \leq \mu[n];\\
&C14: \ \|\mathbf{v}[n]\|^2 \geq \pi^2[n];\\
&C15: \ \pi[n] \geq 0;
\end{aligned}$$

where $\mathbf{\Lambda} = \{\lambda_{k,i}[n], \forall\, n, k, i\}$, $\mathbf{M} = \{\mu[n], \forall\, n\}$ and $\mathbf{\Pi} = \{\pi[n], \forall\, n\}$. Similarly to what proposed in [178], we overcome the non-convex constraints C1 and C2 via Successive Convex Approximation (SCA) in an iterative way. We can compute a lower bound of the instant achievable rate for each user by modifying $\lambda_{k,i}[n]$, $\mu[n]$ and $\pi[n]$ and calculating the first-order Taylor expansion which is a global under-estimator of the rate convex function [195]. Hence, omitting the argument $[n]$ for notation clarity, we redefine the SNR expression as

$$\gamma^U = \frac{\hat{\gamma}^U}{\mu}; \tag{19}$$

$$\gamma^{k,i} = \frac{\hat{\gamma}^{k,i}}{\lambda_{k,i}}, \ \forall\, i = \{1,2\}, \tag{20}$$

where,

$$\hat{\gamma}^U = \frac{P_U^T M_B \alpha_0^2}{\sigma_n^2}; \tag{21}$$

$$\hat{\gamma}^{k,1} = \frac{P_{1,k}^T M_U \alpha_0^2}{\sigma_n^2}; \tag{22}$$

$$\hat{\gamma}^{k,2} = \frac{P_{2,k}^T M_U M_R^2 \alpha_0^2}{(d_k^{RG})^2 \sigma_n^2}. \tag{23}$$

Using (19) and (20) in (10) and (11) respectively and applying the first-order Taylor expansions in the j-th iteration for a particular value of $\lambda_{k,i}^j[n]$, $\mu^j[n]$ and $\mathbf{v}^j[n]$, the lower bound for the rates is

given by

$$\begin{aligned}
&\hat{R}_k^i[n] \geq \\
&(\hat{R}_k^i[n])^j = \log_2\left(1+\frac{\gamma^{i,k}[n]}{\lambda_{k,i}^j[n]}\right) \\
&\qquad -\frac{\gamma^{i,k}[n](\lambda_{k,i}[n]-\lambda_{k,i}^j[n])}{\lambda_{k,i}^j[n](\lambda_{k,i}^j[n]+\gamma^{i,k}[n])\ln 2}, \qquad (24)\\
&\hat{R}^U[n] \geq \\
&(\hat{R}^U[n])^j = \log_2\left(1+\frac{\gamma^U[n]}{\mu^j[n]}\right) \\
&\qquad -\frac{\gamma^U[n](\mu[n]-\mu^j[n])}{\mu^j[n](\mu^j[n]+\gamma^U[n])\ln 2}, \qquad (25)\\
&\|\mathbf{v}[n]\|^2 \geq \|\mathbf{v}^j[n]\|^2 + 2[\mathbf{v}^j[n]]^T(\mathbf{v}[n]-\mathbf{v}^j[n]). \qquad (26)
\end{aligned}$$

where $(\hat{R}_k^i[n])^j$ and $(\hat{R}_U[n])^j$ are the lower bound achievable rates for the k^{th} UE and UAV respectively, in the j^{th} iteration of SCA.

The in-flight power consumption for UAV can be written as

$$P^U[n] = P_o\left(1+\frac{3\|\mathbf{v}[n]\|^2}{\Omega^2 r^2}\right) + \frac{P_p v_0}{\pi[n]} + \frac{1}{2}d_0\rho_s A_r\|\mathbf{v}[n]\|^3. \qquad (27)$$

Applying the lower bounds in (24), (25) and (26) in (18) we obtain a convex problem defined as

$$\begin{aligned}
&\min_{\mathbf{Z},\mathbf{V},\mathbf{\Lambda},\mathbf{M},\mathbf{\Pi}} \sum_{n=1}^{N} P_U^T[n] + \sum_{n=1}^{N}\sum_{k=1}^{K}\sum_{i=1}^{2} P_{i,k}^T[n] \qquad (28)\\
&\quad \text{s.t.}\\
&\hat{C}1: \sum_{i=1}^{2}(\hat{R}_k^i[n])^j \geq R_{min}, \forall\, k;\\
&\hat{C}2: (\hat{R}^U[n])^j \geq \sum_{k=1}^{K}\sum_{i=1}^{2}(\hat{R}_{k,i})^j[n];\\
&\hat{C}14: \|\mathbf{v}^j[n]\|^2 + 2[\mathbf{v}^j[n]]^T(\mathbf{v}[n]-\mathbf{v}^j[n]) \geq \pi^2[n];\\
&\quad C3-C15,
\end{aligned}$$

which solving it provides an upper bound of the problem in (18). We iteratively update the feasible solution $\mathbf{Z}^j[n]$, $\lambda_{k,i}^j[n]$, $\mu^j[n]$, $\mathbf{v}^j[n]$ and $\pi^j[n]$ by solving the convex problem in (28) using the CVX standard optimization solver [196] in the j-th iteration.

5.3.2 Transmission Power Control

For a determined UAV trajectory and RIS phase, the UAV and BS transmission power can be minimized. To define the transmission power minimization with a predefined trajectory $\mathbf{Z}$, the optimization problem in (13) can be rewritten with constraints C3 – C10 already satisfied for the pre-defined trajectory $\mathbf{Z}$. So the optimization problem can be written as

$$\min_{\mathbf{P}} \sum_{k=1}^{K}\sum_{n=1}^{N}\sum_{i=1}^{3} P_i^T[n] \tag{29}$$

s.t.

$$\text{C1}: \sum_{i=1}^{2} R_k^i[n] \geq R_{min}, \forall\, k, n;$$

$$\text{C2}: C[n] \geq \sum_{k=1}^{K}\sum_{i=1}^{2} R_k^i[n], \ \forall\, n.$$

The constraints C1 and C2 are concave with respect to the $\mathbf{P}$. Hence it can be easily solved by employing SCA using the Taylor's expansions, which are global over-estimators of the concave functions [195]. To do so, the SNR expressions are rewritten as

$$\gamma^U[n] = P_U^T[n]\kappa_U[n]; \tag{30}$$

$$\gamma^{i,k}[n] = P_{i,k}^T[n]\kappa_{k,i}[n], \forall\, i \in \{1,2\}, \ k; \tag{31}$$

where,

$$\kappa_U[n] = \left\{\frac{\sqrt{M_B}\alpha_0}{d^{BU}[n]\sigma}\right\}^2, \tag{32}$$

$$\kappa_{k,1}[n] = \left\{\frac{\sqrt{M_U}\alpha_0}{d^{UG}[n]\sigma}\right\}^2, \tag{33}$$

$$\kappa_{k,2}[n] = \left\{\frac{\sqrt{M_U}\alpha_0}{d^{URG}[n]\sigma}\right\}^2. \tag{34}$$

Using (30) and (31) in (10) and (11) respectively and applying the first-order Taylor expansions, we get

$$\hat{R}^{U}[n] \leq$$
$$(\hat{R}^{U}[n])^{j} = \log_2\left(1 + (P_U^T)^j|\kappa_U[n]|^2\right) + \frac{|\kappa_U[n]|^2(P_U^T - (P_U^T)^j)}{(1 + (P_U^T)^j|\kappa_U[n]|^2)\ln(2)}, \tag{35}$$
$$\hat{R}_k^{i}[n] \leq$$
$$(\hat{R}_k^{i}[n])^{j} = \log_2\left(1 + (P_{i,k}^T)^j|\kappa_{k,i}[n]|^2\right) + \frac{|\kappa_{k,i}[n]|^2(P_{i,k}^T - (P_{i,k}^T)^j)}{(1 + (P_{i,k}^T)^j|\kappa_{k,i}[n]|^2)\ln(2)}, \ \forall\, i \in \{1,2\}. \tag{36}$$

Hence, the optimization problem (29) can be rewritten as

$$\min_{\mathbf{P}} \ \sum_{n=1}^{N} P_U^T[n] + \sum_{n=1}^{N}\sum_{k=1}^{K}\sum_{i=1}^{2} P_{i,k}^T[n] \tag{37}$$
$$\text{s.t.}$$
$$\text{C1}: \ \sum_{i=1}^{2}(\hat{R}_k^{i}[n])^{j}[n] \geq R_{\min}, \forall\, k, n;$$
$$\text{C2}: \ (\hat{R}^{U}[n])^{j}[n] \geq \sum_{k=1}^{K}\sum_{i=1}^{2}(\hat{R}_k^{i})^{j}[n], \ \forall\, n.$$

Similar to the UAV trajectory and RIS phase optimization problem, this optimization can be solved using the CVX standard optimization solver. Algorithm 5.1 provides the pseudocode to solve the optimization problem. Note that, we are aiming to minimize the transmission energy consumption of the UAV and BS by iteratively choosing a UAV route aided by the phase shifting involved in the RIS, which satisfies a target minimum rate for all the users, taking into account the rate aggregation of all the users is achievable, fulfilling the backhaul link capacity limitation, something not addressed in the literature to the best of the authors' knowledge.

Determination of Initial Trajectory The major hurdle for SCA is the existence of an initial trajectory that satisfies the constraints i.e. a feasible solution for the designed optimization problem. To the best of the authors' knowledge, there has not been a clear procedure to obtain an initial trajectory for trajectory optimization aside from arbitrary trajectory initialization. To overcome this hurdle, we consider the optimization problem in Eqn (13) with a constant objective function instead of minimizing the power so as to determine a initial feasible solution that satisfies the

constraints.

The major hurdle are the constraints C1 and C2 which are inherently non-convex and can only be made convex by using SCA. To overcome this, we translate the constraints from rate received at the UE to the power necessary for transmission at the base station and the UAV. To do such, in case of constraint C1, we assume that, the UAV has all the data it needs to transmit, i.e. the BS transmits at a very high power to satisfy C2 constraint, and then divide the constraint C1 into two different parts with respect to the two links, i.e. LoS and RIS link and devise the C1 constraint such that at least one of the links satisfies the overall C1 constraint. In the same way, for constraint C2, we assume that the UAV is able to provide the required rate to the UEs at a very high transmit power and the devise the constraint C2 such that it satisfies the combined minimum rate received by the UEs. We then solve this optimization problem with altered C1 and C2 constraints with CVX standard optimization solver to obtain the initial trajectory which is a feasible solution.

Algorithm 5.1 Joint Trajectory, RIS Phase Configuration and Transmission Power Control algorithm.

Output UAV Trajectory $\mathbf{Z}$, UAV Velocity $\mathbf{V}$, P^{Total}

Initialize trajectory $\mathbf{Z}$, $\mathbf{V}$, maximum number of iteration J_{max}, Initial iteration index $j = 0$, Particular UAV and BS transmission power $\mathbf{P}$, Initial trajectory $\mathbf{Z}$, Initial velocity $\mathbf{V}$ and convergence tolerance ϵ

while $j \leq J_{max}$ or $\frac{P^{j}_{Total} - P^{j-1}_{Total}}{P^{j}_{Total}} \leq \epsilon$ **do**

Set $j = j + 1$ and $\{\mathbf{P}^j, \mathbf{V}^j, \mathbf{\Lambda}^j, \mathbf{M}^j, \mathbf{\Pi}^j\} = \{\mathbf{P}, \mathbf{V}, \mathbf{\Lambda}, \mathbf{M}, \mathbf{\Pi}\}$

Solv optimization problem (28) to obtain $\mathbf{Z}, \mathbf{V}, \mathbf{\Lambda}, \mathbf{M}$ and $\mathbf{\Pi}$ for a Particular $\mathbf{P}$

Solve optimization problem (37) to obtain $\mathbf{P}$ and P_{Total} for a Particular $\mathbf{Z}, \mathbf{V}, \mathbf{\Lambda}, \mathbf{M}, \mathbf{\Pi}$

Update $P^{j}_{Total} = P_{Total}$

end while

5.4 Results and Discussion

The solution discussed in the previous section is implemented in MATLAB simulation environment. The base simulation parameters are defined by Table 5.2. The simulation environment is shown in the Figure 5.3. As visible from the figure, over the SCA iterations, the UAV trajectory and transmission power is optimized using Algorithm 5.1 until it converges, i.e., UAV trajectory and transmission power are no longer improved.

5.4.1 UAV LoS transmission power v/s UAV RIS transmission power

Different configurations in terms of static number of UEs in the network have been simulated. Looking at the total transmission power used along the optimized trajectory, that is, the summation of the power from the BS and the transmission power for the UAV, Figure 5.4 shows now that the power increases with the number of users in the network for different values of R_{min}. To be noted that the curve bends when the number of users increases, since their distance to the

Table 5.2: Simulation Parameters.

Parameter	Value
Area	500m $\times$ 500m
Number of Users (K)	3
Position of Users	[20, 450; 250, 0; 500, 200]
Position of Base Station	[0, 0]
Position of RIS	[200, 500]
Number of RIS Elements per user	64
Number of UAVs	1
Initial / Final Position of UAV (Z_0/Z_F)	[0, 0; 500, 500]
Maximum Velocity	20 m / s
Maximum Acceleration	4 m / s^2
Height of the [UAV, BS, RIS]	[20,15,10] m
Path Loss (α_0)	61 dBm
Noise Power Spectral Density (σ^2)	-174 dBm

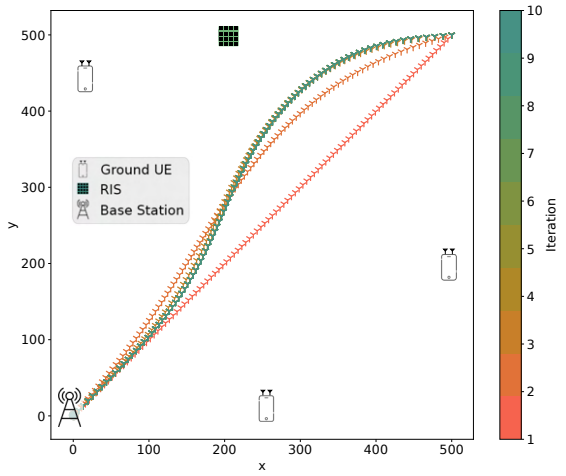

Figure 5.3: Optimization of the UAV trajectory and transmission power over SCA iterations. The marked lines represent the UAV trajectories obtained during the execution of the iterative algorithm. The straight line is the initial solution, while the darkest one is the final solution.

BS, UAV and RIS reduces. Also, the total power increases with the minimum rate requirement. Another significant observation is the change in average power consumption per set of users for different rates. The change in principle should be exponential, i.e., linear increase in rate should require exponential increase in power. But, to follow this criteria, the distance has to be constant, i.e., the trajectory of the UAV has to be constant for all the different rates. But, as visible in Figure 5.5, which shows the optimal trajectories for different values of R_{min}, the optimal trajectory for $R_{min} = 0.057$ is able to deviate more from the straight line trajectory as it can still satisfy the low required minimum rate for the UEs. On the contrary, the optimal trajectory for $R_{min} = 0.757$ is able to deviate less from the straight line trajectory than that for $R_{min} = 0.057$ as the required minimum rate is higher. Note that, we only show optimal trajectories for $R_{min} = \{0.057, 0.257, 0.557, 0.757\}$

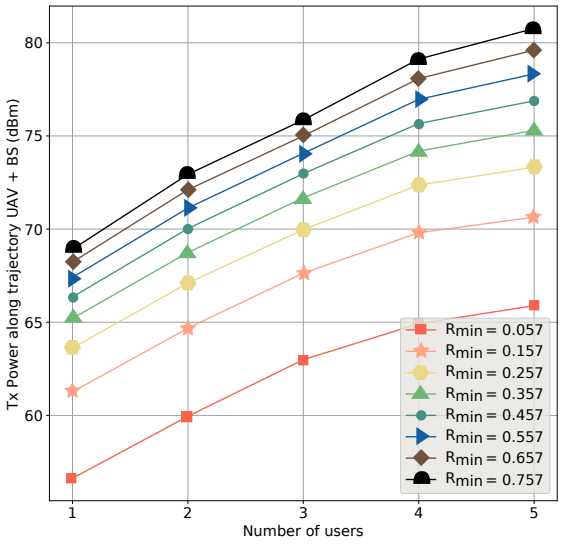

Figure 5.4: Total transmission power (UAV and BS) when increasing the number K of static UEs for different values of R_{min}.

to be able to visually distinguish between the optimal trajectories for the different values of R_{min}. The optimal trajectories for the remaining values of R_{min} are between the optimal trajectory for $R_{min} = 0.057$ and $R_{min} = 0.757$. This trend for optimal trajectories is also true for the scenarios involving one, two, four and five UEs. Hence, the average power consumption for UEs, as shown in Figure 5.4, does not follow an exponential criteria due to change in optimal trajectory for different values of R_{min}. Additionally, the system is very sensitive to the network configuration, i.e., it is inherently limited with respect to number of UEs that can be served simultaneously in a single flight. To improve the scalability of the system, the usage of reinforcement learning can be explored, which has been left for future work.

5.4.2 Impact of UAV Energy Budget on UAV Trajectory

To study the impact of the energy budget on the UAV trajectory optimization, we determine the UAV trajectories for different energy budget values. The energy consumed by the UAV over the straight line path (i.e, shortest path) is the minimum in-flight energy consumption necessary for the UAV to reach its final destination and is hence set as a reference minimum E_{min}. Hence, the energy budget for the UAV is defined as a multiple of E_{min}. Figure 5.6 denotes the impact of UAV energy budget on the trajectory optimization. As visible from the figure, when increasing the budget, the UAV is able to deviate further away from the shortest path trajectory. But eventually, it cannot go much further as it would risk not serving the users on the opposite side (as discussed previously). Once the UAV energy is sufficient to draw the optimal trajectory across the area, any further increase of the UAV energy would likely allow the UAV to slow down its speed or hover on the optimal location for a longer time, thus improving the transmission energy efficiency of

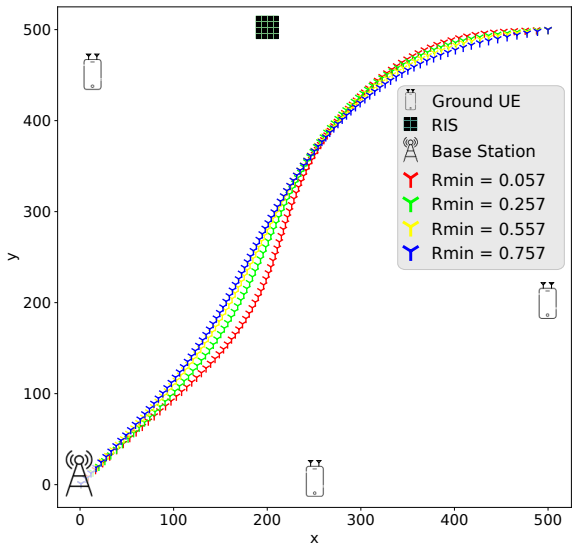

Figure 5.5: Different optimal trajectories for the UAV for three UEs and for different values of R_{min}.

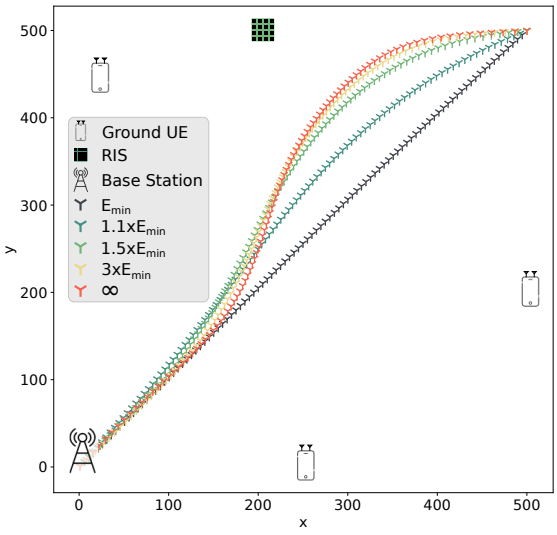

Figure 5.6: Impact of UAV energy budget on the UAV trajectory.

the system. The minimum amount of energy required to reach the optimal trajectory is hence important to dimension the UAV battery capacity.

5.4.3 Impact of RIS Position on UAV Trajectory

We analyze the impact of the different positions of RIS on the optimal UAV trajectories as shown in Figure 5.7. The first discernible observation is that the UAV attempts to go as close as possible to the RIS. This is because the transmission power necessary to satisfy the rate requirement of

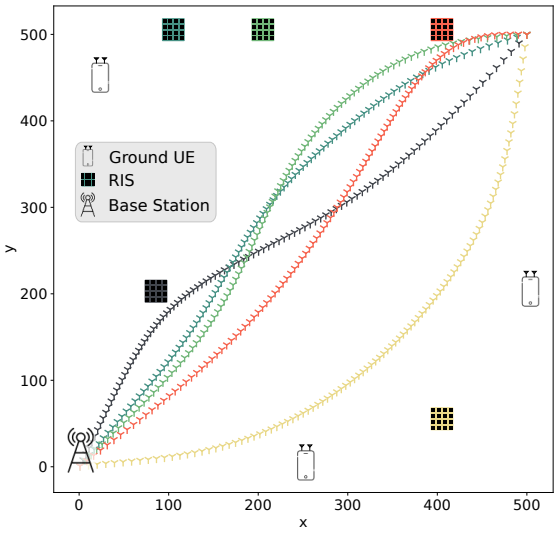

Figure 5.7: Impact of RIS position on UAV trajectory for a fixed UE and BS positions

the UEs is considerably lower when using the RIS compared to directly transmitting to the UEs. This, however, is compensated by the higher path loss that is encountered by the signal i.e. the total distance the signal has to cover using the RIS is higher than that along the LoS channel. Due to this fact, the UAV cannot use the RIS to serve all the UEs at all timesteps. Hence some UEs has to be served directly. This creates a push-pull effect on the UAV that prevents the UAV to venture very close to one UE to avoid violating the QoE requirements of the other UEs. Hence, determining an optimal position for RIS is important while designing the network.

5.4.4 Impact of RIS Position on UAV Transmission Power

As concluded in previous subsection, the UAV has a tendency to move towards the RIS. To determine the impact of the RIS position on the UAV transmission power consumption, we obtained the optimal trajectory for different network service requirements i.e. spectral efficiency or R_{min} per UE randomly chosen between 0.01 and 0.757 bits/s/Hz. Figure 5.9 shows the boxplot for the average UAV power consumption over LoS and RIS links for different positions of the RIS, as denoted in Figure 5.8, obtained for 50 different sets of values of R_{min} randomly chosen between 0.01 and 0.757 bits/s/Hz.

As visible from the figure, the RIS position is crucial with respect to not only the UEs but also the initial trajectory of the UAV. When in position 3, the RIS is closer to both the UEs and the UAV initial trajectory and hence the optimization problem uses the RIS link to serve the UEs. On the other hand, in position 2, the RIS is closer to the UE but is further away from the UAV initial trajectory and hence the RIS link is not much used by the UAV. In the other two positions, the RIS is extremely far away from the UEs and hence is also not much used.

So the optimal solution is able to use the RIS to serve the users when the RIS is closer to the UEs

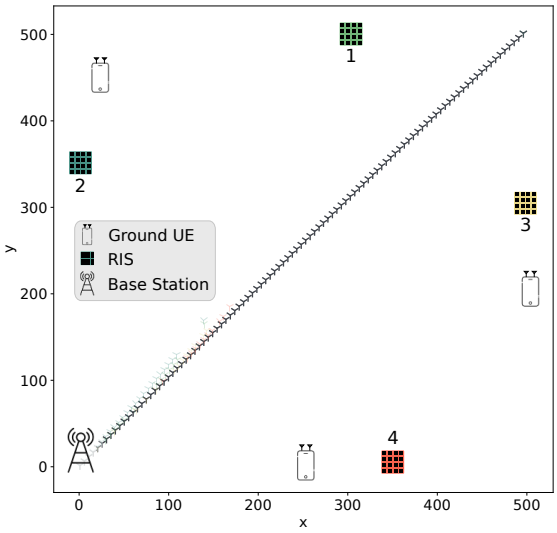

Figure 5.8: Different RIS positions configuration.

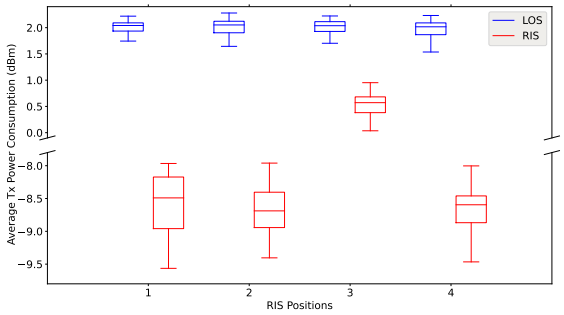

Figure 5.9: Average transmission power consumption of the UAV over the LoS and RIS link for different positions of the RIS as shown in Figure 5.8, for 50 different network service requirements.

as well as the UAV initial trajectory. This also signifies that, the SCA is extremely sensitive to network configurations especially with respect to UAV initial trajectory and RIS and UEs positions. To use SCA to determine the optimal UAV trajectory, RIS phase and UAV transmission power, it is really necessary to define an initial state (a.k.a trajectory) that a complete and feasible solution for the optimization problem. Additionally, the position of the RIS has to be optimal with respect to both UAV initial trajectory and position of the UEs. Hence, the usage of data driven methods such as reinforcement learning techniques to jointly optimize the UAV trajectory, RIS phase and UAV transmission power can be extremely lucrative and pursued for further work, as it would provide a more generalized solution regardless of the specific network configuration.

5.5 Conclusion

Beyond 5G and 6G Networks are expected to provide a certain service level while reducing the power consumption of the system. To this end, we discussed the usage of UAVs and RIS as a way to guarantee certain service requirements while trying to minimise the power consumption of the system.

In this work, we devised jointly, a method to roughly optimize UAV trajectory, RIS phase and UAV transmission power consumption to provide a certain guaranteed service rate to the UEs on the ground. We showed the usage of convex approximation techniques can provide a feasible solution. Moving forward, the usage of reinforcement learning seems very attractive especially due to the sensitive nature of convex approximation schemes to different network configurations.

6

Pilot Reuse Strategies in Cell-Free Massive MIMO Systems

6.1 Introduction

Distributed or Cell-free (CF) massive Multiple-Input, Multiple-Output (mMIMO) [14], [84], [197]–[201] has been considered as one of the potential technologies for beyond-5th Generation (5G) (B5G) and 6G wireless networks thanks to its capability of providing relatively uniform service to the User Equipments (UEs) in the coverage area. As the name implies, CF systems, unlike traditional cellular networks, do not consider the concepts of cell or cell boundaries, where a Base Station (BS) serves multiple UEs within its cell coverage. In CF mMIMO, UEs are jointly served by a relatively larger number of geographically distributed Access Points (APs) over the same time-frequency resource. CF mMIMO lies at the intersection of different technologies like mMIMO [202]–[205], Coordinated MultiPoint (CoMP) [206], [207] and Ultra Dense Network (UDN) [208], [209], combing the best of each technology, while eliminating their deficiencies [199]. CF mMIMO adopts its physical layer from cellular mMIMO, which brings 10x Spectral Efficiency (SE) improvement over legacy cellular networks [199]. This gain comes from deploying a massive number of antennas at each BS, that provide spatial multiplexing for many UEs by digital beamforming. CF mMIMO is inherently a distributed implementation of co-located mMIMO, where densely developed APs provide service for a smaller number of UEs with a coherent joint transmission and Time Division Duplexing (TDD) operation. The procedure takes place in a user-centric (as opposed to network-centric) fashion, where the UEs are surrounded and served by several APs. The APs are connected to one or multiple Central Processing Units (CPUs), i.e., edge-cloud processors or Cloud Radio Access Network (C-RAN) [210] data centers [211], by high-capacity fronthaul links where data precoding / decoding operations, synchronization, and other

network management operations take place. The acquisition of accurate Channel State Information (CSI) is critical for different CF mMIMO operations. Hence, it employs Uplink (UL) pilots to estimate the channel at the AP while eliminating the Downlink (DL) pilot training phase by considering channel reciprocity. However, due to the limited number of channel uses in each coherence interval, only a limited number of orthogonal pilots are available, typically smaller than the number of UEs. The number of available pilots is independent of the number of UEs and is limited due to the natural channel variation in the time and frequency domains [212]. Hence, reusing the same pilot for different UEs is inevitable, which introduces undesirable effects known as pilot contamination: due to the co-pilot interference among UEs, the fading channel at the APs can not be accurately estimated.

Different pilot assignment strategies have already been proposed in the literature to solve this issue. The most straightforward approach is random pilot assignment [14], where each AP independently assigns a random pilot to its associated UEs. This is a fully distributed procedure and requires a minimum degree of centralization and knowledge of the pilots of other UEs, but has the worst performance among different pilot reuse strategies. Hence, a better pilot assignment policy needs to know other UEs' (at least its neighbors) pilots to reduce the effects of pilot contamination. A greedy pilot assignment is proposed in [14], that iteratively updates the pilot of the UE with minimum rate. A structured pilot assignment scheme is proposed in [213], that maximizes the minimum distance of the co-pilot UEs. The location information of the UEs is utilized in location-based greedy pilot assignment [214] to improve the initial pilot assignment. The pilot assignment is also considered as an interference management problem with multiple groupcasting messages in [215] and then solved by topological pilot assignments where both known and unknown UE / AP connectivity patterns are considered.

Graph theory has also been used to model pilot assignment in CF mMIMO, where graph coloring [216] and weight graphic [217] schemes created and employed an interference graph to assign pilots to different UEs. The authors in [218], [219] used tabu search pilot assignment in CF mMIMO. Pilot assignment can also be considered as a graph matching problem and then solved by the Hungarian algorithm [220]. A weighted count-based pilot assignment is presented in [221], that uses the UEs prior geographic information and pilot power to maximize the pilot reuse weighted distance. A scalable pilot assignment scheme is presented in [222] to grant massive access in CF mMIMO. Another scalable pilot assignment algorithm based on deep learning is presented in [223], that uses UEs geographical locations as an input. The authors in [224] presented a pursuit learning approach for joint pilot allocation and AP association. A pilot assignment strategy based on quantum bacterial foraging optimization is proposed in [225]. The pilot assignment is also considered as a balanced diverse clustering problem in [226] and solved by a repulsive clustering approach.

The co-pilot interference, in principle, is caused by pilot reuse for similar UEs, i.e., in terms of geographical proximity and / or similar channel coefficient. Hence, an intelligent pilot assignment scheme could employ the similarity information to avoid pilot reuse for similar UEs. Motivated by this consideration, in this chapter, we consider pilot assignment as a Diverse Clustering Problem (DCP), which forms the clusters of UEs with maximized intra-cluster diversity. We then

propose a repulsive clustering and an iterative maxima search methods to solve this problem. These clusters are then used for pilot assignments.

The main contributions of this chapter are summarized as follows:

- We formulated the pilot assignment as a DCP: a clustering problem with arbitrary capacity constraints on cluster size, aiming to maximize the intra-cluster heterogeneity and inter-cluster homogeneity.
- We propose a repulsive clustering and an iterative maxima search approaches composed of a local search and weak and robust perturbation procedures to sufficiently cover the search space and balance between quality and diversity of solutions.
- We evaluate and compare the performance of the proposed approach under different situations and scenarios with respect to average and per-user UL and DL rates.

The remainder of this chapter is summarized as follows. Section 6.2 provides the system model for the CF mMIMO. We formulate the pilot assignment problem in Section 6.3 and then propose the repulsive clustering in Section 6.4 and iterative maxima search procedure in Section 6.5. The numerical results are presented in Section 6.6, and finally, Section 6.7 concludes the chapter.

6.2 System Model

We consider a typical CF mMIMO system, where K single-antenna UEs are jointly served by M geographically distributed APs each equipped with L antennas ($K \ll M$), as shown in Figure 6.1a. The APs are connected to one or multiple CPUs by unlimited and error-free fronthaul channels. The CPUs are connected through very fast optical fibers and share the information, and every time one arbitrary CPU is responsible for the pilot assignment. So, our approach is fully centralized, and the study of distributed pilot assignments is left for future work.

The channel coefficient $\mathbf{g}_{mk} \in \mathbb{C}^{L\times 1}$ between the m-th AP and the k-th UE is given as

$$\mathbf{g}_{mk} = \beta_{mk}^{1/2}\mathbf{h}_{mk}, \tag{6.1}$$

where $\{\beta_{mk}\}$ represent the Large-Scale Fading (LSF) coefficients, i.e., pathloss and shadowing, and $\{\mathbf{h}_{mk}\}$ indicate the small-scale fading coefficients which are assumed to be independent and identically distributed (i.i.d.) normal random variables $\mathcal{CN}(0, \mathbf{I}_L)$. We adopt the block fading model, shown in Figure 6.1b, where time-frequency resources are divided into coherence intervals of τ_c channel uses in which the channel can be approximately considered as static. The duration of the intervals is defined based on propagation environment, UEs mobility, and carrier frequency.

Each interval is further divided into three sub-intervals such that: $\tau_c = \tau_p + \tau_u + \tau_d$, where τ_p is used for UL pilot training, and τ_u and τ_d are used for UL and DL data transmission, respectively. We assume that $\mathbf{h}_{mk}$ stays constant during a coherence interval and is independent in different coherence intervals. We eliminate the DL pilot training phase by assuming channel reciprocity, i.e., the same channel coefficients for the UL and DL transmissions.

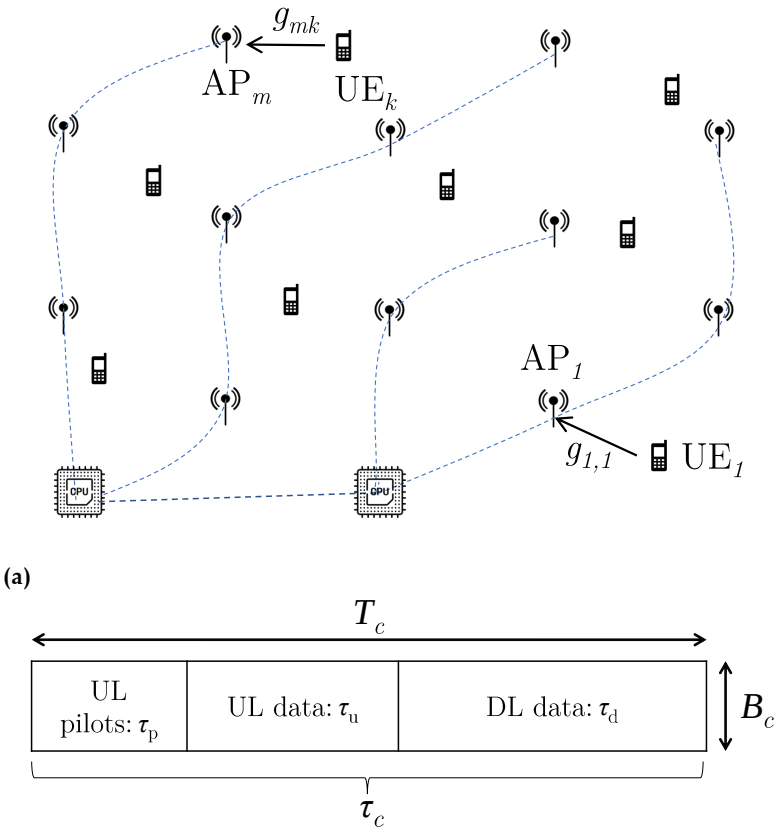

Figure 6.1: (a) A CF mMIMO system, where M distributed APs jointly serve K UEs (K $\ll$ M). (b) A coherence block with UL pilot training, and UL and DL data transmission phases.

6.2.1 Uplink Pilot Training

We assume that there are only τ_p mutually orthogonal pilot sequences with length τ_p each represented as a column $\boldsymbol{\phi} \in \mathbb{C}^{\tau_p \times 1}$ of a matrix $\boldsymbol{\Phi}$, for which we have $\|\boldsymbol{\phi}_{p_k}^H \boldsymbol{\phi}_{p_{k'}}\| = 1$ if $p_k = p_{k'}$, and $\|\boldsymbol{\phi}_{p_k}^H \boldsymbol{\phi}_{p_{k'}}\| = 0$, otherwise, and $p_k \in \{1, \ldots, \tau_p\}$ indicates the index of the pilot assigned to the kth UE.

In the UL pilot training phase, all UEs simultaneously transmit their pilots. The m-th AP receives

$$\mathbf{Y}_m^p = \sqrt{\tau_p \rho^p} \sum_{k=1}^{K} \mathbf{g}_{mk} \boldsymbol{\phi}_{p_k}^H + \mathbf{W}_m^p, \tag{6.2}$$

where ρ^p is the normalized Signal-to-Noise Ratio (SNR) of a pilot sequence with respect to the noise power, and $\mathbf{W}_m^p$ is the $L \times \tau_c$ additive noise matrix with elements following i.i.d. $\sim \mathcal{CN}(0,1)$ random variables.

As shown in [14], [227], the effective channel coefficients between UE k and AP m can be estimated employing the Minimum Mean Square Error (MMSE) estimator after projecting $\mathbf{Y}_m^p$ onto $\boldsymbol{\phi}_k^H$ as

$$\hat{\mathbf{g}}_{mk} = \mathbb{E}\left\{\mathbf{g}_{mk}\check{\mathbf{y}}_{mk}^{pH}\right\}\left(\mathbb{E}\left\{\check{\mathbf{y}}_{mk}^{p}\check{\mathbf{y}}_{mk}^{pH}\right\}\right)^{-1}\check{\mathbf{y}}_{mk}^{p} = c_{mk}\check{\mathbf{y}}_{mk}^{p}, \tag{6.3}$$

where $\check{\mathbf{y}}_{mk}^{p} \triangleq \mathbf{Y}_m^p\boldsymbol{\phi}_{p_k}$, and

$$c_{mk} \triangleq \frac{\sqrt{\tau_p\rho^p}\beta_{mk}}{\tau_p\rho^p\sum_{k'=1}^{K}\beta_{mk'}\left|\boldsymbol{\phi}_{p_k}^H\boldsymbol{\phi}_{p_{k'}}\right|^2+1}. \tag{6.4}$$

The l-th component's mean-square of the estimated channel vector $\hat{\mathbf{g}}_{mk}$ can be calculated as

$$\gamma_{mk} \triangleq \mathbb{E}\left\{\left|[\hat{\mathbf{g}}_{mk}]_l\right|^2\right\} = \sqrt{\tau_p\rho^p}\beta_{mk}c_{mk}. \tag{6.5}$$

6.2.2 Uplink Data Transmission

In CF mMIMO, all APs and UEs share the same time-frequency resources for data transmission. In the UL, all UEs simultaneously transmit their data to the APs. The AP m receives

$$\mathbf{y}_m^u = \sqrt{\rho^u}\sum_{k=1}^{K}\mathbf{g}_{mk}\sqrt{\eta_k}q_k + \mathbf{w}_m^u, \tag{6.6}$$

where q_k is the signal transmitted by UE k with power $\mathbb{E}\left\{|q_k|^2\right\} = 1$, $\eta_k \in [0,1]$ shows the power control coefficient, ρ^u indicates the normalized UL SNR and $w_m^u \sim \mathcal{CN}(0,1)$ is the additive noise at the receiver.

The Mixed Reality (MR) combining scheme can be applied to decode the desired signal for a certain UE k. AP m sends $\hat{\mathbf{g}}_{mk}^*\mathbf{y}_m^u$ to the CPU for data detection. The CPU combines all the received signals for UE k as

$$r_k^u = \sum_{m=1}^{M}\sum_{l=1}^{L}[\hat{\mathbf{g}}_{mk}]_l^*[\mathbf{y}_m^u]_l. \tag{6.7}$$

Following the same procedure as in [14], the signal then can be decomposed at the CPU as

$$\begin{aligned} r_k^u = & \underbrace{\sqrt{\rho^u \eta_k} q_k \mathbb{E}\left\{\sum_{m=1}^{M}\sum_{l=1}^{L} [\hat{g}_{mk}]_l^* [g_{mk}]_l\right\}}_{DS_k} \\ & + \underbrace{\sqrt{\rho^u \eta_k} q_k \left(\sum_{m=1}^{M}\sum_{l=1}^{L} [\hat{g}_{mk}]_l^* [g_{mk}]_l - \mathbb{E}\left\{\sum_{m=1}^{M}\sum_{l=1}^{L} [\hat{g}_{mk}]_l^* [g_{mk}]_l\right\}\right)}_{BU_k} \\ & + \underbrace{\sqrt{\rho^u} \sum_{m=1}^{M}\sum_{k'\neq k}^{K}\sum_{l=1}^{L} \sqrt{\eta_{k'}} [\hat{g}_{mk}]_l^* [g_{mk'}]_l q_{k'}}_{CPI_k} + \sum_{m=1}^{M}\sum_{l=1}^{L} [\hat{g}_{mk}]_l^* [w_m^u]_l , \end{aligned} \tag{6.8}$$

where DS_k, BU_k and CPI_k denoted the desired signal (DS), beamforming uncertainty (BU) and co-pilot interference (CPI), respectively.

The UL achievable rate for UE k can be calculated as

$$R_k^u = \log_2\left(1 + \frac{L^2 \rho^u \eta_k \left(\sum_{m=1}^{M} \gamma_{mk}\right)^2}{L^2 \rho^u \sum_{k'\neq k}^{K} \eta_{k'} \left(\sum_{m=1}^{M} \gamma_{mk} \frac{\beta_{mk'}}{\beta_{mk}}\right)^2 \left|\boldsymbol{\phi}_{p_k}^H \boldsymbol{\phi}_{p_{k'}}\right| + L\rho^u \sum_{k'=1}^{K} \eta_{k'} \sum_{m=1}^{M} \gamma_{mk} \beta_{mk'} + L \sum_{m=1}^{M} \gamma_{mk}}\right). \tag{6.9}$$

6.2.3 Downlink Data Transmission

In DL, APs receive encoded data from their CPUs and carry out the transmit precoding, based on the local CSI. The kth UE receives signal

$$r_k^d = \sqrt{\rho^d} \sum_{m=1}^{M}\sum_{k'=1}^{K} \eta_{mk'}^{1/2} g_{mk}^T \hat{g}_{mk'}^* q_{k'} + w_k^d, \tag{6.10}$$

where ρ^d is the normalized UL SNR, and $w_k^d \sim \mathcal{CN}(0,1)$ is the additive noise at the kth UE. Then q_k will be detected from r_k^d.

Employing a similar methodology as in the UL, the achievable DL rate for the kth UE can be derived from

$$R_k^d = \log_2\left(1 + \frac{L^2 \rho^d \left(\sum_{m=1}^{M} \eta_{mk}^{1/2} \gamma_{mk}\right)^2}{\rho^d \sum_{k'\neq k}^{K} \left(\sum_{m=1}^{M} \eta_{mk'}^{1/2} \gamma_{mk'} \frac{\beta_{mk}}{\beta_{mk'}}\right)^2 \left|\boldsymbol{\phi}_{k'}^H \boldsymbol{\phi}_k\right|^2 + L\rho^d \sum_{k'=1}^{K} \sum_{m=1}^{M} \eta_{mk'} \gamma_{mk'} \beta_{mk} + 1}\right). \tag{6.11}$$

6.3 Pilot Assignment in CF mMIMO

6.3.1 Problem formulation

The goal of the UL pilot training phase is to increase the number of effectively estimated channels or to improve the quality of the UL channel estimation, which can be interpreted as a UL rate maximization problem. So, an efficient pilot reuse scheme should assign pilots to UEs so that the sum of the UL rates is maximized. Mathematically the pilot reuse problem in CF mMIMO can be formulated as

$$\max_{\mathbf{p}} \quad \sum_{k=1}^{K} R_k^u \tag{6.12a}$$

s.t.

$$\mathbf{p} = [p_1, \ldots, p_K]^T, \tag{6.12b}$$

$$\boldsymbol{\phi}_{p_k} = \mathrm{col}_{p_k}(\boldsymbol{\Phi}), \tag{6.12c}$$

$$p_k \in \{1, \ldots, \tau_p\}, \tag{6.12d}$$

where the $\mathbf{p}$ is the pilot assignment vector and $\mathrm{col}_i(\boldsymbol{\Phi})$ indicates the ith column of matrix $\boldsymbol{\Phi}$.

The co-pilot interference originated from reusing the same pilot for similar UEs, i.e., geographical closeness, common serving APs, and similar channel coefficients. So, an intelligent pilot assignment scheme should consider the similarity among the UEs and reuse the same pilot $\boldsymbol{\phi}$ in UEs that have higher dissimilarities, i.e., geographically far apart or with fewer common serving APs. We hence formulate the pilot assignment in CF mMIMO as a diverse clustering problem, where we form τ_p (number of available orthogonal pilots) clusters in such a way that UEs belonging to the same cluster have a high "dissimilarity" or "diversity". In the following subsection, we formulate and discuss the problem.

6.3.2 Diverse Clustering Problem

The DCP consists of the assigning of a set of K elements, i.e., UEs, into τ_p mutually disjoint subsets or clusters, i.e., pilots, while the diversity among the elements in each subset, i.e., intra-cluster diversity, and inter-cluster similarity is maximized. The inter-cluster diversity is calculated as the sum of the individual distances between each pair of elements in clusters, where the concept of distance depends on the specific application context. The objective is to maximize the overall diversity, i.e., the sum of the diversity of all subsets. From the graph theory perspective, DCP can be considered as partitioning the vertices of a complete weighted undirected graph into τ_p subgraphs in such a way that the total weight of the subgraphs is maximized while applying optional constraints on the number of nodes in each subgraph.

An illustration of DCP and of the conventional clustering problem is presented in Figure 6.2 for a small configuration with four data points and two clusters. Figure 6.2a shows a conventional

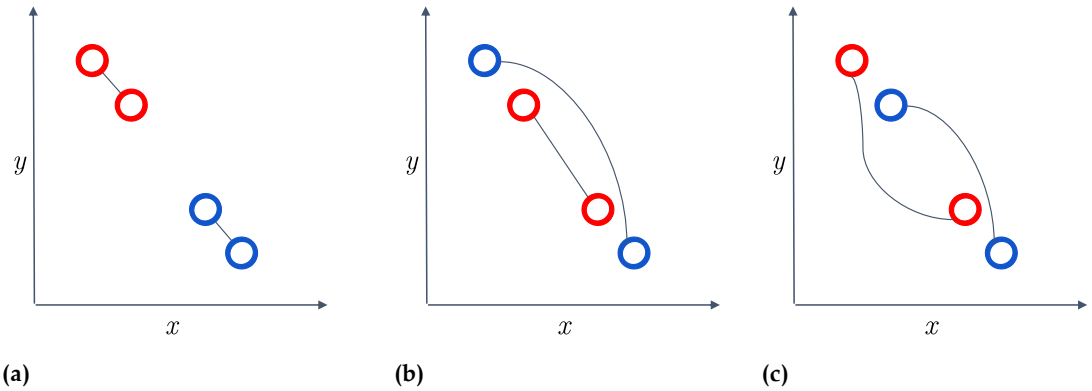

Figure 6.2: Illustrated example and comparison of the conventional clustering (a), and feasible (b) and optimal (c) solutions for diverse clustering, with four data points and two clusters.

clustering problem, where clusters are formed in such a way to minimize inter-cluster similarity (intra-cluster diversity).

In contrast, Figure 6.2b-c show two DCPs, where data points with higher dissimilarities are joining the same cluster. Figure 6.2b represents a feasible solution for DCP, in which the diversity score of one cluster (blue data points) is relatively higher than the other, while in the optimal solution, all clusters should have relatively similar diversity score, as it is the case in Figure 6.2c.

In general DCP can be considered as a capacitated clustering [228], [229] or maximally diverse grouping problem [230], [231] and then formulated as a quadratic integer program as

$$\max_{\mathbf{X}} \quad \sum_{p=1}^{\tau_p} \sum_{k=1}^{K-1} \sum_{k\prime=k+1}^{K} x_{k,p} x_{k',p} d_{k,k'} \tag{6.13a}$$

s.t.

$$\sum_{p=1}^{\tau_p} x_{k,p} = 1, \qquad k = 1, \ldots, K, \tag{6.13b}$$

$$L_k \leq \sum_{k=1}^{K} x_{k,p} \leq U_k, \qquad p = 1, \ldots, \tau_p, \tag{6.13c}$$

$$x_{k,p} \in \{0,1\}, \quad k = 1, \ldots, K, p = 1, \ldots, \tau_p, \tag{6.13d}$$

where $\mathbf{X} \in \{0,1\}^{K \times \tau_p}$ is a binary association matrix, and $x_{k,p} = 1$ if element (UE) k belongs to cluster (pilot) p, and $x_{k,p} = 0$ otherwise. $d_{k,k'}$ is the diversity measure between k and k′ elements, and L_b and U_b show the minimum and maximum size of each set, respectively. The constraint (6.13b) guarantees that each element is assigned to only one cluster, and (6.13c) forces the size of the clusters to be in the specified range. The diversity measure can be a predefined distance function, i.e., Euclidean distance and cosine similarity, or can be defined as a parameterized kernel and then learned by, e.g., neural networks.

This formulation favors forming fewer large-size clusters against many small-size clusters. Considering the full interference among the nodes in each cluster (orthogonal pilot), in the pilot reuse problem, fewer large-size clusters increase the co-pilot interference among the co-cluster UEs. So we multiply a regularization term by the objective of the optimization problem to penalize the large-size clusters by dividing their score by the size of clusters. This will avoid wasteful growth of the size of some clusters. Adding a new node to a N-size cluster is interpreted as interference with all N nodes and penalized. Hence, the new formulation will be

$$\begin{aligned} &\max_{\mathbf{x}} \quad \sum_{p=1}^{\tau_p} \frac{1}{|\mathcal{C}_p|} \sum_{k=1}^{K-1} \sum_{k\prime=k+1}^{K} x_{k,p} x_{k\prime,p} d_{k,k\prime} \\ &\text{s.t.} \\ &(6.13b) - (6.13d) \end{aligned} \tag{6.14}$$

where $\mathcal{C}_p$ is the cluster set p, and $|\cdot|$ shows the size of a set.

DCP is a combinatorial optimization problem and is proved to be NP-hard [232]. Typically finding the exact solution for these problems is not computationally possible, at least when K is large.

DCP has already been investigated in the literature under different names, such as maximally diverse grouping problem [230] and anticlustering [233], [234]. Several algorithms have already been proposed to solve DCP, including tabu search with strategic oscillation [235], genetic algorithm [236], [237], artificial bee colony [238], variable neighborhood search [231]. In this chapter, we propose repulsive scheme and an iterative maxima search method, adopted from [239], for pilot reuse in CF mMIMO based on DCP problem.

6.4 Repulsive Clustering for Pilot Assignment

Repulsive clustering is a simple iterative algorithm that directly maximizes (6.13a), assuming a stringent constraint on the size of clusters, forcing the algorithm to form balanced clusters. This algorithm first randomly assigns data points to different clusters and then iteratively swaps the UEs among clusters as long as it improves the overall repulsion score.

6.5 Iterative Maxima Search for Pilot Reuse

The proposed approach employs an iterative maxima search procedure that integrates a local neighborhood search procedure with a weak perturbation operator to improve the intensity or quality of solutions and a robust perturbation operator to improve the diversity of the solutions by moving the search to a distant region to avoid local optimum solutions. Before going to the details of the proposed scheme, some concepts need to be defined.

Algorithm 6.1 A Heuristic Algorithm for Repulsive Clustering

Input: Number of clusters (pilots) τ_p, Set of UEs $\mathcal{K}$
Output: Pilot assignment vector $\mathbf{p}$

```
Randomly divide 𝒦 UEs into τ_p equal-sized clusters 𝒞,
while Performance is improving do
    for C1, C2 ∈ 𝒞 do
        for u ∈ C1 and w ∈ C2 do
            if exchanging clusters of u and w increases the overall diversity measure then
                Swap the clusters of u and w,
            end if
        end for
    end for
end while
for p = 1 : τ_p do
    Assign pilot φ_p to UEs in cluster p
end for
```

Definition of neighborhoods

We define two different types of neighborhood: OneMove (N_1) neighborhood and SwapMove (N_2) neighborhood. Given the pilot assignment vector $\mathbf{p}^*$, N_1 returns all possible solutions obtained by changing the assigned pilot of a single UE (OneMove) in such a way that the pilot reuse capacity constraints are satisfied, while N_2 returns the possible solutions obtained by exchanging the pilots of a pair of UEs (SwapMove).

M matrix

To improve the computational efficiency of the local search procedure, we employ a $K \times \tau_p$ matrix $\mathbf{M}$, where $m_{k,p} \in \mathbf{M}$ shows the sum of diversity between UE k and all UEs with pilot index p, and having the pilot assignment vector $\mathbf{p}$, calculates as $m_{k,p} = \sum_{\substack{k,k'=1,\\ p_{k'}=p}}^{K} d_{k,k'}$. Calculation of this matrix can be done in order of $\mathcal{O}(K^2)$.

Definition of a solution

The tuple $< \mathbf{p}, \mathbf{c}, \mathbf{s} >$ refers to a solution in search space, where $\mathbf{c}$ is a vector that saves the diversity index of each cluster, and $\mathbf{s}$ is a vector that stores the size of each cluster for a given solution. Basically, for each solution in the search space, we save and update the tuple where the two last elements are used to speed up the search procedure, as we will discuss later.

The overall procedure is presented in Algorithm 6.2. The algorithm starts by generating I_s random initial feasible solutions (Algorithm 6.3), followed by a local neighborhood search procedure (Algorithm 6.4). The best solution among the initial solutions is then saved for later use. It then repeats a maxima search procedure (lines 9-20) followed by a robust perturbation procedure until

*The pilot assignment vector $\mathbf{p}$ is equivalent to the association matrix $\mathbf{X}$ in (6.13a), and in fact, $\mathbf{X}$ is the one-hot encoding version of $\mathbf{p}$.

Algorithm 6.2 Iterative Maxima Search for Pilot Reuse

Input: I_s, t_{max}, α
Output: Pilot assignment vector $\mathbf{p}^*$

1: Initialize empty set $\mathcal{P}_0$
2: **for** $i = 1$ **to** I_s **do**
3: Generate initial solution $\mathbf{p}^0$ employing Algorithm 6.3.
4: Update $\mathbf{p}^0$ employing the local search in Algorithm 6.4.
5: Add $\mathbf{p}^0$ to $\mathcal{P}_0$.
6: **end for**
7: Get the best solution from $\mathcal{P}_0$ and save it in $\mathbf{p}$
8: $\mathbf{p}^* \leftarrow \mathbf{p}$
9: **while** Time() $\leq t_{max}$ **do**
10: Set ctr $\leftarrow 0$
11: **while** ctr $< \alpha$ **do**
12: Apply weak perturbation operator in Algorithm 6.5 on $\mathbf{p}$.
13: Update $\mathbf{p}$ employing local search Algorithm 6.4.
14: **if** $f(\mathbf{p}) > f(\mathbf{p}^*)$ **then**
15: $\mathbf{p}^* \leftarrow \mathbf{p}$
16: Reset ctr $\leftarrow 0$
17: **else**
18: Increase ctr $\leftarrow$ ctr $+ 1$
19: **end if**
20: **end while**
21: Update $\mathbf{p}$ employing the robust perturbation in Algorithm 6.6.
22: **end while**
23: Return $\mathbf{p}^*$

a certain time budget is exceeded. This iterative maxima search procedure is composed of a weak perturbation procedure (Algorithm 6.5) followed by a local search procedure (Algorithm 6.4), which will be discussed in the following subsections. In each iteration, after employing the weak perturbation and local search procedures, the quality or fitness of the current solution $\mathbf{p}$ ($f(\mathbf{p})$) is compared and used to replace the incumbent solution $\mathbf{p}^*$ in case of improvement (lines 14-19). The fitness of a solution is calculated as:

$$f(\mathbf{p}) = \sum_{p=1}^{\tau_p} \frac{1}{|\mathcal{C}_p|} \sum_{\substack{p_k = p_{k'}, \\ k<k'}} d_{kk'}, \tag{6.15}$$

where, $d_{kk'}$ represents the diversity among k and k′ UEs. This fitness function basically is a weighted average of the diversity score of different clusters, where the weight is the inverse of the cluster size.

6.5.1 Initial Feasible Solution

The Initial feasible solution procedure is presented in Algorithm 6.3. The procedure starts by randomly assigning each pilot to L_b UEs and then for the remaining UEs assigns a random pilot

Algorithm 6.3 Initial Feasible Solution

Input: Set of Pilots $\mathcal{P}$, Set of UEs $\mathcal{K}$, L_b, U_b
Output: Initial Pilot Assignment Vector **p**

1: **for** $p \in \mathcal{P}$ **do**
2: Randomly select L_b UEs from $\mathcal{K}$ and name it $\mathcal{K}'$
3: Assign pilot p to UEs in $\mathcal{K}'$ and update $\mathcal{K} = \mathcal{K} \setminus \mathcal{K}'$
4: **end for**
5: **while** $\mathcal{K} \neq \emptyset$ **do**
6: Get $k \in \mathcal{K}$ and randomly select pilot $p \in \mathcal{P}$
7: **if** $|\mathcal{C}|_p < U_b$ **then**
8: Assign pilot p to k and update $\mathcal{K} = \mathcal{K} \setminus \{k\}$
9: **end if**
10: **end while**
11: Return assignment vector **p**.

p while being sure that the number of UEs with pilot p, $|\mathcal{C}_p|$, is less than an upper bound U_b. The complexity of this algorithm is $\mathcal{O}(K + \tau_p)$.

6.5.2 Local Neighborhood Search

The local neighborhood search procedure is presented in Algorithm 6.4. Given the current assignment **p**, the procedure probes $N_1(\mathbf{p})$ (lines 3-11) and $N_2(\mathbf{p})$ (lines 12-19) neighborhoods and iteratively updates the incumbent solution with the better neighbor solution. The procedure repeats until the incumbent solution finds the local optimum and can not be further improved. Given a solution $< \mathbf{p}, \mathbf{c}, \mathbf{s} >$, the fitness of a neighbor solution can be easily computed using the defined above matrix **M**. For N_1 neighbors, changing the pilot index of UE k from i to j does not change the diversity values of the UEs, except those with pilot index i and j. Here the value of a OneMove can be determined by

$$\Delta f = \frac{c_j + m_{kj}}{s_j + 1} - \frac{c_j}{s_j} + \frac{c_i - m_{ki}}{s_i - 1} - \frac{c_i}{s_i}, \tag{6.16}$$

where $m_{k,i}$ and $m_{k,j}$ are the entries of matrix **M** and c, and s are the elements of vectors **c** and **s**, respectively.

Also for N_2 neighbors, the value of a SwapMove (exchanging the pilot index of UEs k and k′) is determined by

$$\Delta f = (m_{k,p_{k'}} - m_{k,p_k}) + (m_{k',p_k} - m_{k',p_{k'}}) - 2d_{kk'}. \tag{6.17}$$

6.5.3 Weak and robust perturbation

The weak and robust perturbation procedures are presented in Algorithm 6.5 and Algorithm 6.6, respectively. The weak perturbation operator aims to jump out of the current local optimum within the iterative search procedure by applying some assignment deterioration. The strength of

Algorithm 6.4 Local Search Procedure

Input: Set of Pilots $\mathcal{P}$, Set of UEs $\mathcal{K}$, $\mathbf{p}$, L_b, U_b
Output: Local optimum assignment $\mathbf{p}^*$

1: $\mathbf{p}^* \leftarrow \mathbf{p}$
2: Initialize $\mathbf{M} \in \mathbb{R}^{K \times \tau_p}$
3: **while** solution improves **do**
4: **for** $k \in \mathcal{K} \wedge p \in \mathcal{P}$ **do**
5: **if** $(p_k^* \neq p) \wedge (\mathcal{C}_{p_k^*} > L_b) \wedge (\mathcal{C}_p < U_b)$ **then**
6: Calculate Δf by (6.16)
7: **if** $\Delta > 0$ **then**
8: Set $p_k^* \leftarrow p$ and update $\mathbf{M}$
9: **end if**
10: **end if**
11: **end for**
12: **for** $k, k' \in \mathcal{K} \wedge k' > k$ **do**
13: **if** $p_k^* \neq p_{k'}^*$ **then**
14: Calculate Δf by (6.17)
15: **if** $\Delta f > 0$ **then**
16: Swap the pilots of k and k' and update $\mathbf{M}$
17: **end if**
18: **end if**
19: **end for**
20: **end while**
21: Return $\mathbf{p}^*$

the weak perturbation is controlled by η_w, representing the number of random neighbor solutions to be checked by this operator. For each perturbation step, the best solution among η_{w2} randomly selected neighbors is compared, and the incumbent solution is replaced in case of improvement (lines 3-7). This incumbent solution is used for the next iteration of perturbation. The large values of η_{w2} cause less deterioration of the current sample and can be set to K to adjust the problem size.

The weak perturbation helps the search procedure discover the neighborhood of the current area better, while it is still possible that the search is trapped in a deep local optimum that weak perturbation can not jump out of. The robust perturbation procedure consequently performs η_s moves regardless of their values. η_s controls the strength of the robust perturbation and is empirically set to $\eta_s = \theta \times \frac{K}{\tau_p}$, from [239], where θ is chosen from $\{1, 1.5\}$.

6.6 Numerical results

6.6.1 Simulation setup

Let us consider M APs with L antennas and K single antenna UEs that are independently and uniformly distributed in a 1×1 km^2 square area. The wraparound technique is adopted to mitigate the network edge and boundary effects and to model the network as if operating over an unlimited area. The large-scale fading coefficient β_{mk} in (6.1) is calculated by $\beta_{mk} = PL_{mk} \cdot 10^{\sigma_{sh} z_{mk}}/10$,

Algorithm 6.5 Weak Perturbation

Input: Pilot assignment vector $\mathbf{p}$, η_w, $\eta_w 2$
Output: Perturbed assignment $\mathbf{p}$

for $i = 1$ **to** η_w **do**
  Randomly select a neighbor solution $\mathbf{p}' \in N_1(\mathbf{p}) \cup N_2(\mathbf{p})$
  for $j = 1$ **to** η_{w2} **do**
    Randomly select a neighbor solution $\mathbf{p}'' \in N_1(\mathbf{p}) \cup N_2(\mathbf{p})$
    if $f(\mathbf{p}'') > f(\mathbf{p}')$ **then**
      $\mathbf{p}' \leftarrow \mathbf{p}''$
    end if
  end for
  $\mathbf{p} \leftarrow \mathbf{p}'$
end for
Return assignment vector $\mathbf{p}$.

Algorithm 6.6 Robust Perturbation

Input: Pilot assignment vector $\mathbf{p}$, η_s
Output: Perturbed assignment $\mathbf{p}$

for $i = 1$ **to** η_w **do**
  Randomly select a neighbor solutions $\mathbf{p}' \in N_1(\mathbf{p}) \cup N_2(\mathbf{p})$
  $\mathbf{p} \leftarrow \mathbf{p}'$
end for
Return assignment vector $\mathbf{p}$.

where $10^{\sigma_{sh} z_{mk}}/10$ represents the shadow fading with standard deviation σ_{sh} and $z_{mk} \sim \mathcal{N}(0,1)$ and PL_{mk} represents the pathloss from UE k to AP m. In this chapter, we use the three-slope path loss model presented in [14] as

$$PL_{mk} = \begin{cases} -L - 15\log_{10}(d_1) - 20\log_{10}(d_0), \text{ if } d_{mk} \leq d_0 \\ -L - 15\log_{10}(d_1) - 20\log_{10}(d_{mk}) \\ \text{ if } d_0 < d_{mk} \leq d_1 \\ -L - 35\log_{10}(d_{mk}), \text{ if } d_{mk} > d_1 \end{cases} \tag{6.18}$$

where d_{mk} indicates the distance between AP m and UE k, d_0 and d_1 are the distance thresholds, and L is given by

$$\begin{aligned} L \triangleq \; & 46.3 + 33.9\log_{10}(f) - 13.82\log_{10}(h_{AP}) \\ & - \left(1.1\log_{10}(f) - 0.7\right) h_u + \left(1.56\log_{10}(f) - 0.8\right), \end{aligned} \tag{6.19}$$

where f (MHz) is the carrier frequency, and h_u (m) and h_{AP} (m) indicate the UE and AP height respectively.

Noise power is calculated by $P_n = Bk_B T_0 W$, where B is the bandwidth, k_B denotes the Boltzmann constant, T_0 is the noise temperature and W represents the noise figure. The transmission powers of the uplink pilot and the uplink data and downlink data are set to $\rho^p = 100$ (mW),

Table 6.1: Simulation setup.

Parameter	Value	Definition
B	20 MHz	Bandwidth
h_u	1.65 m	UE height
h_{AP}	15 m	AP height
d_0, d_1	10 m, 50 m	Path loss distance thresholds
k_B	1.381×10^{-23} (Joule per Kelvin)	Boltzmann constant
T_0	290 (Kelvin)	Noise temperature
W	9	Noise figure
ρ^p	100 mW	Pilot transmission power
ρ^u	100 mW	Uplink transmission power
ρ^d	200 mW	Downlink transmission power

$\rho^u = 100$ (mW), and $\rho^d = 200$ (mW), respectively. The channel estimation overhead has been taken into account in defining the per-user uplink throughput as $T_k^u = B\frac{1-\tau_p/\tau_c}{2}\log_2(1+\mathrm{SINR}_k^u)$, where $\tau_c = 200$ samples. The $1/2$ in the above equation is due to the co-existence of the uplink and downlink traffic. We also employed max-min power control [14] to further improve the sum throughput.

In this chapter we consider the Euclidean distance for the diversity measure as

$$d_{k,k'} = \sqrt{\sum_{i=1}^{|F|}(U_k[i] - U_{k'}[i])^2}, \tag{6.20}$$

where F is the feature set (e.g., geographical coordinates) of the UEs. The definition and analysis of more sophisticated repulsive functions are left for future work.

6.6.2 Result and discussion

This section compares the result of the proposed Iterative Maxima Search (IMS) scheme against different pilot assignment strategies. In particular, the random and greedy pilot assignments from [14], the repulsive clustering [226] and the Ideal solution are chosen for evaluation. The ideal solution represents the unreachable upper bound, where there is no pilot contamination (i.e., $\mathrm{CPI}_k = 0$ in (6.8)) and the channels can be perfectly estimated only having one single pilot. Two different variants of our algorithm are considered: equal size (ES) clusters and variable size (VS) clusters. The former keeps $L_b = U_b$, while the latter does not have such constraint, and the algorithm can form clusters of any size.

Figure 6.3 shows the per-user throughput Cumulative Distribution Function (CDF) of different pilot reuse policies for the small-scale scenario for the sake of comparison with the exhaustive search. (As the complexity of exhaustive search grows exponentially with the number of UEs, calculating its performance for large M is not possible.) The figure shows that the proposed method outperforms other approaches both in UL and DL and works almost as well as the optimal pilot reuse obtained by exhaustive search, but with far less complexity.

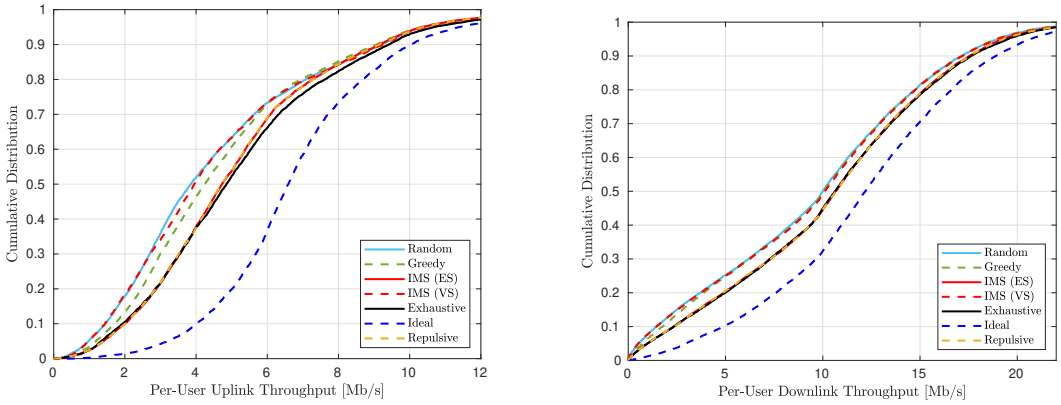

Figure 6.3: Cumulative distribution of the per-user uplink and downlink throughput for different pilot assignment strategies for a small-scale scenario, M = 50, K = 12, L = 1, and $\tau_p = 3$.

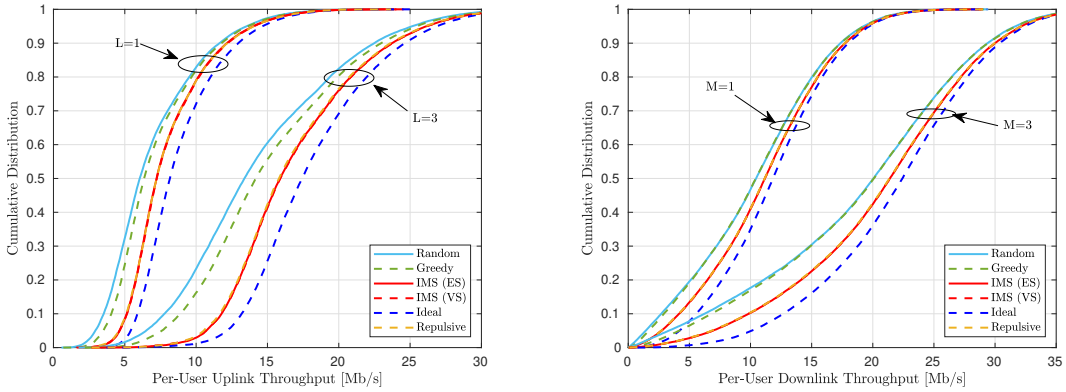

Figure 6.4: Cumulative distribution of the per-user uplink and downlink throughput for different pilot assignment strategies, K = 40, $\tau_p = 10$, and M = 200.

Table 6.2: 95th percentile of per-user uplink and downlink throughput for different values of L, when K = 40, $\tau_p = 10$, and M = 200.

Approach	UL		DL	
	L=1	L=3	L=1	L=3
Random	2.93	6.49	1.43	3.31
Greedy	3.49	7.59	1.68	4.16
Repulsive	4.59	10.52	2.69	6.80
IMS (ES)	4.62	10.71	2.73	6.90
IMS (VS)	4.63	10.68	2.72	6.88
Ideal	5.40	12.20	4.18	10.09

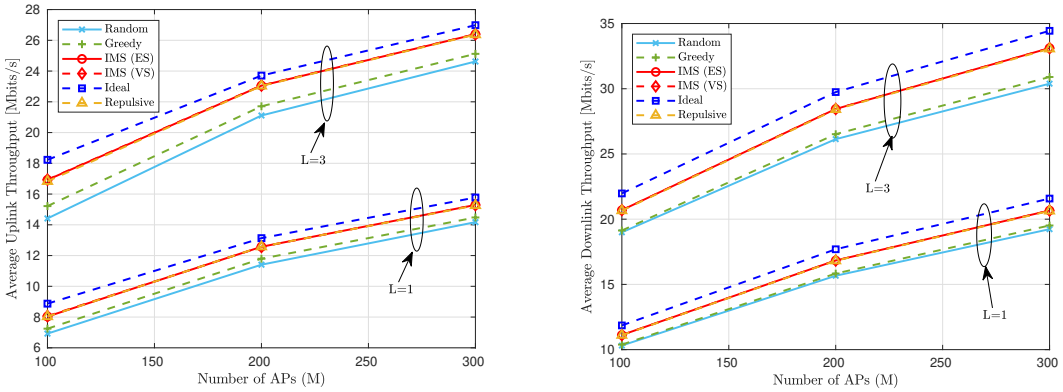

Figure 6.5: Average uplink and downlink throughput for different pilot assignment strategies, K $=$ 40, $\tau_{\mathrm{p}} = 10$.

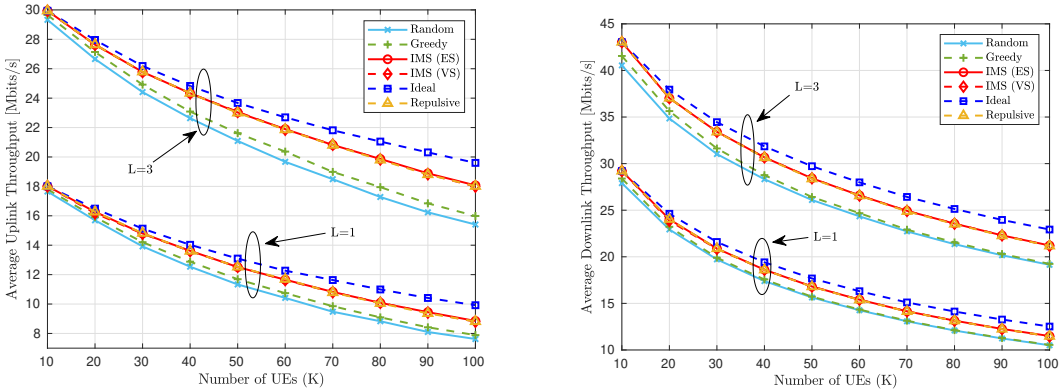

Figure 6.6: Average uplink throughput for different numbers of UEs, M $=$ 100 and $\tau_{\mathrm{p}} = 10$.

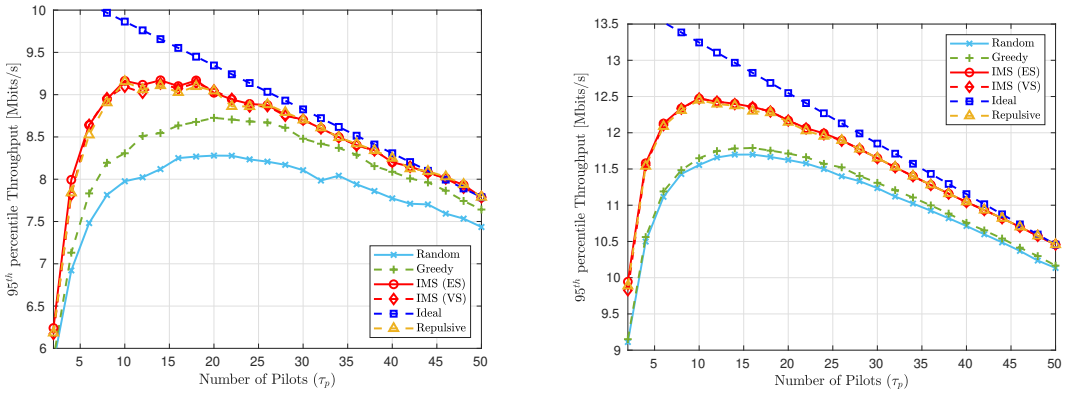

Figure 6.7: Average the per-user uplink and downlink throughput for different numbers of orthogonal pilots, M = 100, L = 1, and K = 50.

The cumulative distribution of the per-user uplink and downlink throughput of different pilot assignment strategies for different numbers of antennas L is shown in Figure 6.4. The superiority of the proposed scheme against other approaches is evident from the figure. It can also be seen from the figure that increasing the number of antennas per AP will increase the rate in all schemes while the gap between the proposed scheme and other algorithms also increases, which is reasonable as our scheme generates less co-pilot interference by properly utilizing the available resources.

Table 6.2 shows the 95th percentile of the per-user throughput extracted from Figure 6.4, where it can be seen that increasing the number of APs' antennas from L = 1 to L = 3 increases the 95th percentile by 2.3x for uplink and 2.5x for downlink. Compared to other schemes, our approach performs slightly better than repulsive clustering, but it improves the 95th percentile rate by 1.13 Mbps ($\approx 32\%$) in uplink and 1.05 Mbps ($\approx 62\%$) in downlink over a greedy pilot assignment scheme, when L = 1. These values for L = 3 are 3.12 Mbps ($\approx 38\%$) and 2.74 Mbps ($\approx 65\%$).

Figure 6.5 compares the average uplink and downlink throughput against different numbers of APs for different pilot reuse schemes. By increasing the number of APs, the average throughput increases in both uplink and downlink. Also, the performance of the multiple-antenna APs is always better than that of single-antenna APs. For example, having 100 APs with three antennas (300 antennas in total) performs better than 300 single-antenna APs. This comes from the fact that increasing L makes the channel more favorable [240] and reduces inter-user interference. It also increases the array gain, which has already been discussed and analyzed in **mai2018cell**.

The average uplink and downlink throughput of different pilot assignment schemes against the number of UEs is illustrated in Figure 6.6. It can be seen from the figure that increasing the number of UEs in the network, while the number of APs is fixed, will decrease the average throughput. The throughput reduction ratio is different for the pilot assignment policies, and in our approach it is lower than in the random and greedy schemes. This shows the reliability of our approach in large-scale scenarios.

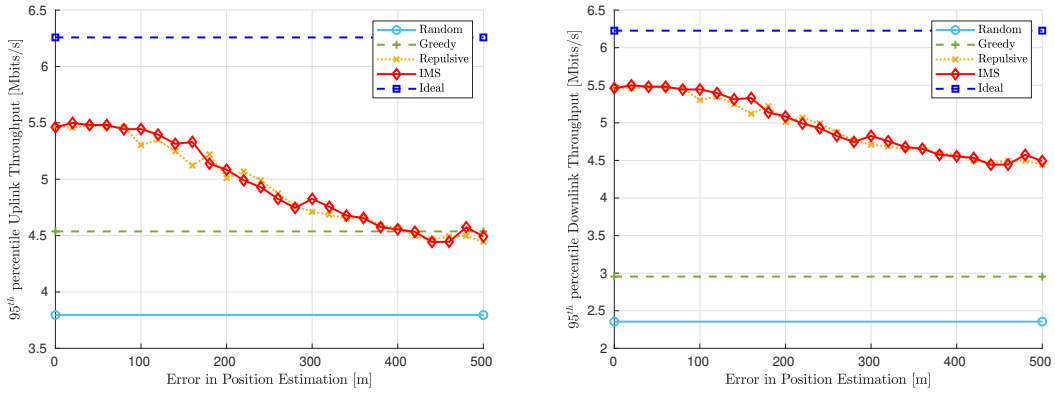

Figure 6.8: Average uplink and downlink throughput for different values of error in location estimation, M = 120, K = 50, K = 10, and L = 1.

Figure 6.7 presents the average uplink and downlink throughput with respect to the number of orthogonal pilots (τ_p) for different pilot assignment schemes, while the size of the coherence block is fixed. An interesting fact that can be seen in the figures is that increasing the number of pilots increases the performance only up to a certain point, after which the performance starts decreasing. This shows the necessity of finding the optimal number of pilots, which is outside this chapter's scope and is left for future research.

Figure 6.8 shows the 95th percentile rate of the proposed schemes in the presence of errors in the UEs locations estimation. As seen in the figure, the proposed algorithms, until a certain level, are robust against errors, and the system performance is not affected much when the error in the location estimation is less than 100 meters. Even after that, the rate is higher than in random and greedy schemes.

Figure 6.9 shows the uplink and downlink throughput for UEs when the CSI (LSF) and/or UE's locations are considered as input features in our clustering algorithm. The figure shows that both features provide relatively similar results, so each can be used as input when the other feature's data is unavailable. It can also be seen that combining both features does not provide better solutions, and considering only one feature space is enough.

6.7 Conclusion

CF mMIMO will be an essential part of future wireless communication systems, given its capability of providing uniform service for the UEs. The performance of these systems can still be further improved before it becomes a functional and operational technology. Pilot contamination is recognized as an undesirable effect that can highly degrade the performance of CF mMIMO when the UEs share the same pilot. In this chapter, we formulated pilot assignment in CF mMIMO systems as a DCP problem and proposed a repulsive and an iterative maxima search approach to solve

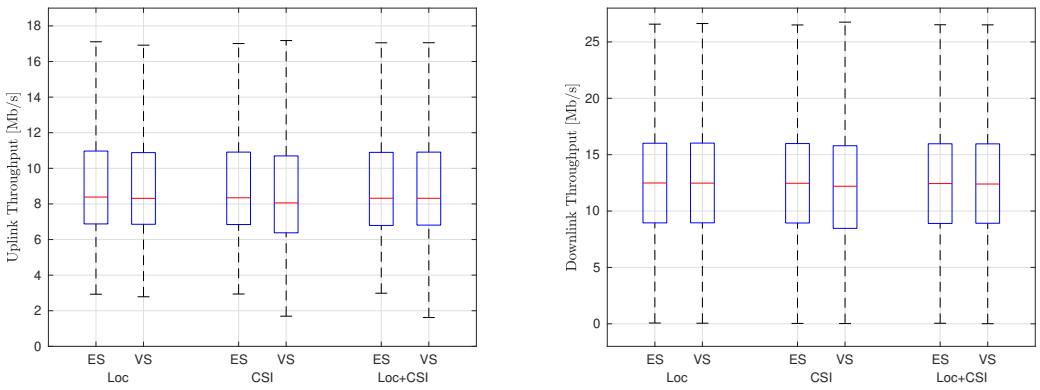

Figure 6.9: Uplink and downlink throughput when location and / or CSI is used as input feature for clustering.

it. Numerical results show the proposed scheme's effectiveness compared to other approaches from the literature. In future works, we will expand our approach by replacing the Euclidean distance with more sophisticated and parameterized diversity functions, i.e., Deep Neural Networks (DNNs) that consider different networking factors such as AP locations, and the density of UEs and APs. Another extension will consider pilot assignment jointly with pilot power control, which can further improve the channel estimation performance. The scalability of different pilot assignment strategies is another factor that should be considered in future research.

7 Conclusion

Next-generation wireless communication systems will create a digitally connected society of automated and intelligent systems. These systems will reshape various parts of our daily lives like healthcare, entertainment, homes, vehicles, industries, and cities. The 5G wireless networks have already been deployed worldwide, providing a multi-fold QoS improvement, compared to 4G, by adopting new techniques, such as mmWave frequency bands, advanced spectrum management techniques, and the integration of licensed and unlicensed bands. B5G communication systems still need to offer new technologies and more efficient solutions to handle the rapid traffic growth demands. In this thesis, we studied the paradigm of future-generation wireless systems and discussed their requirements, specifications, applications, and enabling technologies. High-datarate ubiquitous transmission is considered as one of the main requirements of the NextG systems, aiming to provide high-speed and reliable connectivity to anyone, anytime, anywhere.

The abundant bandwidth available in mmWave frequency bands is significantly higher than that of the legacy sub-6 GHz counterpart. Hence, mmWave communications have already been considered, standardized, and implemented in current wireless systems, both indoor and outdoor, to deliver multi-gigabit connections. In this thesis, we studied the current operational mmWave networks for indoor and outdoor environments. We investigated the IEEE 802.11ad / ay standards that operate over 60 GHz to provide high-speed connectivity in the scale of Gbps for indoor users. User and traffic scheduling is a challenging task in these systems, highly affecting the system's performance. Hence, we discussed the challenges related to the scheduling in realistic scenarios of IEEE 802.11ad / ay devices, studied some pre-existing works, and proposed some research directions.

This thesis also reported the result of a measurement campaign conducted to analyze the performance of an early deployed mmWave cell. Various environmental impacts on mmWave links are studied, from the body and foliage blockage to rain and over-water transmission. The impact of these phenomena over mmWaves propagations is different but generally degrades the

received signal power and service quality. Comparing the measured RSRP with the simulated omnidirectional and strongest RSRP (optimal antenna configuration) shows a considerable gap between the real-world measurements and the theoretical performance. Our study showed that network planners deploying 5G mmWave solutions for applications need carefully design their systems, as ignoring some environmental factors, like rain or wind, can significantly affect the system performance. Current 5G mmWave is not suitable for NLoS and dynamic environments (where the LoS link is constantly blocked), at least with current TCP protocols and for the applications that require reliable transmissions. In these cases, combining mmWave with multi-path TCP or TCP proxy architecture can provide better service levels, which should be considered in future wireless communication systems. The applications of current outdoor mmWave systems are mainly limited to the scenarios in which transmitter and receiver are stationary and have a perfect LoS, e.g., FWA that provides high-speed internet for houses. For more complex use cases such as large industrial environments (where LoS links get blocked by hefty mobile machinery) and cell phones (where the antennas can easily be covered and blocked by the user's hands, head, and body), the usage of mmWaves is challenging and still limited. More efficient beamforming, beam-tracking / beam-switching techniques, blockage prediction, link prediction [241], proactive rate adjustment methods, smart handover techniques, and advanced scheduling, vision aided network management systems [242], [243] are still required to be deployed before making mmWave communications a standard and everyday technology for end-users.

6G will be add new new technologies and innovations such as RIS, UAVs, and CF mMIMO, on top of the existing 5G systems, e.g. mmWave communication. These technologies will significantly enhance performance and bring multi-fold improvement in QoS comparing the previous technologies. Most of these technologies are still under research and should be significantly improved in terms of various performance metrics, including data rate, network coverage, and energy consumption, before becoming standard and functional. Network optimization techniques are suitable tools to ensure that these technologies efficiently utilize the available resources. Hence, in this thesis, we designed and developed network-wide optimization schemes that can be applied to different networking scenarios. For example, we designed an optimization scenario to RIS-aided UAV communications to reduce network overall energy consumption while guaranteeing certain QoS. UAV based transmissions can provide high-speed communication in dense urban areas over mmWaves. The high energy consumption of drones makes UAV communications challenging and energy-critical. The primary source of this power consumption comes from the UAV's movement. RIS can be jointly used with UAV to increase its coverage and provide an energy-efficient and sustainable transmission by reducing UAV's need to move. The problem is defined as a joint UAV trajectory and RIS phase optimization problem problems and the successive convex approximation employed to solve it. The convex approximation techniques could provide a feasible solution but are very sensitive to different network configurations. Adding more parameters to the problem, such as beamforming uncertainty and mobile users, and considering the swarm of UAVs makes the optimization problem mathematically intractable and very hard to solve. In such scenarios, learning-based approaches such as reinforcement learning seem very attractive and can replace the traditional convex optimization schemes.

As another example of network optimization, we considered the pilot assignment problem in CF mMIMO systems. We formulated the pilot assignment in CF mMIMO as a diverse clustering problem and proposed clustering-based solutions that maximize the overall rate of the network. The proposed solutions employ iterative local search to find the best local solutions and replace the incumbent solution in case of improvement. These schemes perform almost as well as the optimal solutions but with far less complexity.

Given the increasing complexity of future wireless communication systems, the traditional optimization schemes will eventually fail to find optimal solutions for tasks like resource allocations and power control, at least in real time. Hence, recently Machine Learning (ML) and especially deep learning approach widely investigated to solve some significant problems in NextG systems. Thanks to recent advances in deep learning for natural language processing and computer vision, these ideas can partially be adopted for specific problems in wireless communications, i.e., channel estimation, resource, and power control. For example, the resource allocation problem in wireless communication can be considered a translation problem (similar to image-to-image and natural language translation), and a deep learning model, i.e., transformers, can be trained to make some predictions and assignments. This deep learning model can feed various data about wireless network topology data, such as the location of nodes, link quality, and power level, and the output will be a proper resource, e.g., orthogonal channel or pilot, for each node. Here the deep learning model considers the network as a whole and learns the relations among different network entities to reach cognition and understanding of the network and use this knowledge for various tasks, such as resource allocation and power control. The main challenge in employing deep learning for wireless communications is its need for labeled datasets, which could be very expensive for wireless communication tasks, if not impossible. Reinforcement Learning (RL), on the other hand, is an approach for sequential decision-making problems in which an agent learns from interaction with the environment in an action-reward loop and is widely being investigated in wireless communications.

List of publications

Journals

[244] S. Mohebi, A. Zanella, and M. Zorzi, “Pilot Reuse in Cell-Free Massive MIMO Systems: A Diverse Clustering Approach,” IEEE Transactions on Wireless Communications, [submitted].

[245] S. Mohebi, F. Michelinakis, A. Elmokashfi, O. Grøndalen, K. Mahmood, and A. Zanella, “Sectors, Beams and Environmental Impact on the Performance of Commercial 5G mmWave Cells: an Empirical Study,” IEEEAccess, pp. 1–15, 2022.

Conferences

[53] S. Mohebi, M. Lecci, A. Zanella, and M. Zorzi, “The challenges of Scheduling and Resource Allocation in IEEE 802.11 ad / ay,” in Mediterranean Communication and Computer Networking Conference (MedComNet), IEEE, 2020, pp. 1–4.

[226] S. Mohebi, A. Zanella, and M. Zorzi, “Repulsive Clustering Based Pilot Assignment for Cell-Free Massive MIMO Systems,” in 30th European Signal Processing Conference (EUSIPCO), IEEE, 2022, pp. 717–721.

[246] A. A. Deshpande, C. J. Vaca-Rubio, S. Mohebi, D. Salami, E. De Carvalho, P. Popovski, S. Sigg, M. Zorzi, and A. Zanella, “Energy-Efficient Design for RIS-assisted UAV communications in beyond-5G Networks,” in 20th Mediterranean Communication and Computer Networking Conference (MedComNet), IEEE, 2022, pp. 158–165.

[247] S. Mohebi, F. Perez-Cruz, A. Zanella, and M. Zorzi, “Towards Congnition-based Networking,” [in preparation].

WindMill Deliverables

[248] S. Mohebi and et al., “Scheduling in IEEE 802.11ad,” chapter in “Initial report on ML for radio resource management and initial datasets”. WindMill Deliverables, 2020.

[249] ——, “Wireless Network Optimization Techniques using Anticipatory and Context Aware Techniques,” chapter in “State of the art on context acquisition & anticipatory optimisation techniques for network optimisation”. WindMill Deliverables, 2020.

[250] ——, “Hierarchical Reinforcement Learning: An Overview,” chapter in “Hierarchical and distributed learning architecture and multi-objective optimization strategies”. WindMill Deliverables, 2021.

[251] ——, “Power and Pilot Optimization in Cell-Free massive MIMO Systems,” chapter in “Final report on system wide cognitive optimisation schemes”. WindMill Deliverables, 2022.

Acknowledgments

Words cannot express my gratitude to my supervisors, Michele Zorzi and Andrea Zanella, for their invaluable patience and feedback. I believe this endeavor would not have been possible without ITN-WindMill, who funded my research. I am also grateful to my colleagues in the SIGNET lab, especially my office mates, for their help and moral support. Thanks should also go to the WindMill fellow ESRs and professors that impacted and inspired me. Additionally, I would like to express gratitude to Professor Fernando Perez-Cruz, for hosting me in the swiss data science center at ETH, Zurich, and to Dr. Kashif Mahmood for having me in Telenor Research, Oslo, and for all their help and support during my visits.

I would be remiss in not mentioning my family, especially my parents, siblings, and wife. Words can not describe how grateful I am to my mother and father (who I lost to COVID) for their lifelong love and support. Lastly, I could not have ended this journey without the support of my lovely wife, Sepideh, whose belief in me has kept my spirits and motivation high during this process.

References

[1] I. T. Union, Imt traffic estimates for the years 2020 to 2030, Jul. 2015. [Online]. Available: https://www.itu.int/dms_pub/itu-r/opb/rep/R-REP-M.2370-2015-TOC-HTM-E.htm.

[2] M. Z. Chowdhury, M. Shahjalal, S. Ahmed, and Y. M. Jang, "6g wireless communication systems: Applications, requirements, technologies, challenges, and research directions," IEEE Open Journal of the Communications Society, vol. 1, pp. 957–975, 2020.

[3] M. Giordani, M. Polese, M. Mezzavilla, S. Rangan, and M. Zorzi, "Toward 6g networks: Use cases and technologies," IEEE Communications Magazine, vol. 58, no. 3, pp. 55–61, 2020.

[4] S. J. Nawaz, S. K. Sharma, S. Wyne, M. N. Patwary, and M. Asaduzzaman, "Quantum machine learning for 6g communication networks: State-of-the-art and vision for the future," IEEE access, vol. 7, pp. 46 317–46 350, 2019.

[5] S. Mumtaz, J. M. Jornet, J. Aulin, W. H. Gerstacker, X. Dong, and B. Ai, "Terahertz communication for vehicular networks," IEEE Transactions on Vehicular Technology, vol. 66, no. 7, 2017.

[6] E. C. Strinati, S. Barbarossa, J. L. Gonzalez-Jimenez, D. Ktenas, N. Cassiau, L. Maret, and C. Dehos, "6g: The next frontier: From holographic messaging to artificial intelligence using subterahertz and visible light communication," IEEE Vehicular Technology Magazine, vol. 14, no. 3, pp. 42–50, 2019.

[7] W. Saad, M. Bennis, and M. Chen, "A vision of 6g wireless systems: Applications, trends, technologies, and open research problems," IEEE network, vol. 34, no. 3, pp. 134–142, 2019.

[8] K. David and H. Berndt, "6g vision and requirements: Is there any need for beyond 5g?" IEEE vehicular technology magazine, vol. 13, no. 3, pp. 72–80, 2018.

[9] F. Tariq, M. R. Khandaker, K.-K. Wong, M. A. Imran, M. Bennis, and M. Debbah, "A speculative study on 6g," IEEE Wireless Communications, vol. 27, no. 4, pp. 118–125, 2020.

[10] Ericsson, Autonomous Mobile Network Scanner User Manual, https://www.ericsson.com/en/reports-and-papers/mobility-report/mobility-visualizer, Accessed on: 2022-11-26, 2022.

[11] E. Björnson, J. Hoydis, L. Sanguinetti, et al., “Massive mimo networks: Spectral, energy, and hardware efficiency,” Foundations and Trends® in Signal Processing, vol. 11, no. 3-4, pp. 154–655, 2017.

[12] C. Liaskos, L. Mamatas, A. Pourdamghani, A. Tsioliaridou, S. Ioannidis, A. Pitsillides, S. Schmid, and I. F. Akyildiz, “Software-defined reconfigurable intelligent surfaces: From theory to end-to-end implementation,” Proceedings of the IEEE, 2022.

[13] Y. Liu, X. Liu, X. Mu, T. Hou, J. Xu, M. Di Renzo, and N. Al-Dhahir, “Reconfigurable intelligent surfaces: Principles and opportunities,” IEEE Communications Surveys & Tutorials, 2021.

[14] H. Q. Ngo, A. Ashikhmin, H. Yang, E. G. Larsson, and T. L. Marzetta, “Cell-free massive MIMO versus small cells,” IEEE Transactions on Wireless Communications, vol. 16, no. 3, pp. 1834–1850, Mar. 2017.

[15] H. He, X. Yu, J. Zhang, S. Song, and K. B. Letaief, “Cell-free massive mimo for 6g wireless communication networks,” Journal of Communications and Information Networks, vol. 6, no. 4, pp. 321–335, 2021.

[16] M. Latva-aho, K. Leppänen, F. Clazzer, and A. Munari, “Key drivers and research challenges for 6g ubiquitous wireless intelligence,” 2020.

[17] E. Markoval, D. Moltchanov, R. Pirmagomedov, D. Ivanova, Y. Koucheryavy, and K. Samouylov, “Priority-based coexistence of embb and urllc traffic in industrial 5g nr deployments,” in 2020 12th International Congress on Ultra Modern Telecommunications and Control Systems and Workshops (ICUMT), IEEE, 2020, pp. 1–6.

[18] Z. Na, Y. Liu, J. Shi, C. Liu, and Z. Gao, “Uav-supported clustered noma for 6g-enabled internet of things: Trajectory planning and resource allocation,” IEEE Internet of Things Journal, vol. 8, no. 20, pp. 15 041–15 048, 2020.

[19] C. De Alwis, A. Kalla, Q.-V. Pham, P. Kumar, K. Dev, W.-J. Hwang, and M. Liyanage, “Survey on 6g frontiers: Trends, applications, requirements, technologies and future research,” IEEE Open Journal of the Communications Society, vol. 2, pp. 836–886, 2021.

[20] I. F. Akyildiz, C. Han, and S. Nie, “Combating the distance problem in the millimeter wave and terahertz frequency bands,” IEEE Communications Magazine, vol. 56, no. 6, pp. 102–108, 2018.

[21] Y. Xing and T. S. Rappaport, “Propagation measurement system and approach at 140 ghz-moving to 6g and above 100 ghz,” in 2018 IEEE global communications Conference (GLOBECOM), IEEE, 2018, pp. 1–6.

[22] T. O'shea and J. Hoydis, "An introduction to deep learning for the physical layer," IEEE Transactions on Cognitive Communications and Networking, vol. 3, no. 4, pp. 563–575, 2017.

[23] G. Gür, "Expansive networks: Exploiting spectrum sharing for capacity boost and 6g vision," Journal of Communications and Networks, vol. 22, no. 6, pp. 444–454, 2020.

[24] J. Tanveer, A. Haider, R. Ali, and A. Kim, "Machine learning for physical layer in 5g and beyond wireless networks: A survey," Electronics, vol. 11, no. 1, p. 121, 2021.

[25] H. E. Melcherts, "The internet of everything and beyond: The interplay between things and humans," Human bond communication: the holy grail of holistic communication and immersive experience, pp. 173–185, 2017.

[26] N. Mahmood, A. Munari, F. Clazzer, and H. Bartz, "Critical and massive machine type communication towards 6g," 2020.

[27] M. Zawish, N. Ashraf, R. I. Ansari, S. Davy, H. K. Qureshi, N. Aslam, and S. A. Hassan, "Towards on-device ai and blockchain for 6g enabled agricultural supply-chain management," arXiv preprint arXiv:2203.06465, 2022.

[28] N. H. Mahmood, S. Böcker, A. Munari, F. Clazzer, I. Moerman, K. Mikhaylov, O. Lopez, O.-S. Park, E. Mercier, H. Bartz, et al., "White paper on critical and massive machine type communication towards 6g," arXiv preprint arXiv:2004.14146, 2020.

[29] K. Mikhaylov, V. Petrov, R. Gupta, M. A. Lema, O. Galinina, S. Andreev, Y. Koucheryavy, M. Valkama, A. Pouttu, and M. Dohler, "Energy efficiency of multi-radio massive machine-type communication (mr-mmtc): Applications, challenges, and solutions," IEEE Communications Magazine, vol. 57, no. 6, pp. 100–106, 2019.

[30] A. Lavric, A. I. Petrariu, and V. Popa, "Sigfox communication protocol: The new era of iot?" In 2019 international conference on sensing and instrumentation in IoT Era (ISSI), IEEE, 2019, pp. 1–4.

[31] Q. Zhou, K. Zheng, L. Hou, J. Xing, and R. Xu, "Design and implementation of open lora for iot," Ieee Access, vol. 7, pp. 100 649–100 657, 2019.

[32] F. A. De Figueiredo, F. A. Cardoso, I. Moerman, and G. Fraidenraich, "On the application of massive mimo systems to machine type communications," IEEE Access, vol. 7, pp. 2589–2611, 2018.

[33] A. Mishra, Y. Mao, L. Sanguinetti, and B. Clerckx, "Rate-splitting assisted massive machine-type communications in cell-free massive mimo," IEEE Communications Letters, 2022.

[34] M. A. Siddiqi, H. Yu, and J. Joung, “5g ultra-reliable low-latency communication implementation challenges and operational issues with iot devices,” Electronics, vol. 8, no. 9, p. 981, 2019.

[35] M. Alsenwi, N. H. Tran, M. Bennis, S. R. Pandey, A. K. Bairagi, and C. S. Hong, “Intelligent resource slicing for embb and urllc coexistence in 5g and beyond: A deep reinforcement learning based approach,” IEEE Transactions on Wireless Communications, vol. 20, no. 7, pp. 4585–4600, 2021.

[36] F. Fang, Y. Xu, Q.-V. Pham, and Z. Ding, “Energy-efficient design of irs-noma networks,” IEEE Transactions on Vehicular Technology, vol. 69, no. 11, pp. 14 088–14 092, 2020.

[37] C.-X. Wang, J. Huang, H. Wang, X. Gao, X. You, and Y. Hao, “6g wireless channel measurements and models: Trends and challenges,” IEEE Vehicular Technology Magazine, vol. 15, no. 4, pp. 22–32, 2020.

[38] J. Navarro-Ortiz, P. Romero-Diaz, S. Sendra, P. Ameigeiras, J. J. Ramos-Munoz, and J. M. Lopez-Soler, “A survey on 5g usage scenarios and traffic models,” IEEE Communications Surveys & Tutorials, vol. 22, no. 2, pp. 905–929, 2020.

[39] D. Vaya and T. Hadpawat, “Internet of everything (ioe): A new era of iot,” in ICCCE 2019, Springer, 2020, pp. 1–6.

[40] F. Hussain, “Internet of everything,” in Internet of things, Springer, 2017, pp. 1–11.

[41] S. A. Khowaja, P. Khuwaja, and K. Dev, “Internet of everything enabled solution for covid-19, its new variants and future pandemics: Framework, challenges, and research directions,” arXiv preprint arXiv:2101.02030, 2021.

[42] F. Yang, S. Wang, J. Li, Z. Liu, and Q. Sun, “An overview of internet of vehicles,” China communications, vol. 11, no. 10, pp. 1–15, 2014.

[43] M. M. Hamdi, L. Audah, S. A. Rashid, A. H. Mohammed, S. Alani, and A. S. Mustafa, “A review of applications, characteristics and challenges in vehicular ad hoc networks (vanets),” in 2020 International Congress on Human-Computer Interaction, Optimization and Robotic Applications (HORA), IEEE, 2020, pp. 1–7.

[44] J. Heo, B. Kang, J. M. Yang, J. Paek, and S. Bahk, “Performance-cost tradeoff of using mobile roadside units for v2x communication,” IEEE Transactions on Vehicular Technology, vol. 68, no. 9, pp. 9049–9059, 2019.

[45] J. He, K. Yang, and H.-H. Chen, “6g cellular networks and connected autonomous vehicles,” IEEE Network, vol. 35, no. 4, pp. 255–261, 2020.

[46] S. Huang, B. Wang, X. Li, P. Zheng, D. Mourtzis, and L. Wang, “Industry 5.0 and society 5.0—comparison, complementation and co-evolution,” Journal of Manufacturing Systems, vol. 64, pp. 424–428, 2022.

[47] A. P. Dani, I. Salehi, G. Rotithor, D. Trombetta, and H. Ravichandar, “Human-in-the-loop robot control for human-robot collaboration: Human intention estimation and safe trajectory tracking control for collaborative tasks,” IEEE Control Systems Magazine, vol. 40, no. 6, pp. 29–56, 2020.

[48] B. Li, Z. Fei, and Y. Zhang, “Uav communications for 5g and beyond: Recent advances and future trends,” IEEE Internet of Things Journal, vol. 6, no. 2, pp. 2241–2263, 2018.

[49] A. Hafeez, M. A. Husain, S. Singh, A. Chauhan, M. T. Khan, N. Kumar, A. Chauhan, and S. Soni, “Implementation of drone technology for farm monitoring & pesticide spraying: A review,” Information Processing in Agriculture, 2022.

[50] P. K. R. Maddikunta, S. Hakak, M. Alazab, S. Bhattacharya, T. R. Gadekallu, W. Z. Khan, and Q.-V. Pham, “Unmanned aerial vehicles in smart agriculture: Applications, requirements, and challenges,” IEEE Sensors Journal, vol. 21, no. 16, pp. 17 608–17 619, 2021.

[51] A. Çöltekin, I. Lochhead, M. Madden, S. Christophe, A. Devaux, C. Pettit, O. Lock, S. Shukla, L. Herman, Z. Stacho , et al., “Extended reality in spatial sciences: A review of research challenges and future directions,” ISPRS International Journal of Geo-Information, vol. 9, no. 7, p. 439, 2020.

[52] X. Xu, Y. Pan, P. P. M. Y. Lwin, and X. Liang, “3d holographic display and its data transmission requirement,” in 2011 international conference on information photonics and optical communications, IEEE, 2011, pp. 1–4.

[53] S. Mohebi, M. Lecci, A. Zanella, and M. Zorzi, “The challenges of Scheduling and Resource Allocation in IEEE 802.11 ad / ay,” in Mediterranean Communication and Computer Networking Conference (MedComNet), IEEE, 2020, pp. 1–4.

[54] Task Group ay, TGay usage model, doc.: 802.11-15 / 0625r7, Nov. 2017. [Online]. Available: https://mentor.ieee.org/802.11/dcn/15/11-15-0625-07-00ay-ieee-802-11-tgay-usage-scenarios.pptx.

[55] C. Wang, Y. Chen, Z. Lu, X. Wen, Z. Wang, and L. Wang, “FC-BET: A Fast Consecutive Beam Tracking Scheme for MmWave Vehicular Communications,” in 2021 IEEE Wireless Communications and Networking Conference (WCNC), IEEE, 2021, pp. 1–6.

[56] S. Huang, Y. Gao, W. Xu, Y. Gao, and Z. Feng, “Energy-angle domain initial access and beam tracking in millimeter wave v2x communications,” IEEE Access, vol. 7, pp. 9340–9350, 2019.

[57] C. Han, Y. Wu, Z. Chen, and X. Wang, “Terahertz communications (teracom): Challenges and impact on 6g wireless systems,” arXiv preprint arXiv:1912.06040, 2019.

[58] I. F. Akyildiz, J. M. Jornet, and C. Han, “Terahertz band: Next frontier for wireless communications,” Physical communication, vol. 12, pp. 16–32, 2014.

[59] K. Tekbıyık, A. R. Ekti, G. K. Kurt, and A. Görçin, “Terahertz band communication systems: Challenges, novelties and standardization efforts,” Physical Communication, vol. 35, p. 100 700, 2019.

[60] S. Ali, W. Saad, N. Rajatheva, K. Chang, D. Steinbach, B. Sliwa, C. Wietfeld, K. Mei, H. Shiri, H.-J. Zepernick, et al., “6g white paper on machine learning in wireless communication networks,” arXiv preprint arXiv:2004.13875, 2020.

[61] G. Zhu, D. Liu, Y. Du, C. You, J. Zhang, and K. Huang, “Toward an intelligent edge: Wireless communication meets machine learning,” IEEE communications magazine, vol. 58, no. 1, pp. 19–25, 2020.

[62] M. E. Morocho-Cayamcela, H. Lee, and W. Lim, “Machine learning for 5g/b5g mobile and wireless communications: Potential, limitations, and future directions,” IEEE access, vol. 7, pp. 137 184–137 206, 2019.

[63] Y. Sun, M. Peng, Y. Zhou, Y. Huang, and S. Mao, “Application of machine learning in wireless networks: Key techniques and open issues,” IEEE Communications Surveys & Tutorials, vol. 21, no. 4, pp. 3072–3108, 2019.

[64] R.-A. Stoica and G. T. F. de Abreu, “6g: The wireless communications network for collaborative and ai applications,” arXiv preprint arXiv:1904.03413, 2019.

[65] L. Lovén, T. Leppänen, E. Peltonen, J. Partala, E. Harjula, P. Porambage, M. Ylianttila, and J. Riekki, “Edgeai: A vision for distributed, edge-native artificial intelligence in future 6g networks,” The 1st 6G wireless summit, pp. 1–2, 2019.

[66] F. Clazzer, A. Munari, G. Liva, F. Lazaro, C. Stefanovic, and P. Popovski, “From 5g to 6g: Has the time for modern random access come?” arXiv preprint arXiv:1903.03063, 2019.

[67] Y. Liu, X. Yuan, Z. Xiong, J. Kang, X. Wang, and D. Niyato, “Federated learning for 6g communications: Challenges, methods, and future directions,” China Communications, vol. 17, no. 9, pp. 105–118, 2020.

[68] Z. Yang, M. Chen, K.-K. Wong, H. V. Poor, and S. Cui, "Federated learning for 6g: Applications, challenges, and opportunities," Engineering, 2021.

[69] T. Li, A. K. Sahu, A. Talwalkar, and V. Smith, "Federated learning: Challenges, methods, and future directions," IEEE Signal Processing Magazine, vol. 37, no. 3, pp. 50–60, 2020.

[70] S. Niknam, H. S. Dhillon, and J. H. Reed, "Federated learning for wireless communications: Motivation, opportunities, and challenges," IEEE Communications Magazine, vol. 58, no. 6, pp. 46–51, 2020.

[71] D. C. Nguyen, M. Ding, Q.-V. Pham, P. N. Pathirana, L. B. Le, A. Seneviratne, J. Li, D. Niyato, and H. V. Poor, "Federated learning meets blockchain in edge computing: Opportunities and challenges," IEEE Internet of Things Journal, vol. 8, no. 16, pp. 12 806–12 825, 2021.

[72] Q. Yang, Y. Liu, T. Chen, and Y. Tong, "Federated machine learning: Concept and applications," ACM Transactions on Intelligent Systems and Technology (TIST), vol. 10, no. 2, pp. 1–19, 2019.

[73] A. Bürkle, F. Segor, and M. Kollmann, "Towards autonomous micro uav swarms," Journal of intelligent & robotic systems, vol. 61, no. 1, pp. 339–353, 2011.

[74] M. Campion, P. Ranganathan, and S. Faruque, "A review and future directions of uav swarm communication architectures," in 2018 IEEE international conference on electro/information technology (EIT), IEEE, 2018, pp. 0903–0908.

[75] ——, "Uav swarm communication and control architectures: A review," Journal of Unmanned Vehicle Systems, vol. 7, no. 2, pp. 93–106, 2018.

[76] M. A. ElMossallamy, H. Zhang, L. Song, K. G. Seddik, Z. Han, and G. Y. Li, "Reconfigurable intelligent surfaces for wireless communications: Principles, challenges, and opportunities," IEEE Transactions on Cognitive Communications and Networking, vol. 6, no. 3, pp. 990–1002, 2020.

[77] E. Basar, M. Di Renzo, J. De Rosny, M. Debbah, M.-S. Alouini, and R. Zhang, "Wireless communications through reconfigurable intelligent surfaces," IEEE access, vol. 7, pp. 116 753–116 773, 2019.

[78] E. Björnson, Ö. Özdogan, and E. G. Larsson, "Reconfigurable intelligent surfaces: Three myths and two critical questions," IEEE Communications Magazine, vol. 58, no. 12, pp. 90–96, 2020.

[79] C. Huang, A. Zappone, G. C. Alexandropoulos, M. Debbah, and C. Yuen, "Reconfigurable intelligent surfaces for energy efficiency in wireless communication," IEEE Transactions on Wireless Communications, vol. 18, no. 8, pp. 4157–4170, 2019.

[80] C. Pan, H. Ren, K. Wang, J. F. Kolb, M. Elkashlan, M. Chen, M. Di Renzo, Y. Hao, J. Wang, A. L. Swindlehurst, et al., "Reconfigurable intelligent surfaces for 6g systems: Principles, applications, and research directions," IEEE Communications Magazine, vol. 59, no. 6, pp. 14–20, 2021.

[81] M. Jung, W. Saad, and G. Kong, "Performance analysis of active large intelligent surfaces (liss): Uplink spectral efficiency and pilot training," IEEE Transactions on Communications, vol. 69, no. 5, pp. 3379–3394, 2021.

[82] M. Di Renzo, K. Ntontin, J. Song, F. H. Danufane, X. Qian, F. Lazarakis, J. De Rosny, D.-T. Phan-Huy, O. Simeone, R. Zhang, et al., "Reconfigurable intelligent surfaces vs. relaying: Differences, similarities, and performance comparison," IEEE Open Journal of the Communications Society, vol. 1, pp. 798–807, 2020.

[83] H. Q. Ngo, E. G. Larsson, and T. L. Marzetta, "Energy and spectral efficiency of very large multiuser mimo systems," IEEE Transactions on Communications, vol. 61, no. 4, pp. 1436–1449, 2013.

[84] G. Interdonato, E. Björnson, H. Quoc Ngo, P. Frenger, and E. G. Larsson, "Ubiquitous cell-free massive MIMO communications," EURASIP Journal on Wireless Communications and Networking, vol. 2019, no. 1, pp. 1–13, 2019.

[85] S. Chen, J. Zhang, Y. Jin, and B. Ai, "Wireless powered ioe for 6g: Massive access meets scalable cell-free massive mimo," China Communications, vol. 17, no. 12, pp. 92–109, 2020.

[86] A. L. Imoize, H. I. Obakhena, F. I. Anyasi, and S. N. Sur, "A review of energy efficiency and power control schemes in ultra-dense cell-free massive mimo systems for sustainable 6g wireless communication," Sustainability, vol. 14, no. 17, p. 11 100, 2022.

[87] C. Pan, J. Yi, C. Yin, J. Yu, and X. Li, "Joint 3d uav placement and resource allocation in software-defined cellular networks with wireless backhaul," IEEE Access, vol. 7, pp. 104 279–104 293, 2019.

[88] M. Mozaffari, A. T. Z. Kasgari, W. Saad, M. Bennis, and M. Debbah, "Beyond 5g with uavs: Foundations of a 3d wireless cellular network," IEEE Transactions on Wireless Communications, vol. 18, no. 1, pp. 357–372, 2018.

[89] M. Giordani and M. Zorzi, "Non-terrestrial networks in the 6g era: Challenges and opportunities," IEEE Network, vol. 35, no. 2, pp. 244–251, 2020.

[90] N. Gisin and R. Thew, "Quantum communication," Nature photonics, vol. 1, no. 3, pp. 165–171, 2007.

[91] X. Su, M. Wang, Z. Yan, X. Jia, C. Xie, and K. Peng, "Quantum network based on non-classical light," Science China Information Sciences, vol. 63, no. 8, pp. 1–12, 2020.

[92] T. Huang, W. Yang, J. Wu, J. Ma, X. Zhang, and D. Zhang, "A survey on green 6g network: Architecture and technologies," IEEE access, vol. 7, pp. 175 758–175 768, 2019.

[93] N. Chi, Y. Zhou, Y. Wei, and F. Hu, "Visible light communication in 6g: Advances, challenges, and prospects," IEEE Vehicular Technology Magazine, vol. 15, no. 4, pp. 93–102, 2020.

[94] M. Katz and I. Ahmed, "Opportunities and challenges for visible light communications in 6g," 2020 2nd 6G wireless summit (6G SUMMIT), pp. 1–5, 2020.

[95] S. Ariyanti and M. Suryanegara, "Visible light communication (vlc) for 6g technology: The potency and research challenges," in 2020 Fourth World Conference on Smart Trends in Systems, Security and Sustainability (WorldS4), IEEE, 2020, pp. 490–493.

[96] T. Hewa, G. Gür, A. Kalla, M. Ylianttila, A. Bracken, and M. Liyanage, "The role of blockchain in 6g: Challenges, opportunities and research directions," 2020 2nd 6G Wireless Summit (6G SUMMIT), pp. 1–5, 2020.

[97] T. Nguyen, N. Tran, L. Loven, J. Partala, M.-T. Kechadi, and S. Pirttikangas, "Privacy-aware blockchain innovation for 6g: Challenges and opportunities," 2020 2nd 6G Wireless Summit (6G SUMMIT), pp. 1–5, 2020.

[98] W. Li, Z. Su, R. Li, K. Zhang, and Y. Wang, "Blockchain-based data security for artificial intelligence applications in 6g networks," IEEE Network, vol. 34, no. 6, pp. 31–37, 2020.

[99] T. Maksymyuk, J. Gazda, M. Volosin, G. Bugar, D. Horvath, M. Klymash, and M. Dohler, "Blockchain-empowered framework for decentralized network management in 6g," IEEE Communications Magazine, vol. 58, no. 9, pp. 86–92, 2020.

[100] A. Liu, Z. Huang, M. Li, Y. Wan, W. Li, T. X. Han, C. Liu, R. Du, D. K. P. Tan, J. Lu, et al., "A survey on fundamental limits of integrated sensing and communication," IEEE Communications Surveys & Tutorials, vol. 24, no. 2, pp. 994–1034, 2022.

[101] F. Liu, Y. Cui, C. Masouros, J. Xu, T. X. Han, Y. C. Eldar, and S. Buzzi, "Integrated sensing and communications: Towards dual-functional wireless networks for 6g and beyond," IEEE journal on selected areas in communications, 2022.

[102] Y. Cui, F. Liu, X. Jing, and J. Mu, "Integrating sensing and communications for ubiquitous iot: Applications, trends, and challenges," IEEE Network, vol. 35, no. 5, pp. 158–167, 2021.

[103] D. K. P. Tan, J. He, Y. Li, A. Bayesteh, Y. Chen, P. Zhu, and W. Tong, "Integrated sensing and communication in 6g: Motivations, use cases, requirements, challenges and future directions," in 2021 1st IEEE International Online Symposium on Joint Communications & Sensing (JC&S), IEEE, 2021, pp. 1–6.

[104] H. Hua, J. Xu, and T. X. Han, "Optimal transmit beamforming for integrated sensing and communication," arXiv preprint arXiv:2104.11871, 2021.

[105] Q. Zhang, H. Sun, Z. Wei, and Z. Feng, "Sensing and communication integrated system for autonomous driving vehicles," in IEEE INFOCOM 2020-IEEE Conference on Computer Communications Workshops (INFOCOM WKSHPS), IEEE, 2020, pp. 1278–1279.

[106] W. Yuan, Z. Wei, S. Li, J. Yuan, and D. W. K. Ng, "Integrated sensing and communication-assisted orthogonal time frequency space transmission for vehicular networks," IEEE Journal of Selected Topics in Signal Processing, vol. 15, no. 6, pp. 1515–1528, 2021.

[107] S. J. Nawaz, S. K. Sharma, B. Mansoor, M. N. Patwary, and N. M. Khan, "Non-coherent and backscatter communications: Enabling ultra-massive connectivity in 6g wireless networks," IEEE Access, vol. 9, pp. 38 144–38 186, 2021.

[108] C. Liaskos, A. Tsioliaridou, S. Ioannidis, A. Pitsillides, and I. F. Akyildiz, "Realizing ambient backscatter communications with intelligent surfaces in 6g wireless systems," IEEE Wireless Communications, vol. 29, no. 1, pp. 178–185, 2021.

[109] S. Basharat, S. A. Hassan, A. Mahmood, Z. Ding, and M. Gidlund, "Reconfigurable intelligent surface-assisted backscatter communication: A new frontier for enabling 6g iot networks," IEEE Wireless Communications, 2022.

[110] IEEE P802.11, IEEE standard for information technology – telecommunications and information exchange between systems local and metropolitan area networks – specific requirements - Part 11: Wireless LAN Medium Access Control (MAC) and Physical Layer (PHY) specifications, Dec. 2016.

[111] Task Group ay, Status of project IEEE 802.11ay, 2015. [Online]. Available: http://www.ieee802.org/11/Reports/tgay_update.htm.

[112] T. Nitsche, C. Cordeiro, A. B. Flores, E. W. Knightly, E. Perahia, and J. C. Widmer, "IEEE 802.11ad: Directional 60 GHz communication for multi-gigabit-per-second Wi-Fi," IEEE Communications Magazine, vol. 52, no. 12, pp. 132–141, Dec. 2014, ISSN: 1558-1896. DOI: 10.1109/MCOM.2014.6979964.

[113] E. Khorov, A. Ivanov, A. Lyakhov, and V. Zankin, “Mathematical Model for Scheduling in IEEE 802.11ad Networks,” in IFIP Wireless and Mobile Networking Conference (WMNC), Colmar, France, Jul. 2016. DOI: 10.1109/WMNC.2016.7543983.

[114] M. U. Rajan and A. Babu, “Theoretical maximum throughput of IEEE 802.11 ad millimeter wave wireless LAN in the contention based access period: With two level aggregation,” in International Conference on Wireless Communications, Signal Processing and Networking (WiSPNET), IEEE, Mar. 2017, pp. 2531–2536.

[115] H. Shokri-Ghadikolaei, L. Gkatzikis, and C. Fischione, “Beam-searching and transmission scheduling in millimeter wave communications,” in IEEE International Conference on Communications (ICC), IEEE, Jun. 2015, pp. 1292–1297.

[116] W. Feng, Y. Wang, D. Lin, N. Ge, J. Lu, and S. Li, “When mmWave communications meet network densification: A scalable interference coordination perspective,” IEEE Journal on Selected Areas in Communications, vol. 35, no. 7, pp. 1459–1471, Jul. 2017.

[117] H. Assasa, J. Widmer, T. Ropitault, and N. Golmie, “Enhancing the ns-3 IEEE 802.11ad model fidelity: Beam codebooks, multi-antenna beamforming training, and quasi-deterministic mmwave channel,” in ACM Workshop on ns-3 (WNS3), Florence, Italy, Jun. 2019, pp. 33–40, ISBN: 9781450371407. DOI: 10.1145/3321349.3321354.

[118] M. Lecci, P. Testolina, M. Giordani, M. Polese, T. Ropitault, C. Gentile, N. Varshney, A. Bodi, and M. Zorzi, “Simplified ray tracing for the millimeter wave channel: A performance evaluation,” in Information Theory and Applications Workshop (ITA), San Diego, CA, USA, Feb. 2020.

[119] H. Assasa, J. Widmer, J. Wang, T. Ropitault, and N. Golmie, “An implementation proposal for IEEE 802.11ay SU/MU-MIMO communication in ns-3,” in Workshop on Next-Generation Wireless with ns-3 (WNGW), Florence, Italy, Jun. 2019, pp. 26–29, ISBN: 9781450372787. DOI: 10.1145/3337941.3337947.

[120] T. Azzino, T. Ropitault, and M. Zorzi, “Scheduling the Data Transmission Interval in IEEE 802.11ad: A Reinforcement Learning Approach,” in International Conference on Computing, Networking and Communications (ICNC), Big Island, HI, US, Feb. 2020.

[121] N. Feamster and J. Rexford, “Why (and how) networks should run themselves,” in Applied Networking Research Workshop (ANRW), ACM, Jul. 2018, pp. 20–20.

[122] P. Gaw owicz and A. Zubow, “Ns-3 meets OpenAI gym: The playground for machine learning in networking research,” in ACM International Conference on Modeling, Analysis and Simulation of Wireless and Mobile Systems (MSWiM), Miami Beach, USA, Nov. 2019, pp. 113–120.

[123] R. Munos, T. Stepleton, A. Harutyunyan, and M. G. Bellemare, “Safe and efficient off-policy reinforcement learning,” in International Conference on Neural Information Processing Systems (NIPS), Barcelona, Spain, Dec. 2016, pp. 1054–1062, ISBN: 9781510838819.

[124] Task Group ad, TGad evaluation methodology, doc.: IEEE 802.11-09/0296r16, Jan. 2010. [Online]. Available: https://mentor.ieee.org/802.11/dcn/09/11-09-0296-16-00ad-evaluation-methodology.doc.

[125] Task Group ay, TGay evaluation methodology, doc.: 802.11-15/0866r2, Jan. 2016. [Online]. Available: https://mentor.ieee.org/802.11/dcn/15/11-15-0866-04-00ay-11ay-evaluation-methodology.doc.

[126] A. Narayanan, E. Ramadan, J. Carpenter, Q. Liu, Y. Liu, F. Qian, and Z.-L. Zhang, “A first look at commercial 5G performance on smartphones,” in Proceedings of The Web Conference 2020, 2020, pp. 894–905.

[127] A. Narayanan, X. Zhang, R. Zhu, A. Hassan, S. Jin, X. Zhu, X. Zhang, D. Rybkin, Z. Yang, Z. M. Mao, et al., “A variegated look at 5G in the wild: performance, power, and QoE implications,” in Proceedings of the 2021 ACM SIGCOMM 2021 Conference, 2021, pp. 610–625.

[128] A. Narayanan, E. Ramadan, R. Mehta, X. Hu, Q. Liu, R. A. Fezeu, U. K. Dayalan, S. Verma, P. Ji, T. Li, et al., “Lumos5G: Mapping and Predicting Commercial mmWave 5G Throughput,” in Proceedings of the ACM Internet Measurement Conference, 2020, pp. 176–193.

[129] F. Michelinakis, A. S. Al-Selwi, M. Capuzzo, A. Zanella, K. Mahmood, and A. Elmokashfi, “Dissecting Energy Consumption of NB-IoT Devices Empirically,” IEEE Internet of Things Journal, vol. 8, no. 2, pp. 1224–1242, 2020.

[130] 5G-HEART consortium, “D5.2: Initial Solution and Verification of Aquaculture Use Case Trials,” Tech. Rep., 2020.

[131] “Vertical industry use cases and requirements in 5g-vinni,” [Online]. Available: http://www.6gsummit.com/wp-content/uploads/2019/04/Day2_Session9_Groensund_Telenor.pdf (visited on 02/08/2020).

[132] A. Kaloxylos, A. Gavras, and R. De Peppe, Empowering Vertical Industries through 5G Networks - Current Status and Future Trends, Aug. 2020. DOI: 10.5281/zenodo.3698113. [Online]. Available: https://doi.org/10.5281/zenodo.3698113.

[133] D. Pimienta-del-Valle, L. Mendo, J. M. Riera, and P. Garcia-del-Pino, “Indoor LOS Propagation Measurements and Modeling at 26, 32, and 39 GHz Millimeter-Wave Frequency Bands,” Electronics, vol. 9, no. 11, p. 1867, 2020.

[134] M. Khalily, S. Taheri, S. Payami, M. Ghoraishi, and R. Tafazolli, “Indoor wideband directional millimeter wave channel measurements and analysis at 26 GHz, 32 GHz, and 39 GHz,” Transactions on Emerging Telecommunications Technologies, vol. 29, no. 10, e3311, 2018.

[135] Z. Lin, X. Du, H.-H. Chen, B. Ai, Z. Chen, and D. Wu, “Millimeter-wave propagation modeling and measurements for 5G mobile networks,” IEEE Wireless Communications, vol. 26, no. 1, pp. 72–77, 2019.

[136] X. Zhao, S. Li, Q. Wang, M. Wang, S. Sun, and W. Hong, “Channel measurements, modeling, simulation and validation at 32 GHz in outdoor microcells for 5G radio systems,” IEEE access, vol. 5, pp. 1062–1072, 2017.

[137] J. Ko, Y.-J. Cho, S. Hur, T. Kim, J. Park, A. F. Molisch, K. Haneda, M. Peter, D.-J. Park, and D.-H. Cho, “Millimeter-wave channel measurements and analysis for statistical spatial channel model in in-building and urban environments at 28 GHz,” IEEE Transactions on Wireless Communications, vol. 16, no. 9, pp. 5853–5868, 2017.

[138] S. Hur, H. Yu, J. Park, W. Roh, C. U. Bas, R. Wang, and A. F. Molisch, “Feasibility of mobility for millimeter-wave systems based on channel measurements,” IEEE Communications Magazine, vol. 56, no. 7, pp. 56–63, 2018.

[139] P. Zhang, B. Yang, C. Yi, H. Wang, and X. You, “Measurement-Based 5G Millimeter-Wave Propagation Characterization in Vegetated Suburban Macrocell Environments,” IEEE Transactions on Antennas and Propagation, 2020.

[140] C. U. Bas, R. Wang, S. Sangodoyin, S. Hur, K. Whang, J. Park, J. Zhang, and A. F. Molisch, “28 GHz microcell measurement campaign for residential environment,” in GLOBECOM 2017-2017 IEEE Global Communications Conference, IEEE, 2017, pp. 1–6.

[141] J. Ko, Y.-S. Noh, Y.-C. Kim, S. Hur, S.-r. Yoon, D. Park, K. Whang, D.-J. Park, and D.-H. Cho, “28 GHz millimeter-wave measurements and models for signal attenuation in vegetated areas,” in 2017 11th European Conference on Antennas and Propagation (EUCAP), IEEE, 2017, pp. 1808–1812.

[142] U. T. Virk and K. Haneda, “Modeling Human Blockage at 5G Millimeter-Wave Frequencies,” IEEE Transactions on Antennas and Propagation, vol. 68, no. 3, pp. 2256–2266, 2019.

[143] A. Alammouri, J. Mo, B. L. Ng, J. C. Zhang, and J. G. Andrews, “Hand grip impact on 5G mmWave mobile devices,” IEEE Access, vol. 7, pp. 60 532–60 544, 2019.

[144] J. Huang, Y. Cao, X. Raimundo, A. Cheema, and S. Salous, “Rain statistics investigation and rain attenuation modeling for millimeter wave short-range fixed links,” IEEE Access, vol. 7, pp. 156 110–156 120, 2019.

[145] A. M. Al-Saman, M. Cheffena, M. Mohamed, M. H. Azmi, and Y. Ai, “Statistical Analysis of Rain at Millimeter Waves in Tropical Area,” IEEE Access, vol. 8, pp. 51 044–51 061, 2020.

[146] R. Poorzare and A. Calveras, “Open trends on TCP performance over urban 5G mmwave networks,” in Proceedings of the 17th ACM Symposium on Performance Evaluation of Wireless Ad Hoc, Sensor, & Ubiquitous Networks, 2020, pp. 85–92.

[147] R. Poorzare and A. C. Augé, “Challenges on the way of implementing TCP over 5G networks,” IEEE access, vol. 8, pp. 176 393–176 415, 2020.

[148] M. Polese, R. Jana, and M. Zorzi, “TCP and MP-TCP in 5G mmWave networks,” IEEE Internet Computing, vol. 21, no. 5, pp. 12–19, 2017.

[149] ——, “TCP in 5G mmWave networks: Link level retransmissions and MP-TCP,” in 2017 IEEE Conference on Computer Communications Workshops (INFOCOM WKSHPS), IEEE, 2017, pp. 343–348.

[150] M. Zhang, M. Polese, M. Mezzavilla, J. Zhu, S. Rangan, S. Panwar, and M. Zorzi, “Will TCP work in mmWave 5G cellular networks?” IEEE Communications Magazine, vol. 57, no. 1, pp. 65–71, 2019.

[151] Y. Ren, W. Yang, X. Zhou, H. Chen, and B. Liu, “A survey on TCP over mmWave,” Computer Communications, 2021.

[152] T. Choi, C. U. Bas, R. Wang, S. Hur, J. Park, J. Zhang, and A. F. Molisch, “Measurement based directional modeling of dynamic human body shadowing at 28 GHz,” in 2018 IEEE Global Communications Conference (GLOBECOM), IEEE, 2018, pp. 1–6.

[153] V. Kristem, C. U. Bas, R. Wang, and A. F. Molisch, “Outdoor wideband channel measurements and modeling in the 3–18 GHz band,” IEEE Transactions on Wireless Communications, vol. 17, no. 7, pp. 4620–4633, 2018.

[154] K. Zhang, R. Zhang, J. Wu, Y. Jiang, and X. Tang, “Measurement and Modeling of Path Loss and Channel Capacity Analysis for 5G UMa Scenario,” in 2019 11th International Conference on Wireless Communications and Signal Processing (WCSP), IEEE, 2019, pp. 1–5.

[155] O. Ozdemir, F. Erden, I. Guvenc, T. Yekan, and T. Zarian, “28 GHz mmWave Channel Measurements: A Comparison of Horn and Phased Array Antennas and Coverage Enhancement Using Passive and Active Repeaters,” arXiv preprint arXiv:2002.00121, 2020.

[156] D. Xu, A. Zhou, X. Zhang, G. Wang, X. Liu, C. An, Y. Shi, L. Liu, and H. Ma, "Understanding Operational 5G: A First Measurement Study on Its Coverage, Performance and Energy Consumption," in Proceedings of the Annual conference of the ACM Special Interest Group on Data Communication on the applications, technologies, architectures, and protocols for computer communication, 2020, pp. 479–494.

[157] P. J. Mateo, C. Fiandrino, and J. Widmer, "Analysis of TCP performance in 5G mm-wave mobile networks," in ICC 2019-2019 IEEE International Conference on Communications (ICC), IEEE, 2019, pp. 1–7.

[158] Rohde & Schwarz, Autonomous Mobile Network Scanner User Manual, https://www.rohde-schwarz.com/cz/manual/r-s-tsma6-autonomous-mobile-network-scanner-user-manual-manuals-gb1_78701-572421.html, Accessed on: 2021-09-17, 2020.

[159] Nr; physical layer measurements (release 16), TS 38.215 V16.1.0, 3GPP, Mar. 2020.

[160] 3GPP, "Technical Specification Group Radio Access Network; NR; User Equipment (UE) procedures in Idle mode and RRC Inactive state," 3rd Generation Partnership Project (3GPP), Technical Specification (TS) 38.304, Dec. 2020, Version 16.3.0. [Online]. Available: https://portal.3gpp.org/desktopmodules/Specifications/SpecificationDetails.aspx?specificationId=3192 (visited on 04/13/2021).

[161] A. Klautau, N. González-Prelcic, and R. W. Heath, "LIDAR data for deep learning-based mmWave beam-selection," IEEE Wireless Communications Letters, vol. 8, no. 3, pp. 909–912, 2019.

[162] J. Zhu, D. Li, H. Zhao, X. Wang, and R. Jiang, "Adaptive SVM-based Beam Allocation for MmWave Small Cell Networks," in 2020 International Conference on Wireless Communications and Signal Processing (WCSP), IEEE, 2020, pp. 558–562.

[163] 3GPP, "Study on channel model for frequencies from 0.5 to 100 GHz," 3rd Generation Partnership Project (3GPP), Technical report (TR) 38.901, Jan. 2020, Version 16.1.0. [Online]. Available: https://portal.3gpp.org/desktopmodules/Specifications/SpecificationDetails.aspx?specificationId=3173 (visited on 04/13/2021).

[164] H. M. Rahim, C. Y. Leow, T. Abd Rahman, A. Arsad, and M. A. Malek, "Foliage attenuation measurement at millimeter wave frequencies in tropical vegetation," in 2017 IEEE 13th Malaysia International Conference on Communications (MICC), IEEE, 2017, pp. 241–246.

[165] M. Lecci, M. Polese, C. Lai, J. Wang, C. Gentile, N. Golmie, and M. Zorzi, "Quasi-deterministic channel model for mmWaves: Mathematical formalization and validation," in GLOBECOM 2020-2020 IEEE Global Communications Conference, IEEE, 2020, pp. 1–6.

[166] N. Varshney, J. Wang, C. Lai, C. Gentile, R. Charbonnier, and Y. Corre, "Quasi-deterministic channel propagation model for an urban environment at 28 GHz," IEEE Antennas and Wireless Propagation Letters, vol. 20, no. 7, pp. 1145–1149, 2021.

[167] TSGR, "TR 138 900 - V14.2.0 - LTE; 5G; Study on channel model for frequency spectrum above 6 GHz (3GPP TR 38.900 version 14.2.0 Release 14)," 2017. [Online]. Available: https://portal.etsi.org/TB/ETSIDeliverableStatus.aspx.

[168] K. Haneda, J. Zhang, L. Tan, G. Liu, Y. Zheng, H. Asplund, J. Li, Y. Wang, D. Steer, C. Li, et al., "5G 3GPP-like channel models for outdoor urban microcellular and macrocellular environments," in 2016 IEEE 83rd vehicular technology conference (VTC spring), IEEE, 2016, pp. 1–7.

[169] G. R. MacCartney, M. K. Samimi, and T. S. Rappaport, "Omnidirectional path loss models in New York City at 28 GHz and 73 GHz," in 2014 IEEE 25th Annual International Symposium on Personal, Indoor, and Mobile Radio Communication (PIMRC), IEEE, 2014, pp. 227–231.

[170] G. R. MacCartney and T. S. Rappaport, "Rural macrocell path loss models for millimeter wave wireless communications," IEEE Journal on selected areas in communications, vol. 35, no. 7, pp. 1663–1677, 2017.

[171] S. Sun, G. R. MacCartney, and T. S. Rappaport, "A novel millimeter-wave channel simulator and applications for 5G wireless communications," in 2017 IEEE International Conference on Communications (ICC), IEEE, 2017, pp. 1–7.

[172] S. Ju, O. Kanhere, Y. Xing, and T. S. Rappaport, "A millimeter-wave channel simulator NYUSIM with spatial consistency and human blockage," in 2019 IEEE global communications conference (GLOBECOM), IEEE, 2019, pp. 1–6.

[173] M. Polese, M. Mezzavilla, M. Zhang, J. Zhu, S. Rangan, S. Panwar, and M. Zorzi, "milliProxy: A TCP proxy architecture for 5G mmWave cellular systems," in 2017 51st Asilomar Conference on Signals, Systems, and Computers, IEEE, 2017, pp. 951–957.

[174] D. Zordan, F. Campagnaro, and M. Zorzi, "On the feasibility of an anti-grounding service with autonomous surface vessels," in OCEANS 2019-Marseille, IEEE, 2019, pp. 1–8.

[175] Y. Y. Munaye, R.-T. Juang, H.-P. Lin, and G. B. Tarekegn, “Resource Allocation for Multi-UAV Assisted IoT Networks: A Deep Reinforcement Learning Approach,” in 2020 International Conference on Pervasive Artificial Intelligence (ICPAI), IEEE, 2020, pp. 15–22.

[176] P.-M. Olsson, J. Kvarnström, P. Doherty, O. Burdakov, and K. Holmberg, “Generating UAV communication networks for monitoring and surveillance,” in 2010 11th international conference on control automation robotics & vision, IEEE, 2010, pp. 1070–1077.

[177] C. Luo, W. Miao, H. Ullah, S. McClean, G. Parr, and G. Min, “Unmanned aerial vehicles for disaster management,” in Geological disaster monitoring based on sensor networks, Springer, 2019, pp. 83–107.

[178] Y. Cai, Z. Wei, S. Hu, D. W. K. Ng, and J. Yuan, “Resource allocation for power-efficient IRS-assisted UAV communications,” in 2020 IEEE International Conference on Communications Workshops (ICC Workshops), IEEE, 2020, pp. 1–7.

[179] S. Li, B. Duo, X. Yuan, Y.-C. Liang, and M. Di Renzo, “Reconfigurable intelligent surface assisted UAV communication: Joint trajectory design and passive beamforming,” IEEE Wireless Communications Letters, vol. 9, no. 5, pp. 716–720, 2020.

[180] A. Ranjha and G. Kaddoum, “URLLC facilitated by mobile UAV relay and RIS: A joint design of passive beamforming, blocklength, and UAV positioning,” IEEE Internet of Things Journal, vol. 8, no. 6, pp. 4618–4627, 2020.

[181] L. Yang, F. Meng, J. Zhang, M. O. Hasna, and M. Di Renzo, “On the performance of RIS-assisted dual-hop UAV communication systems,” IEEE Transactions on Vehicular Technology, vol. 69, no. 9, pp. 10 385–10 390, 2020.

[182] B. Sheen, J. Yang, X. Feng, and M. M. U. Chowdhury, “A Deep Learning Based Modeling of Reconfigurable Intelligent Surface Assisted Wireless Communications for Phase Shift Configuration,” IEEE Open Journal of the Communications Society, 2021.

[183] K. Li, W. Ni, E. Tovar, and A. Jamalipour, “On-board deep Q-network for UAV-assisted online power transfer and data collection,” IEEE Transactions on Vehicular Technology, vol. 68, no. 12, pp. 12 215–12 226, 2019.

[184] M. Yi, X. Wang, J. Liu, Y. Zhang, and B. Bai, “Deep reinforcement learning for fresh data collection in UAV-assisted IoT networks,” in IEEE INFOCOM 2020-IEEE Conference on Computer Communications Workshops (INFOCOM WKSHPS), IEEE, 2020, pp. 716–721.

[185] A. Colpaert, E. Vinogradov, and S. Pollin, "3D beamforming and handover analysis for UAV networks," in 2020 IEEE Globecom Workshops (GC Wkshps, IEEE, 2020, pp. 1–6.

[186] M. Nemati, J. Park, and J. Choi, "RIS-assisted coverage enhancement in millimeter-wave cellular networks," IEEE Access, vol. 8, pp. 188 171–188 185, 2020.

[187] A. Fotouhi, H. Qiang, M. Ding, M. Hassan, L. G. Giordano, A. Garcia-Rodriguez, and J. Yuan, "Survey on UAV cellular communications: Practical aspects, standardization advancements, regulation, and security challenges," IEEE Communications Surveys & Tutorials, vol. 21, no. 4, pp. 3417–3442, 2019.

[188] H. V. Abeywickrama, B. A. Jayawickrama, Y. He, and E. Dutkiewicz, "Empirical power consumption model for UAVs," in 2018 IEEE 88th Vehicular Technology Conference (VTC-Fall), IEEE, 2018, pp. 1–5.

[189] E. D. Carvalho, A. Ali, A. Amiri, M. Angjelichinoski, and R. W. Heath, "Non-Stationarities in Extra-Large-Scale Massive MIMO," IEEE Wireless Communications, vol. 27, no. 4, pp. 74–80, 2020. DOI: 10.1109/MWC.001.1900157.

[190] G. Fontanesi, A. Zhu, and H. Ahmadi, "Outage Analysis for Millimeter-Wave Fronthaul Link of UAV-Aided Wireless Networks," IEEE Access, vol. 8, pp. 111 693–111 706, 2020.

[191] S. Lin, B. Zheng, G. C. Alexandropoulos, M. Wen, M. Di Renzo, and F. Chen, "Reconfigurable intelligent surfaces with reflection pattern modulation: Beamforming design and performance analysis," IEEE Transactions on Wireless Communications, vol. 20, no. 2, pp. 741–754, 2020.

[192] Y. Zeng, J. Xu, and R. Zhang, "Energy minimization for wireless communication with rotary-wing UAV," IEEE Transactions on Wireless Communications, vol. 18, no. 4, pp. 2329–2345, 2019.

[193] F. Mason, F. Chiariotti, M. Capuzzo, D. Magrin, A. Zanella, and M. Zorzi, "Combining lorawan and a new 3d motion model for remote uav tracking," in IEEE INFOCOM 2020-IEEE Conference on Computer Communications Workshops (INFOCOM WKSHPS), IEEE, 2020, pp. 412–417.

[194] E. Basar and I. Yildirim, "SimRIS channel simulator for reconfigurable intelligent surface-empowered communication systems," in 2020 IEEE Latin-American Conference on Communications (LATINCOM), IEEE, 2020, pp. 1–6.

[195] Y. Zeng and R. Zhang, "Energy-efficient UAV communication with trajectory optimization," IEEE Transactions on Wireless Communications, vol. 16, no. 6, pp. 3747–3760, 2017.

[196] M. Grant, S. Boyd, and Y. Ye, CVX: Matlab software for disciplined convex programming, 2009.

[197] H. Q. Ngo, A. Ashikhmin, H. Yang, E. G. Larsson, and T. L. Marzetta, "Cell-free massive MIMO: Uniformly great service for everyone," in 2015 IEEE 16th international workshop on signal processing advances in wireless communications (SPAWC), IEEE, 2015, pp. 201–205.

[198] J. Zhang, S. Chen, Y. Lin, J. Zheng, B. Ai, and L. Hanzo, "Cell-free massive MIMO: A new next-generation paradigm," IEEE Access, vol. 7, pp. 99 878–99 888, 2019.

[199] Ö. T. Demir, E. Björnson, and L. Sanguinetti, "Foundations of user-centric cell-free massive mimo," arXiv preprint arXiv:2108.02541, 2021.

[200] S. Elhoushy, M. Ibrahim, and W. Hamouda, "Cell-free massive MIMO: A survey," IEEE Communications Surveys & Tutorials, vol. 24, no. 1, pp. 492–523, 2021.

[201] E. Björnson and L. Sanguinetti, "Scalable cell-free massive MIMO systems," IEEE Transactions on Communications, vol. 68, no. 7, pp. 4247–4261, 2020.

[202] L. Lu, G. Y. Li, A. L. Swindlehurst, A. Ashikhmin, and R. Zhang, "An overview of massive MIMO: Benefits and challenges," IEEE journal of selected topics in signal processing, vol. 8, no. 5, pp. 742–758, 2014.

[203] T. L. Marzetta, "Massive MIMO: an introduction," Bell Labs Technical Journal, vol. 20, pp. 11–22, 2015.

[204] T. L. Marzetta and H. Yang, Fundamentals of massive MIMO. Cambridge University Press, 2016.

[205] E. G. Larsson, O. Edfors, F. Tufvesson, and T. L. Marzetta, "Massive MIMO for next generation wireless systems," IEEE communications magazine, vol. 52, no. 2, pp. 186–195, 2014.

[206] M. Sawahashi, Y. Kishiyama, A. Morimoto, D. Nishikawa, and M. Tanno, "Coordinated multipoint transmission / reception techniques for LTE-advanced [Coordinated and Distributed MIMO]," IEEE Wireless Communications, vol. 17, no. 3, pp. 26–34, 2010.

[207] R. Irmer, H. Droste, P. Marsch, M. Grieger, G. Fettweis, S. Brueck, H.-P. Mayer, L. Thiele, and V. Jungnickel, "Coordinated multipoint: Concepts, performance, and field trial results," IEEE Communications Magazine, vol. 49, no. 2, pp. 102–111, 2011.

[208] M. Kamel, W. Hamouda, and A. Youssef, "Ultra-dense networks: A survey," IEEE Communications surveys & tutorials, vol. 18, no. 4, pp. 2522–2545, 2016.

[209] S. Chen, F. Qin, B. Hu, X. Li, and Z. Chen, “User-centric ultra-dense networks for 5g: Challenges, methodologies, and directions,” IEEE Wireless Communications, vol. 23, no. 2, pp. 78–85, 2016.

[210] J. Wu, Z. Zhang, Y. Hong, and Y. Wen, “Cloud radio access network (C-RAN): a primer,” IEEE network, vol. 29, no. 1, pp. 35–41, 2015.

[211] E. Björnson and L. Sanguinetti, “Making cell-free massive MIMO competitive with MMSE processing and centralized implementation,” IEEE Transactions on Wireless Communications, vol. 19, no. 1, pp. 77–90, 2019.

[212] S. Chen, J. Zhang, J. Zhang, E. Björnson, and B. Ai, “A survey on user-centric cell-free massive MIMO systems,” Digital Communications and Networks, Dec. 2021.

[213] M. Attarifar, A. Abbasfar, and A. Lozano, “Random vs structured pilot assignment in cell-free massive MIMO wireless networks,” in 2018 IEEE International Conference on Communications Workshops (ICC Workshops), IEEE, May 2018, pp. 1–6.

[214] Y. Zhang, H. Cao, P. Zhong, C. Qi, and L. Yang, “Location-based greedy pilot assignment for cell-free massive MIMO systems,” in 2018 IEEE 4th International Conference on Computer and Communications (ICCC), IEEE, Dec. 2018, pp. 392–396.

[215] H. Yu, X. Yi, and G. Caire, “Topological pilot assignment in large-scale distributed MIMO networks,” IEEE Transactions on Wireless Communications, Feb. 2022.

[216] H. Liu, J. Zhang, S. Jin, and B. Ai, “Graph coloring based pilot assignment for cell-free massive MIMO systems,” IEEE Transactions on Vehicular Technology, vol. 69, no. 8, pp. 9180–9184, Jun. 2020.

[217] W. Zeng, Y. He, B. Li, and S. Wang, “Pilot assignment for cell-free massive MIMO systems using a weighted graphic framework,” IEEE Transactions on Vehicular Technology, Jun. 2021.

[218] H. Liu, J. Zhang, X. Zhang, A. Kurniawan, T. Juhana, and B. Ai, “Tabu-search-based pilot assignment for cell-free massive MIMO systems,” IEEE Transactions on Vehicular Technology, vol. 69, no. 2, pp. 2286–2290, Feb. 2019.

[219] J. Ding, D. Kong, and D. Qu, “Improved Tabu-Search Preamble Assignment in Cell-Free Massive MIMO Systems,” in 2021 International Wireless Communications and Mobile Computing (IWCMC), IEEE, Jul. 2021, pp. 718–723.

[220] S. Buzzi, C. D’Andrea, M. Fresia, Y.-P. Zhang, and S. Feng, “Pilot assignment in cell-free massive MIMO based on the Hungarian algorithm,” IEEE Wireless Communications Letters, vol. 10, no. 1, pp. 34–37, Jan. 2020.

[221] W. Li, X. Sun, and D. Chen, “Pilot Assignment Based on Weighted-Count for Cell-Free Massive MIMO Systems,” in 2021 Asia-Pacific Conference on Communications Technology and Computer Science (ACCTCS), IEEE, Jan. 2021, pp. 258–261.

[222] M. Sarker and A. O. Fapojuwo, “Granting Massive Access by Adaptive Pilot Assignment Scheme for Scalable Cell-free Massive MIMO Systems,” in 2021 IEEE 93rd Vehicular Technology Conference (VTC2021-Spring), IEEE, Apr. 2021, pp. 1–5.

[223] J. Li, Z. Wu, P. Zhu, D. Wang, and X. You, “Scalable Pilot Assignment Scheme for Cell-Free Large-Scale Distributed MIMO With Massive Access,” IEEE Access, vol. 9, pp. 122 107–122 112, Sep. 2021.

[224] N. Raharya, W. Hardjawana, O. Al-Khatib, and B. Vucetic, “Pursuit learning-based joint pilot allocation and multi-base station association in a distributed massive MIMO network,” IEEE Access, vol. 8, pp. 58 898–58 911, Mar. 2020.

[225] C. Zhu, Y. Liang, T. Li, and F. Li, “Pilot Assignment in Cell-Free Massive MIMO based on Quantum Bacterial Foraging Optimization,” in 2021 13th International Conference on Wireless Communications and Signal Processing (WCSP), IEEE, 2021, pp. 1–5.

[226] S. Mohebi, A. Zanella, and M. Zorzi, “Repulsive Clustering Based Pilot Assignment for Cell-Free Massive MIMO Systems,” in 30th European Signal Processing Conference (EUSIPCO), IEEE, 2022, pp. 717–721.

[227] T. C. Mai, H. Q. Ngo, M. Egan, and T. Q. Duong, “Pilot power control for cell-free massive MIMO,” IEEE Transactions on Vehicular Technology, vol. 67, no. 11, pp. 11 264–11 268, 2018.

[228] Q. Zhou, U. Benlic, Q. Wu, and J.-K. Hao, “Heuristic search to the capacitated clustering problem,” European Journal of Operational Research, vol. 273, no. 2, pp. 464–487, 2019.

[229] J. Brimberg, N. Mladenović, R. Todosijević, and D. Uroševiĉ, “Solving the capacitated clustering problem with variable neighborhood search,” Annals of Operations Research, vol. 272, no. 1, pp. 289–321, 2019.

[230] A. Schulz, “The balanced maximally diverse grouping problem with block constraints,” European Journal of Operational Research, vol. 294, no. 1, pp. 42–53, Oct. 2021.

[231] J. Brimberg, N. Mladenović, and D. Uroševiĉ, “Solving the maximally diverse grouping problem by skewed general variable neighborhood search,” Information Sciences, vol. 295, pp. 650–675, 2015.

[232] T. A. Feo and M. Khellaf, “A class of bounded approximation algorithms for graph partitioning,” Networks, vol. 20, no. 2, pp. 181–195, 1990.

[233] M. Papenberg and G. W. Klau, “Using anticlustering to partition data sets into equivalent parts,” Psychological Methods, vol. 26, no. 2, p. 161, Apr. 2021.

[234] M. J. Brusco, J. D. Cradit, and D. Steinley, “Combining diversity and dispersion criteria for anticlustering: A bicriterion approach,” British Journal of Mathematical and Statistical Psychology, vol. 73, no. 3, pp. 375–396, Sep. 2020.

[235] M. Gallego, M. Laguna, R. Martî, and A. Duarte, “Tabu search with strategic oscillation for the maximally diverse grouping problem,” Journal of the Operational Research Society, vol. 64, no. 5, pp. 724–734, 2013.

[236] Z. Fan, Y. Chen, J. Ma, and S. Zeng, “Erratum: A hybrid genetic algorithmic approach to the maximally diverse grouping problem,” Journal of the Operational Research Society, vol. 62, no. 7, pp. 1423–1430, 2011.

[237] K. Singh and S. Sundar, “A new hybrid genetic algorithm for the maximally diverse grouping problem,” International Journal of Machine Learning and Cybernetics, vol. 10, no. 10, pp. 2921–2940, 2019.

[238] F. J. Rodriguez, M. Lozano, C. Garcîa-Martînez, and J. D. González-Barrera, “An artificial bee colony algorithm for the maximally diverse grouping problem,” Information Sciences, vol. 230, pp. 183–196, 2013.

[239] X. Lai and J.-K. Hao, “Iterated maxima search for the maximally diverse grouping problem,” European Journal of Operational Research, vol. 254, no. 3, pp. 780–800, 2016.

[240] Z. Chen and E. Björnson, “Channel hardening and favorable propagation in cell-free massive MIMO with stochastic geometry,” IEEE Transactions on Communications, vol. 66, no. 11, pp. 5205–5219, 2018.

[241] Y. Koda, J. Park, M. Bennis, K. Yamamoto, T. Nishio, M. Morikura, and K. Nakashima, “Communication-efficient multimodal split learning for mmwave received power prediction,” IEEE Communications Letters, vol. 24, no. 6, pp. 1284–1288, 2020.

[242] T. Nishio, Y. Koda, J. Park, M. Bennis, and K. Doppler, “When wireless communications meet computer vision in beyond 5g,” IEEE Communications Standards Magazine, vol. 5, no. 2, pp. 76–83, 2021.

[243] Y. Tian, G. Pan, and M.-S. Alouini, “Applying deep-learning-based computer vision to wireless communications: Methodologies, opportunities, and challenges,” IEEE Open Journal of the Communications Society, vol. 2, pp. 132–143, 2020.